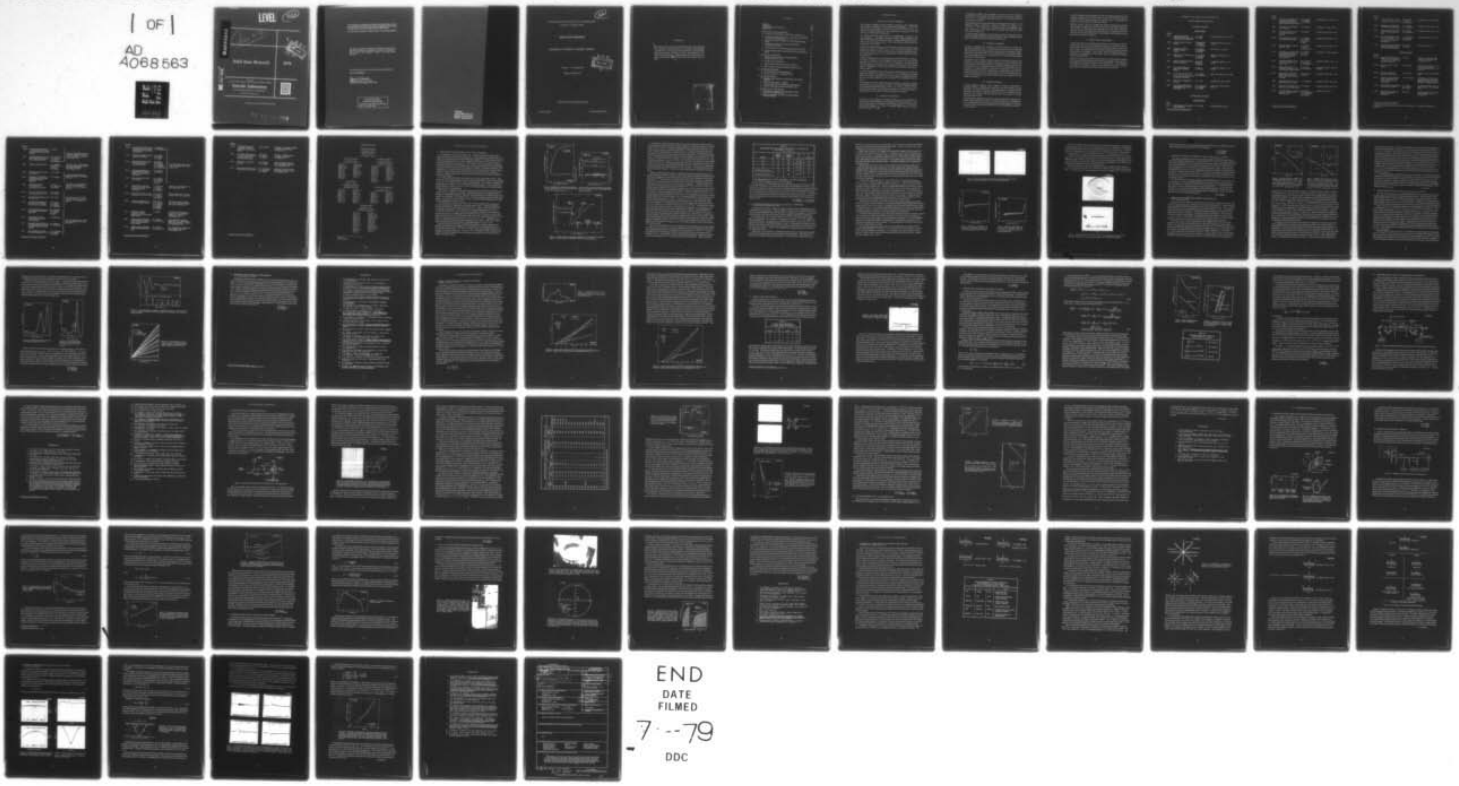
AD-A068 563 MASSACHUSETTS INST OF TECH LEXINGTON LINCOLN LAB F/G 9/3
SOLID STATE RESEARCH, 1978:4.(U)
NOV 78 A L MCWHORTER F19628-78-C-0002
UNCLASSIFIED ESD-TR-78-287 NL

1 OF 1
AD A068 563



END
DATE FILMED
7-79
DDC

ESD-TR-78-287

LEVEL II

4/12

AD A068563

See 1473

DDC
RECEIVED
MAY 15 1979
C

Solid State Research

1978

DDC FILE COPY

Prepared
under Electronic Systems Division Contract F19628-78-C-0002 by

Lincoln Laboratory
MASSACHUSETTS INSTITUTE OF TECHNOLOGY
LEXINGTON, MASSACHUSETTS



Approved for public release; distribution unlimited.

79 05 14 059

The work reported in this document was performed at Lincoln Laboratory, a center for research operated by Massachusetts Institute of Technology, with the support of the Department of the Air Force under Contract F19628-78-C-0002.

This report may be reproduced to satisfy needs of U.S. Government agencies.

The views and conclusions contained in this document are those of the contractor and should not be interpreted as necessarily representing the official policies, either expressed or implied, of the United States Government.

This technical report has been reviewed and is approved for publication.

FOR THE COMMANDER

Raymond L. Loiselle

Raymond L. Loiselle, Lt. Col., USAF
Chief, ESD Lincoln Laboratory Project Office

Non-Lincoln Recipients

PLEASE DO NOT RETURN

Permission is given to destroy this document when it is no longer needed.

Printed by
United States Air Force
Hanscom Air Force Base
Bedford, Massachusetts

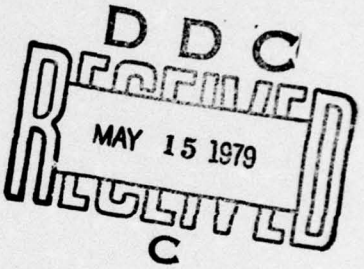
(12)

MASSACHUSETTS INSTITUTE OF TECHNOLOGY

LINCOLN LABORATORY

SOLID STATE RESEARCH

QUARTERLY TECHNICAL SUMMARY REPORT



1 AUGUST – 31 OCTOBER 1978

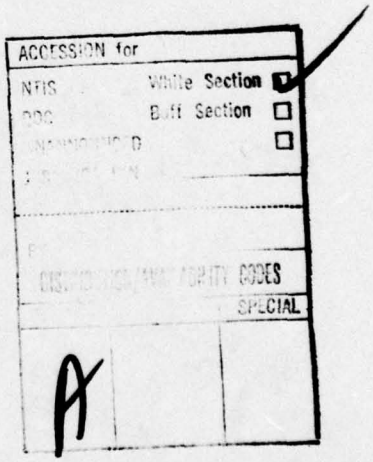
ISSUED 15 MARCH 1979

Approved for public release; distribution unlimited.

LEXINGTON MASSACHUSETTS

ABSTRACT

This report covers in detail the solid state research work of the Solid State Division at Lincoln Laboratory for the period 1 August through 31 October 1978. The topics covered are Solid State Device Research, Quantum Electronics, Materials Research, Microelectronics, and Surface-Wave Technology. Funding is primarily provided by the Air Force, with additional support provided by the Army, ARPA, NSF, and DOE.



CONTENTS

	Abstract	iii
	Introduction	vii
	Reports on Solid State Research	xi
	Organization	xvii
I.	SOLID STATE DEVICE RESEARCH	1
	A. Beryllium-Ion Implantation in InP and $In_{1-x}Ga_xAs_yP_{1-y}$	1
	B. P-N Junction Diodes in InP and $In_{1-x}Ga_xAs_yP_{1-y}$ Fabricated by Beryllium-Ion Implantation	4
	C. Growth of Nominally Undoped InP and $In_{0.8}Ga_{0.2}As_{0.5}P_{0.5}$ Alloys	8
	D. Transport Properties and Impurity Levels of InP and $In_{0.8}Ga_{0.2}As_{0.5}P_{0.5}$	8
	E. Photoluminescence of InP and $In_{0.8}Ga_{0.2}As_{0.5}P_{0.5}$ Alloys	10
	F. Interband Magnetooptical Measurements on $In_{1-x}Ga_xAs_yP_{1-y}$ Alloys	13
II.	QUANTUM ELECTRONICS	15
	A. Emission Cross Section and Flashlamp-Excited NdP_5O_{14} Laser at 1.32 μm	15
	B. Ni:MgF_2 Laser Development	18
	C. Higher-Order Nonlinear Processes in $CdGeAs_2$	20
	D. High-Resolution Tunable Submillimeter Spectroscopy	24
III.	MATERIALS RESEARCH	27
	A. Laser Annealing of Se-Implanted GaAs	27
	B. Activation Energy of Cr Acceptors in InP	33
IV.	MICROELECTRONICS	37
	A. Integrated Mixer Module for Submillimeter-Wavelength Operation	37
	B. Charge-Coupled Devices: Imagers	38
	C. Charge-Coupled Devices: SAW/CCD Buffer Memory	41
	D. Parallel-Plate Plasma Etching for Silicon CCDs	43
V.	SURFACE-WAVE TECHNOLOGY	47
	A. Parametric Interactions in Acoustoelectric Surface Acoustic Wave (SAW) Devices	47
	B. Resonant Interactions of Surface and Bulk Acoustic Waves in Gratings	53

INTRODUCTION

I. SOLID STATE DEVICE RESEARCH

Multi-energy Be implants in n-type InP and $In_{1-x}Ga_xAs_yP_{1-y}$ have yielded layers with uniform as-implanted Be concentrations of approximately 3×10^{18} cm^{-3}. Sheet carrier concentrations, which were in the $(1\text{-}2) \times 10^{14}$ cm^{-2} range, were obtained on samples implanted at room temperature and annealed at 750° and 700°C for InP and InGaAsP, respectively.

P-n junction diodes have been formed by Be-implantation in n-type InP and $In_{1-x}Ga_xAs_yP_{1-y}$. Low leakage currents and abrupt voltage breakdowns were observed for both mesa and planar InP diodes. Scanning photoresponse measurements of the $In_{1-x}Ga_xAs_yP_{1-y}$ ($E_g \approx 1.0$ eV) mesa diodes showed uniform avalanche gains of 2 to 3 times.

Liquid-phase epitaxy has been used to reproducibly grow InP and InGaAsP alloys with $N_D - N_A$ at the low 10^{15}-cm^{-3} level. The 77 K electron mobilities for the InP are in the 40,000- to 60,000-cm^2/V-sec range, with N_D/N_A between 2.5 and 6. For $In_{0.8}Ga_{0.2}As_{0.5}P_{0.5}$, the 77 K mobilities are 12,000 to 14,000 cm^2/V-sec with $N_D/N_A \leq 2$.

Analysis of measurements of the high-magnetic-field Hall coefficient vs temperature yields values for the concentrations of deep donors in InP and InGaAsP specimens of 5×10^{15} cm^{-3} and 3×10^{14} cm^{-3}, respectively. The transport data were fit using deep level donor activation energies of 0.29 and 0.12 eV for InP and InGaAsP, respectively. These energy values were inferred from the photoluminescence spectra.

In a study of photoluminescence of LPE-grown InP and InGaAsP, several spectral peaks were observed in a range 0.3 to 1.41 eV. An investigation is presently under way to test the hypothesis that one of the peaks in the photoluminescence spectra, with peak energies of 1.12 eV for InP and 0.9 eV for InGaAsP, is due to oxygen.

The oscillatory interband magneto-transmission has been measured on samples of LPE-grown $In_{0.77}Ga_{0.23}As_{0.52}P_{0.48}$ layers. The band parameters determined from the analysis of the data are $E_g = 1.07$ eV, $m_c^* = 0.061\ m_o$, and $E_p = 17.6$ eV, where these parameters are the direct energy gap at $T \approx 20$ K, the conduction-band effective mass, and the $\vec{k} \cdot \vec{p}$ interaction energy, respectively.

II. QUANTUM ELECTRONICS

The $^4F_{3/2} \rightarrow {}^4I_{13/2}$ emission cross section of NdP_5O_{14} at 1.32 μm has been determined from both spontaneous and stimulated emission measurements. The relative performance of a flashlamp-excited NdP_5O_{14} laser at 1.32 and 1.05 μm has also been evaluated. At 1.32 μm, a multimode output energy of 2.7 mJ has been achieved with 1.6 J input.

A CW-pumped Ni:MgF_2 laser operating at 1.62 μm has been repetitively Q-switched at 100 Hz, yielding a peak power output of 20 W with a power enhancement of $> 10^3$. A distributed loss coefficient $\leq 10^{-3}$ cm^{-1} has been measured in the Ni:MgF_2 laser crystal.

Phasematched fourth-harmonic generation in $CdGeAs_2$ has been carried out. The measured effective fourth-order nonlinear coefficient is $\chi^{(4)}_{I,eff}/\epsilon_o = 8 \times 10^{-27}$ m^3/V^3. The contribution of cascade processes, connected with lower-order nonlinearities, to the effective third- and fourth-order nonlinear coefficients has been considered.

A tunable sideband submillimeter spectrometer has been constructed as a first step in developing submillimeter frequency standards. Several rotational transitions in D_2O and CO have been measured to high accuracy.

III. MATERIALS RESEARCH

In order to investigate the usefulness of laser heating for removing ion-implantation damage in GaAs, a study has been made of the effects of annealing with a CW Nd:YAG laser on the electrical properties of Se-implanted samples. Good electrical activation of the Se donors has been achieved, but thermal stress due to laser heating can result in the formation of (111) slip planes that degrade the electrical characteristics.

To determine why Cr doping of InP has not yielded resistivities as high as those obtained for Fe-doped semi-insulating crystals used to provide substrates for epitaxial growth, the activation energy for thermally exciting electrons from the Cr acceptor level to the conduction band of InP has been determined from measurements of the Hall coefficient as a function of temperature. The activation energy was found to be 0.39 eV, indicating that Cr-doped samples have lower resistivities because the Cr level is considerably closer to the conduction band than is the Fe level (which has an activation energy of 0.65 eV), not because Cr is less soluble in InP than Fe.

IV. MICROELECTRONICS

A GaAs monolithic integrated circuit capable of receiving submillimeter-wavelength radiation coupled through a high-resistivity GaAs substrate has been fabricated. The circuit consists of a slot antenna coupled to a surface-oriented mixer diode by a section of coplanar transmission line and an integrated bypass capacitor. The conversion loss measured with this mixer module at 350 GHz was approximately 20 dB.

A system has been designed to make noise measurements related to charge transfer and charge detection on the 100- × 400-element imager for the GEODSS program. Using double-correlated sampling, noise-equivalent signals of 10 electrons at a 400-kHz data rate have been achieved from the floating diffusion output circuit of the imager.

A theoretical analysis has been made of the effect of sampling-finger width on the frequency response of the SAW/CCD buffer memory, and this analysis has been compared with the measured response of a prototype device. The measured response of the device falls off as predicted by theory.

Improved process control for parallel-plate plasma etching of low-pressure chemical vapor deposited films of silicon nitride and polycrystalline silicon has been achieved by constraining wafer temperatures to near room temperature. The lower etching rates obtained with this method are not significant when compared with the improved uniformity and reproducibility over methods that allow the wafer to be heated by the plasma.

V. SURFACE-WAVE TECHNOLOGY

A simplified model for the charge-storage process in acoustoelectric surface-acoustic-wave devices has been adopted; the many types of parametric interactions which occur in these devices can then be summarized within a unifying concept. Further, this conceptual view also identifies the kinds of signal-processing functions which are attainable. Devices which employ two-signal parametric interactions are straightforwardly interrelated, and the concept also extends to higher-order interactions.

A series of very sharp stop bands has been observed in the transmission response of a 200-groove normal-incidence grating when the wavelength of an incident surface acoustic wave is within ±20 percent of the grating period. These stop bands are produced by resonant conversion in the grating of surface waves into bulk waves which reflect back and forth from bottom to top of the crystal.

REPORTS ON SOLID STATE RESEARCH

15 August through 15 November 1978

PUBLISHED REPORTS

Journal Articles

JA No.			
4772	GaInAsP/InP Double-Heterostructure Lasers for Fiber Optic Communications	J.J. Hsieh C.C. Shen	Fiber Integ. Opt. 1, 357 (1978)
4791A	Surface States on n-Type $SrTiO_3$	S. Ellialtioğlu* T. Wolfram* V.E. Henrich	Solid State Commun. 27, 321 (1978)
4804	Efficient cw Optically Pumped Ni:MgF_2 Laser	P.F. Moulton A. Mooradian T.B. Reed	Opt. Lett. 3, 164 (1978)
4809	High Na^+-Ion Conductivity in $Na_5YSi_4O_{12}$	H.Y-P. Hong J.A. Kafalas M. Bayard	Mater. Res. Bull. 13, 757 (1978)
4814	Optical and Electrical Properties of $CdGeAs_2$	G.W. Iseler H. Kildal N. Menyuk	J. Electron. Mater. 7, 737 (1978)
4823	Vapor Phase Growth of $Hg_{1-x}Cd_xTe$ Epitaxial Layers	P. Vohl C.M. Wolfe	J. Electron. Mater. 7, 659 (1978)
4835	Condon Internal Diffraction in the $O_u^+ \rightarrow O_g^+$ Fluorescence of Photoassociated Hg_2	D.J. Ehrlich R.M. Osgood, Jr.	Phys. Rev. Lett. 41, 547 (1978)
4854	Solar Cells: Plugging into the Sun	J.C.C. Fan	Technol. Rev. 80, 14 (1978)
4856	Gap-Coupled InSb/$LiNbO_3$ Acoustoelectric Convolver Operating at 77 K	F.J. Leonberger R.W. Ralston S.A. Reible	Appl. Phys. Lett. 33, 484 (1978)

* * * * *

UNPUBLISHED REPORTS

Journal Articles

JA No.			
4806	Rate Equations in Stimulated Light Scattering	P.L. Kelley	Accepted by Phys. Rev. A

* Author not at Lincoln Laboratory.

JA No.			
4816	Pressure and Intensity Dependence of Multiphoton Energy Deposition and Reaction Yield in Vinyl Chloride	F.M. Lussier* J.I. Steinfeld* T.F. Deutsch	Accepted by Chem. Phys. Lett.
4843	Infrared Laser Photochemistry of Silane	T.F. Deutsch	Accepted by J. Chem. Phys.
4852	Transverse Modes in Gap-Coupled Surface Wave Devices	S.A. Reible	Accepted by Appl. Phys. Lett.
4859	An Acoustoelectric SAW/CCD Buffer Memory Device	D.L. Smythe R.W. Ralston B.E. Burke E. Stern	Accepted by Appl. Phys. Lett.
4862	Efficient Thallium Photodissociation Laser	D.J. Ehrlich J. Maya* R.M. Osgood, Jr.	Accepted by Appl. Phys. Lett.
4872	Frequencies, Line Strengths, and Assignments in the Doppler-Limited Spectrum of Formaldehyde from 2700-3000 cm^{-1}	L.R. Brown* R.H. Hunt* A.S. Pine	Accepted by J. Mol. Spectrosc.
4875	Vibrational Kinetics of SF_6 Dissolved in Simple Cryogenic Liquids	S.R.J. Brueck T.F. Deutsch R.M. Osgood, Jr.	Accepted by Chem. Phys. Lett.
4877	Energy Extraction from Metastable Excimers – Hg_2 as an Energy Storage Medium	D.J. Ehrlich R.M. Osgood, Jr.	Accepted by IEEE J. Quantum Electron.
4879	Enhancement of Nonlinear Optical Processes with a Double-Pass Tight-Focusing Geometry	S.R.J. Brueck H. Kildal	Accepted by Appl. Phys. Lett.
4880	Electrode Materials for the Photoelectrolysis of Water	J.G. Mavroides	Accepted by Mater. Res. Bull.
4883	Effect of H_2 on Residual Impurities in GaAs MBE Layers	A.R. Calawa	Accepted by Appl. Phys. Lett.
4884	Time and Magnetic Field Dependence of the Nickel Carbonylation Rate	R.S. Mehta* M.S. Dresselhaus* G. Dresselhaus* H.J. Zeiger	Accepted by Surf. Sci.

* Author not at Lincoln Laboratory.

JA No.			
4886	Spectral Intensities in the ν_3-Bands of $^{12}CH_4$ and $^{13}CH_4$	M. Dang-Nhu* A.S. Pine A.G. Robiette*	Accepted by J. Mol. Spectrosc.
4887	Beryllium Ion Implantation in InP and $In_{1-x}Ga_xAs_yP_{1-y}$	J.P. Donnelly C.A. Armiento	Accepted by Appl. Phys. Lett.
4888	Collision Induced Predissociation in Photoassociated Hg_2	D.J. Ehrlich R.M. Osgood, Jr.	Accepted by Chem. Phys. Lett.
4890	P-n Junction Diodes in InP and $In_{1-x}Ga_xAs_yP_{1-y}$ Fabricated by Beryllium Ion Implantation	C.A. Armiento J.P. Donnelly S.H. Groves	Accepted by Appl. Phys. Lett.
4893	Efficient Frequency Tripling of CO_2 Laser Radiation in Tandem $CdGeAs_2$ Crystals	N. Menyuk G.W. Iseler	Accepted by Opt. Lett.

Meeting Speeches†

MS No.			
4447C	Doppler-Limited Infrared Molecular Spectroscopy with a Tunable-Laser Difference-Frequency Converter	A.S. Pine	Seminar, Pennsylvania State University, University Park, 21 September 1978
4542B	Recent Advances in Laser Devices	A. Mooradian	Latin American Seminar on the Laser and Applications, La Plata, Argentina, 21-26 August 1978
4650A	Efficient cw Optically Pumped Ni:MgF_2 Laser	P.F. Moulton	Seminar, M.I.T., 28 September 1978
4654	Advances in GaAs Schottky Diode Submillimeter Heterodyne Receivers and Radiometers	P.E. Tannenwald	AGARD Symp. on Millimetre and Submillimetre Wave Propagation and Circuits, Munich, Germany, 4-8 September 1978
4689E	Fabrication and Applications of Submicron Structures	H.I. Smith D.C. Flanders M.W. Geis	Dry Etching Seminar, Danvers, Massachusetts, 10-11 October 1978
4701A	Solid State Electrochromic Displays Using Solid Electrolytes	M. Bayard	Gordon Research Conf., Tilton, New Hampshire, 31 July – 4 August 1978

* Author not at Lincoln Laboratory.

† Titles of Meeting Speeches are listed for information only. No copies are available for distribution.

MS No.			
4709A	Performance Requirements for Analog Signal Processors in Radar and Communication Systems	E. Stern	Society of Photo-Optical Instrumentation Engineers, 22nd Intl. Symp., San Diego, California, 28-31 August 1978
4802	Vibrational Kinetics in Cryogenic Liquids and Applications to Nonlinear Optics	S.R.J. Brueck T.F. Deutsch H. Kildal R.M. Osgood, Jr.	
4741	SAW/CCD Buffer Memory	D.L. Smythe R.W. Ralston E. Stern B.E. Burke	1978 Intl. Conf. on the Application of Charge Coupled Devices, San Diego, California, 25-27 October 1978
4744	Structural Aspects of Solid Electrolytes	H.Y-P. Hong	American Chemical Society, Miami, Florida, 12-13 September 1978
4745	Development of NASICON, a Solid Electrolyte for High-Temperature Sodium Batteries	J.A. Kafalas	
4750	Oscillatory Magneto-Transmission of $In_{1-x}Ga_xAs_yP_{1-y}$ Alloys	K. Alavi* R.L. Aggarwal* S.H. Groves	First Intl. Conf. on Solids and Plasmas in High Magnetic Fields, M.I.T., 18-20 September 1978
4754	Growth of Undoped InP and $In_{1-x}Ga_xAs_yP_{1-y}$ by LPE	S.H. Groves M.C. Plonko	1978 Intl. Symp. on GaAs and Related Compounds, St. Louis, Missouri, 24-27 September 1978
4756	Properties of InP Doped with Fe, Cr, or Co	G.W. Iseler	
4779	Annealing of Se-Implanted GaAs and InP by Scanned Nd:YAG Laser Irradiation	J.C.C. Fan J.P. Donnelly C.O. Bozler R.L. Chapman	
4757	An Acoustoelectric Schottky-Diode Memory-Correlator Subsystem	D.H. Hurlburt R.W. Ralston R.P. Baker E. Stern	1978 Ultrasonics Symp., Cherry Hill, New Jersey, 25-27 September 1978
4758	Acoustoelectric Signal-Processing Devices with Charge Storage	J.H. Cafarella	
4759	Automated Pulsed Technique for Measuring the Phase and Amplitude Response of SAW Devices	J.H. Holtham R.C. Williamson	
4760	Gap-Coupled InSb/$LiNbO_3$ Convolver Operating at 77 K	F.J. Leonberger R.W. Ralston S.A. Reible	

* Author not at Lincoln Laboratory.

MS No.			
4761	Interaction of Surface Waves and Bulk Waves in Gratings: Phase Shifts and a New Type of Resonance	J. Melngailis R.C. Williamson	1978 Ultrasonics Symp., Cherry Hill, New Jersey, 25-27 September 1978
4762	Transverse Modes in Acoustoelectric Convolvers	S.A. Reible K.L. Wang* V.S. Dolat	
4763	High-Performance Hybrid SAW Chirp-Fourier-Transform System	V.S. Dolat M.B. Schulz L.A. Veilleux G.R. McCully R.C. Williamson	
4766	Fast Synchronization in a Spread-Spectrum System Based on Acoustoelectric Convolvers	D. Brodtkorb J.E. Laynor	
4767	An Acoustoelectric SAW/CCD Device	D.L. Smythe R.W. Ralston B.E. Burke E. Stern	
4777	GaInAsP/InP Lasers and Detectors for Fiber Optics Communications at 1.0-1.6 μm	C.E. Hurwitz J.J. Hsieh J.N. Walpole S.H. Groves	EASCON '78, Washington, D.C., 24-27 September 1978
4777A	GaInAsP/InP Lasers and Detectors for Use at 1.0-1.6 μm	C.E. Hurwitz J.J. Hsieh J.N. Walpole S.H. Groves	Electrooptics/Laser '78 Conf., Boston, 19-21 September 1978
4780	mm-Wave Integrated Circuits for Strategic Sensors	R.W. Laton W.E. Courtney R.A. Murphy C.O. Bozler H.J. Stalzer G.B. Jones	Gov't Microcircuits Applications Conf., Monterey, California, 14-16 November 1978
4793	Zn-Diffused, Stripe-Geometry, Double-Heterostructure GaInAsP/InP Diode Lasers	J.J. Hsieh	6th IEEE Intl. Semiconductor Laser Conf., San Francisco, California, 29 October – 3 November 1978
4796	Condon Internal Diffraction in the Bound-Free Fluorescence of Photoassociated Heavy Metals	D.J. Ehrlich R.M. Osgood, Jr.	Laser Induced Processes in Molecules Conf., Heriot-Watt University, Edinburgh, Scotland, 20-22 September 1978
4796A	Collision Induced Predissociation in Photoassociated Hg_2	D.J. Ehrlich R.M. Osgood, Jr.	31st Annual Gaseous Electronics Conf., Buffalo, New York, 17-20 October 1978

* Author not at Lincoln Laboratory.

MS No.			
4802A	Vibrational Kinetics in Cryogenic Liquids and Applications to Nonlinear Optics	S.R.J. Brueck	Seminar, Los Alamos Scientific Laboratory, New Mexico, 28 August 1978
4809	Evaluation of High-Speed 9-12 Micrometer Detectors Using Sub-Nanosecond Pulsed Pb Salt Lasers	K.W. Nill* J.F. Butler* D.L. Spears	22nd Intl. Technical Symp., San Diego, California, 30 August 1978
4814	Millimeter Wave Mosaic Receiver	R.A. Murphy W.T. Lindley	4th Joint Strategic Sciences Mtg., San Diego, California, 13-15 September 1978
4818	Design Requirements for an Electrooptic A/D Converter	F.J. Leonberger C.E. Woodward D.L. Spears	High-Speed A/D Conversion Workshop, Portland, Oregon, 16-17 October 1978

* Author not at Lincoln Laboratory.

ORGANIZATION

SOLID STATE DIVISION

A. L. McWhorter, *Head*
I. Melngailis, *Associate Head*
C. R. Grant, *Assistant*

P. E. Tannenwald, *Senior Staff*

QUANTUM ELECTRONICS

A. Mooradian, *Leader*
P. L. Kelley, *Associate Leader*

Barch, W. E.
Belanger, L. J.
Blumberg, W. A. M.
Brueck, S. R. J.
Burke, J. W.
Chiao, R.*
Chinn, S. R.
DeFeo, W. E.
Deutsch, T. F.
Ehrlich, D. J.
Feldman, B.
Fetterman, H. R.
Fleming, M. W.†
Hancock, R. C.
Kildal, H.
Menyuk, N.
Moulton, P. F.
Osgood, R. M., Jr.
Parker, C. D.
Peck, D. D.
Pine, A. S.

APPLIED PHYSICS

A. G. Foyt, *Leader*
C. E. Hurwitz, *Associate Leader*
T. C. Harman, *Senior Staff*
R. H. Kingston, *Senior Staff*

Armiento, C. A.†
Calawa, A. R.
Carter, F. B.
DeMeo, N. L., Jr.
Diadiuk, V.
Donnelly, J. P.
Duffy, P. E.
Ferrante, G. A.
Glasser, L. A.†
Groves, S. H.
Leonberger, F. J.
Lind, T. A.
Maby, E. W.†
McBride, W. F.
Norris, P. E.†
Paladino, A. E.
Plonko, M. C.
Spears, D. L.
Tsang, D. Z.†
Walpole, J. N.

ELECTRONIC MATERIALS

A. J. Strauss, *Leader*
H. J. Zeiger, *Associate Leader*
J. G. Mavroides, *Senior Staff*

Anderson, C. H., Jr.
Bayard, M. L.
Button, M. J.
Chapman, R. L.
Davis, F. M.
Delaney, E. J.
Fahey, R. E.
Fan, J. C. C.
Finn, M. C.
Gale, R. P.
Gay, R. R.†
Hong, H. Y-P.
Hsieh, J. J.
Iseler, G. W.
Kafalas, J. A.
Kolesar, D. E.
Krohn, L., Jr.
Mastromattei, E. L.
Owens, E. B.
Palm, B. J.
Pantano, J. V.
Tracy, D. M.
Vohl, P.

SURFACE WAVE TECHNOLOGY

E. Stern, *Leader*
R. C. Williamson, *Associate Leader*

Baker, R. P.
Becker, R. A.
Brogan, W. T.
Cafarella, J. H.
Dolat, V. S.
Holtham, J. H.
Hurlburt, D. H.
Keman, W. C.
LaFleur, W. J.
Melngailis, J.
Oates, D. E.
Ralston, R. W.
Reible, S. A.
Slattery, R. L.
Withers, R. S.
Yao, I.

MICROELECTRONICS

W. T. Lindley, *Leader*
F. J. Bachner, *Associate Leader*
H. I. Smith, *Assistant Leader*

Alley, G. D.
Bozler, C. O.
Burke, B. E.
Chiang, A. M.
Clifton, B. J.
Daniels, P. J.
DeGraff, P. D.
Durant, G. L.
Eastman, L. F.
Efremow, N., Jr.
Elta, M. E.
Felton, B. J.
Flanders, D. C.
Geis, M. W.
Gopinath, A.
Gray, R. V.
Hansell, G. L.†
Hawryluk, A. M.†
Lincoln, G. A., Jr.
McGonagle, W. H.
Mountain, R. W.
Murphy, R. A.
Pichler, H. H.
Shaver, D. C.†
Silversmith, D. J.
Smythe, D. L., Jr.
Sotomayer-Diaz, O.
Turner, G. W.
Wilde, R. E.

---

* Summer staff

† Research assistant

I. SOLID STATE DEVICE RESEARCH

A. BERYLLIUM-ION IMPLANTATION IN InP AND $In_{1-x}Ga_xAs_yP_{1-y}$

Ion implantation will almost certainly play a significant role in the fabrication of optoelectronic devices in InP and $In_{1-x}Ga_xAs_yP_{1-y}$. Some preliminary results on both n- and p-type ion-implanted layers in InP have already been reported.[1-4] In this section we will present more-detailed information on Be-ion-implanted InP and report for the first time ion-implantation results in $In_{1-x}Ga_xAs_yP_{1-y}$. The results in InP include the effects of implant and anneal temperature on the electrical characteristics of the implanted layer and the effects of implanted Be-concentration on junction depth and, therefore, presumably indiffusion of the implanted Be. We will also report results on the use of a multi-energy Be-implant schedule designed to create a uniform-concentration p-type layer in both InP and $In_{1-x}Ga_xAs_yP_{1-y}$. The latter results are applicable to the fabrication of high-quality p-n junctions, which are reported in Sec. B below.

The InP samples used in these experiments were cut from pulled single crystals. High-resistivity (111) Fe-doped samples were used for initial experiments, and (100) n-type samples ($n \approx 2 \times 10^{16}$ cm^{-3}) were used for p-n junction measurements. After cutting and polishing, the InP samples were etched[5] in 1:1:5:1 mixture of $HAc:HClO_4:HNO_3:HCl$. The $In_{1-x}Ga_xAs_yP_{1-y}$ samples used were n-type [$n \approx (0.5 \text{ to } 1) \times 10^{16}$ cm^{-3}] epitaxial layers grown by liquid-phase epitaxy on (100) n^+-InP substrates.[6]

Beryllium was implanted into the etched surfaces of the InP samples and into the as-grown surfaces on the $In_{1-x}Ga_xAs_yP_{1-y}$ samples. Following implantation, two slightly different methods of encapsulation and anneal, which gave identical results on both implanted and control samples, were employed. Both methods rely on a pyrolytic phosphosilicate glass (PSG) encapsulation, nominally 7.84 wt% P, deposited at 250°C. Details of these methods and first-anneal sample processing can be found in Ref. 7.

For the first set of experiments, 400-keV Be^+ ions were implanted into Fe-doped substrates at temperatures ranging from room temperature to 200°C. Following implantation, the anneal temperatures used ranged from 500° to 750°C. Figure I-1 shows the sheet hole concentration and mobility vs anneal temperature for samples implanted at 150°C with 1×10^{14} cm^{-2} 400-keV Be^+ ions. Data for several samples implanted at room temperature are also shown and are in substantial agreement with 150°C data. As shown, there is a significant increase in the Be^+ activation between 500° and 600°C. Between 600° and 700°C, the sheet hole concentration increases from 2.6×10^{13} to 5.3×10^{13} cm^{-2}. Following a 750°C anneal, the sheet concentration in samples implanted at 150°C was 5.6×10^{13} cm^{-2}, while in samples implanted at room temperature it was slightly higher at 5.9×10^{13} cm^{-2}.

Figure I-2 shows the sheet hole concentration and mobility vs implant temperature for samples implanted with several different doses of 400-keV Be^+ ions and annealed at 750°C. The samples implanted with 3×10^{13} and 1×10^{14} cm^{-2} showed only a slight reduction in concentration with implant temperature. With a 3×10^{14} cm^{-2} implant, however, the sheet concentration in samples implanted at room temperature was about a factor-of-2 lower than in samples implanted at $\geq$100°C.

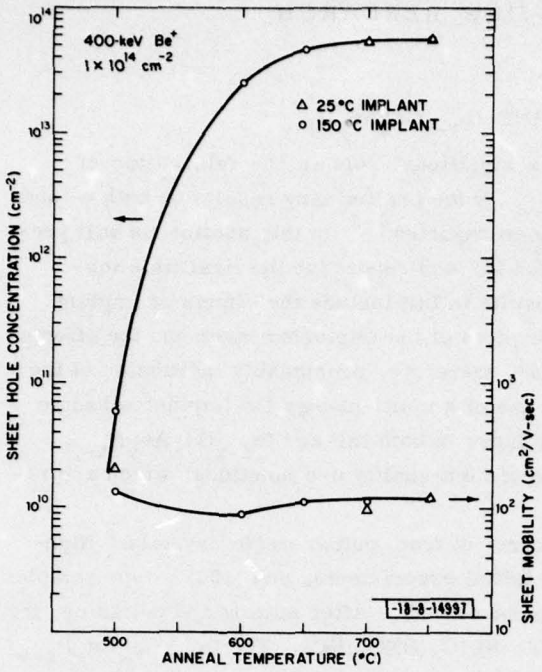


Fig. I-1. Sheet hole concentration and mobility vs anneal temperature for InP implanted with 1×10^{14} cm^{-2} 400-keV Be^+ ions.

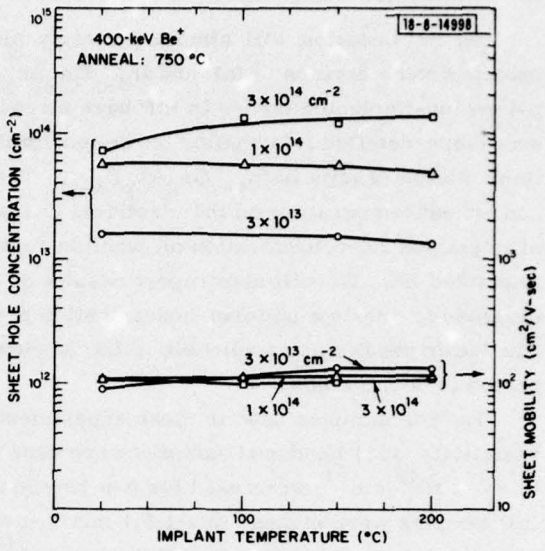


Fig. I-2. Sheet hole concentration and mobility vs implant temperature for InP implanted with 400-keV Be^+ ions.

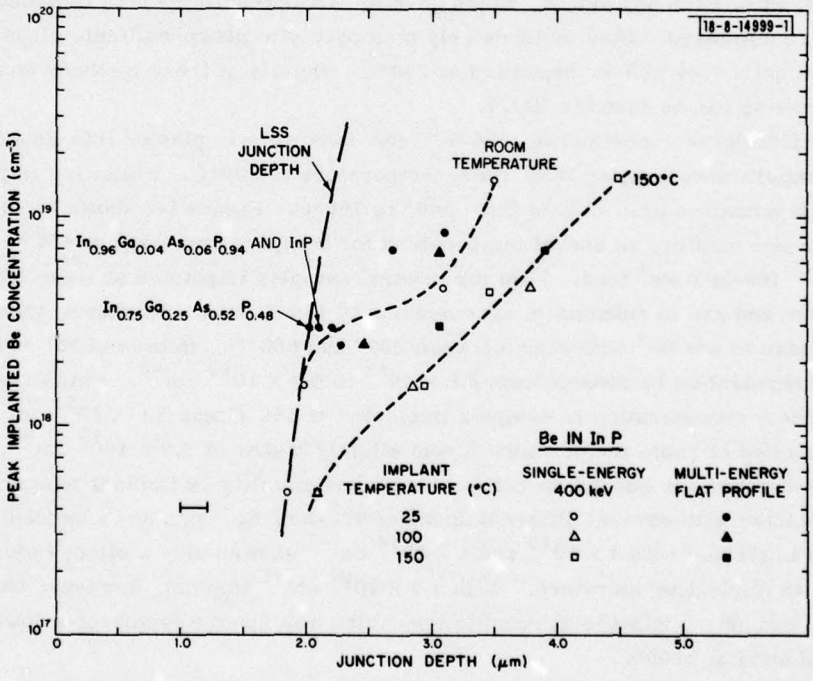


Fig. I-3. Junction depth vs maximum implanted Be concentration for 400-keV single- and multi-energy Be implants in InP and $In_{1-x}Ga_xAs_yP_{1-y}$.

To determine if these differences could be due to a Be-concentration dependent diffusion effect as has been observed in GaAs (see Refs. 8 through 11), the junction depths in a series of n-type InP ($n \approx 2 \times 10^{16}$ cm^{-3}) samples implanted with both a single-energy (400-keV) and a multi-energy Be implant schedule were determined. The multi-energy schedule was used since, in the actual fabrication of p-n junction diodes, some type of multiple implant would most likely be used to avoid the possibility of a buried p-type layer. The multi-energy schedule[12,13] used was designed to give a fairly uniform as-implanted Be concentration and was based on N at 400 keV, 12/18 N at 200 keV, 7/18 N at 100 keV, and 4/18 N at 50 keV, where N is the dose at 400 keV. For $N = 1.8 \times 10^{14}$ cm^{-2}, the uniform as-implanted Be concentration is about 3×10^{18} cm^{-3}. Following anneal and PSG removal, the samples were coated with ≈1000 Å of SiO_2 and then cleaved and preferentially etched in a KOH, $K_3Fe(CN)_6$ (potassium ferricyanide) solution to reveal the position of the p-n junction. The SiO_2-InP interface was used as the surface reference. The error in junction determination is estimated to be about 0.2 μm.

Figure I-3 shows the junction depth vs maximum implanted Be concentration (N_p) in InP samples implanted with either a single- or multi-energy implant schedule and annealed at 750°C. The maximum implanted Be concentration was calculated from the implanted dose using LSS range theory.[12,13] Also shown is the junction depth in several $In_{1-x}Ga_xAs_yP_{1-y}$ samples implanted with a multi-energy implant schedule and annealed at 700°C. Note that one of the InP data points falls right on top of an $In_{1-x}Ga_xAs_yP_{1-y}$ data point. The heavy dashed line represents the junction depth predicted from LSS theory[12,13] in $n \approx 2 \times 10^{16}$ cm^{-3} InP. The predicted junction depths for the quaternary samples are very close to this line (within 0.05 μm). The light dashed lines are drawn through the single-energy room-temperature and 150°C implant results. Except for possibly the lowest dose, 3×10^{13} cm^{-2} ($N_p = 4.7 \times 10^{17}$ cm^{-3}), the junctions depths in samples implanted at 100° and 150°C are significantly deeper than in similar samples implanted at room temperature. For the samples implanted at room temperature with a single-energy implant dose $\leq 1 \times 10^{14}$ cm^{-2} ($N_p \approx 1.6 \times 10^{18}$ cm^{-3}), the measured junction depths were identical to those predicted by LSS range theory, indicating insignificant indiffusion of the implanted Be. Samples implanted at room temperature with a multi-energy schedule, which resulted in an as-implanted concentration of 3×10^{18} cm^{-3}, exhibited junction depths which were within experimental error of that predicted by LSS theory. $In_{1-x}Ga_xAs_yP_{1-y}$ samples implanted to this level also showed insignificant Be indiffusion. Samples implanted to higher Be concentration showed increased junction depth. For some reason which is not yet fully understood, the junction depth in samples implanted with a multi-energy Be implant were generally shallower than the junction depths in samples implanted with a single 400-keV implant. From the data it appears that the maximum implanted Be concentration for a flat profile without significant indiffusion is about 3×10^{18} cm^{-3}. This result is qualitatively similar to results obtained on GaAs (see Refs. 8 through 11) and is in fairly good agreement with recently obtained SIMS measurements.[4]

Table I-1 summarizes the sheet carrier concentration and mobilities that have been obtained on n-type InP and $In_{1-x}Ga_xAs_yP_{1-y}$ samples implanted with the multi-energy Be schedule shown. This schedule should result in an as-implanted Be concentration of $\approx 3 \times 10^{18}$ cm^{-3}. For InP, the highest sheet concentration was obtained on samples implanted at room temperature and annealed at 750°C. As noted above, these samples showed insignificant indiffusion compared with samples implanted at 150°C which had a lower sheet concentration. These results may

TABLE I-1

MULTI-ENERGY BERYLLIUM IMPLANTS (FLAT PROFILE $\approx 3 \times 10^{18}$ Be cm^{-3}) IN InP AND $In_{1-x}Ga_xAs_yP_{1-y}$

Material	Implant Temperature (°C)	Anneal Temperature (°C)	N_s (cm^{-2})	μ_s (cm^2/V-sec)
InP	25	700	1.3×10^{14}	62
InP	25	750	2.2×10^{14}	66
InP	150	750	1.8×10^{14}	87
$In_{0.76}Ga_{0.24}As_{0.52}P_{0.48}$	25	700	1.2×10^{14}	82
$In_{0.75}Ga_{0.25}As_{0.52}P_{0.48}$	25	700	1.5×10^{14}	81

All samples implanted with 1.8×10^{14} cm^{-2} at 400 keV, 1.2×10^{14} cm^{-2} at 200 keV, 7.0×10^{13} cm^{-2} at 100 keV, and 4.0×10^{13} cm^{-2} at 50 keV.

indicate that outdiffusion to the surface also takes place when indiffusion is observed, as has been shown to take place in GaAs (see Ref. 10). Stripping measurements on a sample implanted at room temperature and annealed at 750°C indicate that the hole concentration is fairly uniform in the flat portion of the implanted region, with $p \approx (1.5 \text{ to } 2.0) \times 10^{18}$ cm^{-3}. Although the sheet concentrations obtained in quaternary samples which are annealed at 700°C are not as high as the best observed in InP, they are comparable to that obtained in the InP samples annealed at 700°C.

J. P. Donnelly
C. A. Armiento
G. A. Ferrante
S. H. Groves

B. P-N JUNCTION DIODES IN InP AND $In_{1-x}Ga_xAs_yP_{1-y}$ FABRICATED BY BERYLLIUM-ION IMPLANTATION

In this section we report results of p-n junction diodes formed by implantation of Be in n-type InP and $In_{1-x}Ga_xAs_yP_{1-y}$. Mesa and planar InP diodes, which exhibit low leakage currents and abrupt breakdowns, have been fabricated. In addition, $In_{1-x}Ga_xAs_yP_{1-y}$ ($E_g \approx 1.0$ eV) mesa diodes have been made which exhibit uniform breakdown over the area of the device.

InP samples were cut from (100) n-type ($n \approx 2 \times 10^{16}$ cm^{-3}) pulled single crystals. Prior to implantation, these samples were polished and etched[5] in a 1:1:5:1 mixture of $HAc:HClO_4:HNO_3:HCl$. $In_{1-x}Ga_xAs_yP_{1-y}$ samples were n-type [$n \approx (0.5 \text{ to } 1.0) \times 10^{16}$ cm^{-3}] epitaxial layers grown by liquid-phase epitaxy on (100) n^+ InP substrates.[6] Beryllium was implanted at room temperature into the etched InP surfaces and into the as-grown surfaces of the $In_{1-x}Ga_xAs_yP_{1-y}$ layers. Details of the implantation and anneal procedure can be found in Sec. A above and in Ref. 7.

Mesa diodes were fabricated by implanting the entire surface of the sample and subsequently etching mesas using a 1-percent bromine-methanol solution. Planar diodes were fabricated by implanting through holes opened in a 5-μm-thick layer of photoresist and a

2000-Å layer of pyrolytic SiO_2. In both structures, ohmic contacts to the p-type Be-implanted layers were made using microalloyed evaporated Au-Mg. Contacts to the back of the n-type substrates were made using microalloyed Au-Sn.

Initial diodes were fabricated using the following multi-energy Be implant schedule: 1.8×10^{14} cm^{-2} at 400 keV, 1.2×10^{14} cm^{-2} at 200 keV, 7×10^{13} cm^{-2} at 100 keV, and 4×10^{13} cm^{-2} at 50 keV. According to LSS range theory,[12,13] this implant schedule should yield a fairly uniform as-implanted Be concentration of 3×10^{18} cm^{-3} and a junction depth of 2 μm. Measurement of the hole concentration in the implanted region and the junction depth have shown that this implant schedule results in insignificant indiffusion of the implanted Be (see Sec. A above).

Figures I-4(a) and (b) show the I-V characteristics of a 10-mil-diam mesa and a 15-mil-diam planar InP diode, respectively, fabricated using the above implant schedule. Leakage current in both diodes is in the subnanoampere range for reverse biases out to more than 10 V. Near breakdown, the etched mesa diodes exhibited significantly more leakage current than the planar diode. A possible explanation (but not necessarily the correct one) is that the planar diodes had a pyrolytic SiO_2 layer over the exposed junction which may have provided some surface passivation.

Similar mesa diodes fabricated in a 6-μm-thick layer of $In_{0.75}Ga_{0.25}As_{0.52}P_{0.48}$ ($n \approx 8 \times 10^{15}$ cm^{-3}) exhibited breakdown voltage as high as 92 V. Figure I-5 shows the effective concentration vs depletion width of such an $In_{0.75}Ga_{0.25}As_{0.52}P_{0.48}$ diode obtained from capacitance-voltage measurements. Using the abrupt depletion model, the effective concentration (N_{eff}) is equal to $N_A N_D/(N_A + N_D)$, where N_A and N_D are the net ionized acceptor and donor concentrations, respectively, at the edge of the depletion region. In the situation where $N_A \gg N_D$, N_{eff} vs depletion width is essentially a plot of net donor concentration as a function of distance. Figure I-5 indicates that the p-n junction is fairly abrupt. Although an exact fit has not been obtained, the slight grading that is observed is about what is expected from the as-implanted Be profile (which to first order falls off with a Gaussian shape).

To determine if breakdown in the etched-mesa InP and $In_{0.75}Ga_{0.25}As_{0.52}P_{0.48}$ diodes was due to uniform avalanche breakdown, scanned photoresponse measurements were performed using the 6328-Å line of a He-Ne laser. Although some of these diodes exhibited uniform photocurrent gains of up to 3, many diodes showed edge breakdown and/or an enhanced edge response. As might be expected, inspection of the mesas indicated that the slope of the mesa at the junction generally determined whether or not a diode showed these edge effects.

To eliminate these edge effects so that the intrinsic uniformity of the Be-implanted junctions could be determined, diodes with shallower junctions were made in a thin $In_{1-x}Ga_xAs_yP_{1-y}$ layer which was "punched-through" or fully depleted before breakdown. The shallow junctions permit more-reproducible etching of mesas with near-vertical walls at the junction, which minimize edge response and field crowding.[14] Punch-through operation further minimizes the effect of any residual field crowding.

The $In_{0.75}Ga_{0.25}As_{0.52}P_{0.48}$ layer used for these diodes was 4 μm thick and was implanted with Be doses of 6×10^{13} cm^{-2} at 70 keV and 5×10^{13} cm^{-2} at 50 keV. According to LSS range statistics, this implant schedule should yield a junction depth of 0.6 μm. However, cleaved, stained mesas indicate that some diffusion of Be has occurred, resulting in a junction depth of 1.2 to 1.5 μm.

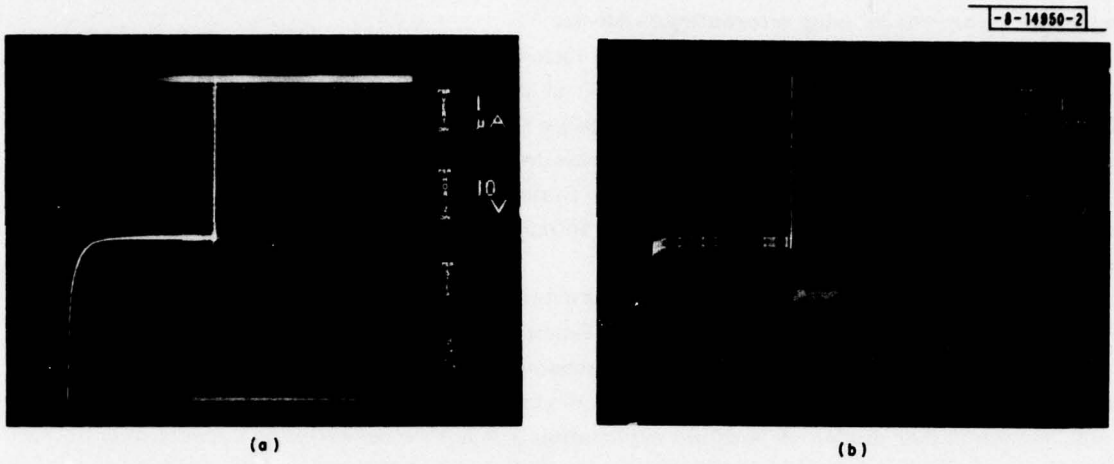


Fig. I-4. Current-voltage characteristics of Be-implanted InP diodes: (a) 10-mil-diam mesa diode, (b) 15-mil-diam planar diode.

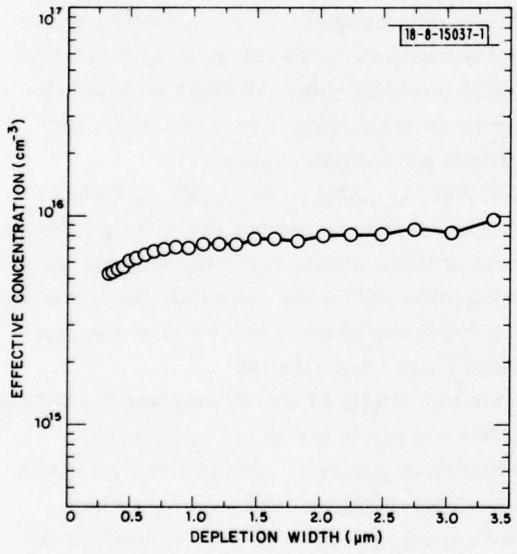


Fig. I-5. Effective concentration as a function of depletion width for an $In_{0.75}Ga_{0.25}As_{0.52}P_{0.48}$ mesa diode.

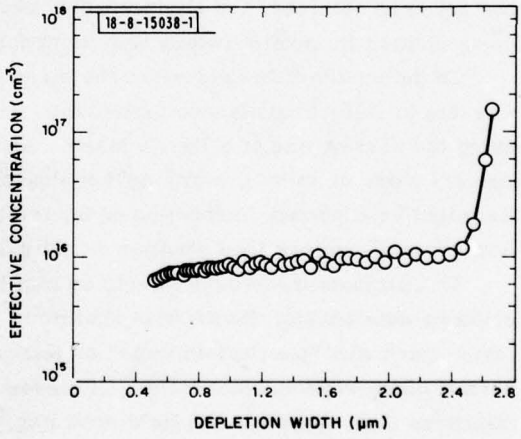


Fig. I-6. Effective concentration as a function of depletion width for an $In_{0.75}Ga_{0.25}As_{0.52}P_{0.48}$ punch-through mesa diode.

Figure I-6 shows the effective concentration vs depletion width obtained from capacitance-voltage measurements on a 10-mil-diam etched-mesa diode. Even though there was apparently some Be diffusion, these measurements indicate that the junction is still abrupt. The sudden increase in concentration at 2.5 μm indicates that the depletion region has reached through to the n^+-InP substrate. This punch-through occurs at 45 V, while breakdown occurs at 72 V.

Figures I-7(a) and (b) show the scanned photoresponse of one of these devices at a reverse bias of 69 V, which was taken using the 1.15-μm line of a He-Ne laser. Similar results were obtained using the 0.6328-μm line. Figure I-7(a) shows the photoresponse superimposed on the raster scan pattern, while (b) shows the horizontal scans superimposed on each other so that fluctuations in photoresponse are more easily detectable.

These scans indicate a uniform photoresponse gain of 2 (compared with the response at 50 V) over the entire area of the device, without any indication of edge response or edge breakdown. The depression in the photoresponse in the center of the device is due to the Au-Mg

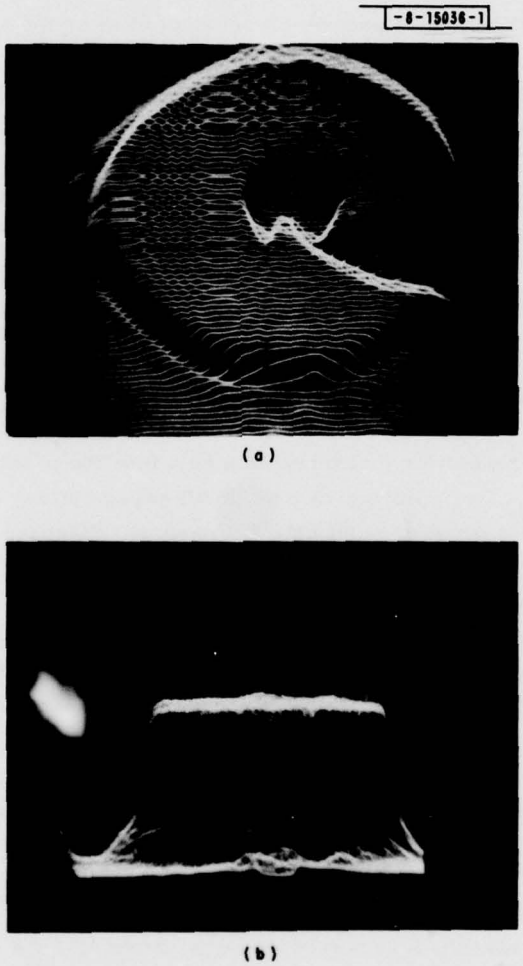


Fig. I-7. Photoresponse scans at 1.15 μm of an $In_{0.75}Ga_{0.25}As_{0.52}P_{0.48}$ punch-through mesa diode: (a) 3-dimensional display, (b) 2-dimensional display.

contact and the lead wire. These measurements indicate that junctions exhibiting uniform avalanche breakdown can be fabricated by Be-ion implantation.

C. A. Armiento
J. P. Donnelly
S. H. Groves

C. GROWTH OF NOMINALLY UNDOPED InP AND $In_{0.8}Ga_{0.2}As_{0.5}P_{0.5}$ ALLOYS

Two simple and reproducible liquid-phase epitaxial growth techniques have been used to grow InP and InGaAsP alloys with $N_D - N_A$ at the low 10^{15} cm^{-3} level. This represents nearly an order-of-magnitude reduction in net impurity concentration below that in growths made without "in situ" purification. The first growth technique uses $\sim 5 \times 10^{-7}$ atm of H_2O in the H_2 growth atmosphere to convert most of the Si in the growth solution to SiO_2. The second technique uses PH_3 as a source of P, but a bake prior to growth is necessary. Results similar to ours for this technique were reported earlier[15,16] but without an explanation of the purification mechanism. We have gathered evidence which suggests that H_2O is inadvertently added with the PH_3, and the purification in this process is accomplished by the same mechanism as in the H_2O-addition process.

Growth of InP with 77 K electron mobilities in the 40,000 to 60,000 cm^2/V-sec range, with N_D/N_A between 2.5 and 6, is readily achieved by either process. For $In_{0.8}Ga_{0.2}As_{0.5}P_{0.5}$, the 77 K mobilities are 12,000 to 14,000 cm^2/V-sec with $N_D/N_A \leq 2$. The H_2O-addition technique offers greater control and has given the lowest values of $N_D - N_A$. On the other hand, the PH_3-source technique offers the attractive side benefit of providing a protective partial atmosphere of phosphorus to prevent thermal etching of InP substrates. A fuller discussion of this work has been accepted for publication.[17]

S. H. Groves
M. C. Plonko

D. TRANSPORT PROPERTIES AND IMPURITY LEVELS OF InP AND $In_{0.8}Ga_{0.2}As_{0.5}P_{0.5}$

Hall-coefficient and resistivity measurements as a function of temperature have been made on InP and $In_{0.8}Ga_{0.2}As_{0.5}P_{0.5}$ alloys grown by liquid-phase epitaxy (LPE). These materials were grown with one of the "in situ" purification procedures discussed in Sec. C above, and they have net shallow impurity concentrations $N_D - N_A$ in the low 10^{15} cm^{-3} range. Low-magnetic-field measurements were made at H = 5 kG with an automatic measurement apparatus[18] for temperatures between 10 and 300 K. The effective electron concentration n was determined from the measured Hall coefficient R by assuming that the Hall-coefficient scattering factor r is unity: $n = r/Re = 1/Re$, where e is the electronic charge. These data are shown by dots on the main plots in Fig. I-8 for InP and in Fig. I-9 for an $In_{0.8}Ga_{0.2}As_{0.5}P_{0.5}$ alloy.

A fit of the extrinsic carrier activation to the data of Figs. I-8 and I-9 has been accomplished by first assuming a single-donor species, and second, by ignoring excited impurity states, as is appropriate to the range of purity considered here.[19] With these assumptions, the unknown parameters that determine the electron concentration are N_D, N_A, and E_D (the donor and acceptor concentrations and the donor activation energy, respectively). The quantity $N_D - N_A$ was estimated from the high-temperature n values in Figs. I-8 and I-9, and with this the separate values of N_D and N_A were found from a mobility analysis,[19] which is based on the assumption that at some temperature the mobility is entirely limited by ionized impurity

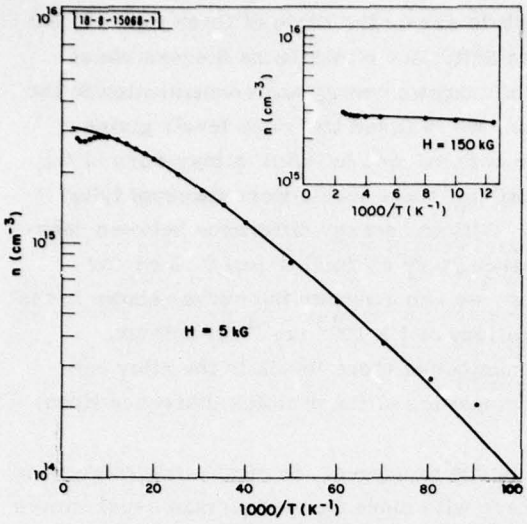


Fig. I-8. Effective electron carrier concentration vs 1000/T for InP. Solid curve is calculated using E_D = 3.7 meV. Insert shows high-magnetic-field data; curve is calculated using a deep-level concentration of 5×10^{15} cm^{-3} and energy of 0.29 eV.

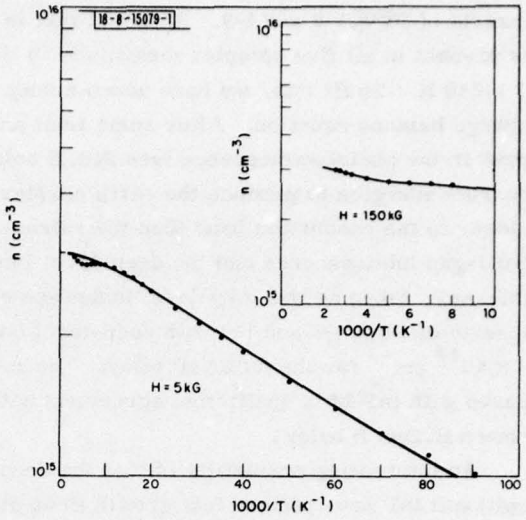


Fig. I-9. Effective electron carrier concentration vs 1000/T for $In_{0.8}Ga_{0.2}As_{0.5}P_{0.5}$. Solid curve is calculated using E_D = 0. Insert shows high-magnetic-field data; curve is calculated using a deep-level concentration of 3×10^{14} cm^{-3} and energy of 0.12 eV.

scattering. The conduction-band effective mass m_c^* and static dielectric constant ϵ_o used for this analysis are $m_c^* = 0.79\ m_o$ and $\epsilon_o = 12.4$ for InP, and $m_c^* = 0.061\ m_o$ and $\epsilon_o = 13.2$ for $In_{0.8}Ga_{0.2}As_{0.5}P_{0.5}$, where m_c^* for the alloy is taken from the magnetoabsorption results presented in Sec. F below, and ϵ_o for the alloy is estimated from an interpolation formula using the reported values of ϵ_o for GaAs, InP, InAs, and GaP. This procedure yielded the values $N_D = 3.7 \times 10^{15}$ cm^{-3} and $N_A = 6.0 \times 10^{14}$ cm^{-3} for the InP sample from the fit to the mobility at $T \simeq 40$ K, and $N_D = 6.0 \times 10^{15}$ cm^{-3} and $N_A = 3.0 \times 10^{15}$ cm^{-3} for the alloy from the fit to the mobility at $T \simeq 20$ K. With these values of N_D and N_A in the charge neutrality equation, E_D was adjusted to give an acceptable fit of calculated to measured electron concentration. The curves in the main portion of Figs. I-8 and I-9 give the calculated curve for InP with E_D = 0.0037 eV, and for $In_{0.8}Ga_{0.2}As_{0.5}P_{0.5}$ with $E_D \simeq 0$, respectively. Boltzmann statistics are adequate for the InP case, but Fermi-Dirac statistics are necessary for the charge neutrality calculation in the case of the alloy. The deviation of the experimental points from the calculated curve at low temperatures, especially apparent in Fig. I-8, is due to the onset of a competing conduction process such as impurity band conduction.

The behavior of the real electron concentration with temperature above 100 K for both the InP and InGaAsP alloys is obscured by the temperature dependence of the Hall-coefficient scattering factor due to the increasing importance of polar mode phonon scattering above that temperature, an effect that has been studied in the case of high-purity GaAs (see Ref. 20). To separate the carrier activation from scattering effects it is desirable to measure the Hall coefficient in the high-magnetic-field limit, in which the scattering factor is unity. Measurements have been taken at the National Magnet Laboratory with $H \simeq 150$ kG, well into the high-field regime, for temperatures between 100 and 400 K, and the resulting data are plotted in the

inserts of Figs. I-8 and I-9. An effect that is difficult to see on the scale of these figures, but is present in all five samples measured, is the extra activation of electrons discernible at $T > 250$ K. To fit this, we have added a deep level of unknown energy and concentration to the charge balance equation. After some trial and error, we realized that deep levels giving a peak in the photoluminescence (see Sec. E below) for both InP and InGaAsP alloys were of the correct energies to produce the extra carrier activation if these levels were taken as lying closer to the conduction band than the valence band. With the energy difference between near-band-gap luminescence and the deep-level luminescence, 0.29 eV for InP and 0.12 eV for InGaAsP, taken as the deep-level ionization energies, we can generate the curves shown in the inserts of Figs. I-8 and I-9 with deep-level concentrations of 5×10^{15} cm^{-3} for InP and 3×10^{14} cm^{-3} for the InGaAsP alloy. The reduced number of these levels in the alloy compared with InP is in qualitative agreement with the intensities of the photoluminescence lines, shown in Sec. E below.

An interesting possibility is that the deep level is due to oxygen. Several workers growing epitaxial InP have noticed that growth in an atmosphere with more O_2 or H_2O than usual causes an increase in the ratio of electron concentration at 300 K to that at 77 K, n_{300}/n_{77}. This effect may be caused by an increased number of these deep levels, although it is recognized that the concentration and ionization energy of the shallow donors as well as the compensation – factors that may vary with the O_2 or H_2O concentration in the growth tube atmosphere – also affect the quantity n_{300}/n_{77}.

S. H. Groves

E. PHOTOLUMINESCENCE OF InP AND $In_{0.8}Ga_{0.2}As_{0.5}P_{0.5}$ ALLOYS

A preliminary study has been made of photoluminescence from nominally undoped InP and $In_{0.8}Ga_{0.2}As_{0.5}P_{0.5}$ alloys grown by liquid-phase epitaxy (LPE). This study has been done with the samples at 77 K and with an apparatus selected for ease of operation over a broad range of photon energies, 0.3 to 1.6 eV, at some sacrifice of resolution. A krypton laser has provided photoexcitation of 0.5 W at 0.6741 μm wavelength. The luminescent radiation has been passed through a prism monochromator and imaged on a thermoelectrically cooled PbS detector.

Figure I-10 shows the luminescence intensity vs photon energy for a sample with electrical characteristics $N_D - N_A = 2.8 \times 10^{15}$ cm^{-3} and $\mu_{77} = 3.7 \times 10^4$ cm^2/V-sec, where $N_D - N_A$ is the net impurity concentration and μ_{77} is the electron mobility at 77 K. The peak at ~1.4 eV involves transitions to shallow donors and acceptors and, with higher resolution, would separate into: (1) a sharp, high-intensity peak at 1.4 eV due to band-to-band and shallow-donor-to-valence-band transitions, (2) a weaker peak 35 to 40 meV below the 1.4-eV peak and due to conduction-band-to-shallow-acceptor transitions, and (3) possibly a transition 75 to 80 meV below the 1.4-eV peak and very much weaker. These details can be seen in the spectra reported by workers at the Royal Radar Establishment[21] for LPE grown samples measured at 77 K and in work we have done[22] in an apparatus with higher resolution and with the samples near 4 K. Very-high-resolution near-gap luminescence has been reported for LPE InP samples at 1.8 K by Hess et al.[23]

The second peak in Fig. I-10, at 1.12 eV, is probably of the same origin as the broad peak at 1.17 eV in Ref. 21. This was seen in most, but not all, of the undoped LPE material investigated in that study and was seen in the bottom portion of their undoped, melt-grown InP crystals. The hypothesis was made in Ref. 21 that this line comes from impurity/P-vacancy complexes. From our analysis of extrinsic carrier activation discussed in Sec. D above, we believe that this

transition involves a level located ~0.3 eV below the conduction band. As mentioned above, an investigation is under way to test the hypothesis that this level is due to oxygen.

The lowest energy peak in Fig. I-10 occurs at 0.49 eV. Later runs with this apparatus were extended to 0.3 eV, and all samples showed, in addition, a similar type of transition at 0.35 eV. On the basis of an electron spin resonance analysis,[24] the 0.35-eV line has been assigned to an intra-center transition between the five T_2 and five E levels of the Fe^{2+} ($3d^6$) impurity. The origin of the 0.49-eV level is not known but may be radiation from a higher excited level of the Fe^{2+} manifold. Our undoped layers, 5 to 10 μm thick, were grown on the Fe-doped InP substrates. However, the profile of the Fe in the sample and the source of the Fe giving rise to the photoluminescence lines have not been determined.

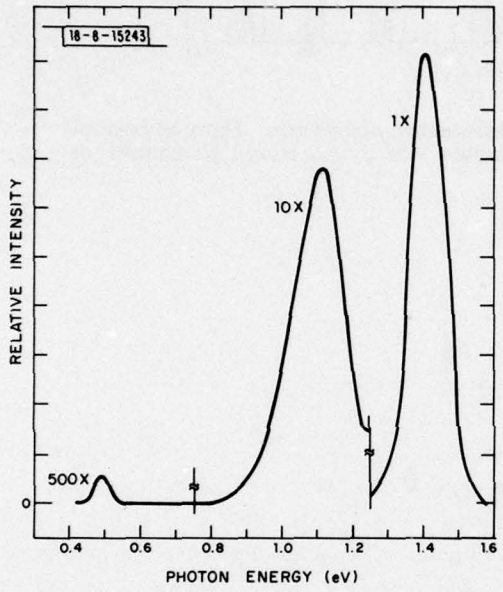


Fig. I-10. Photoluminescence spectrum for undoped InP grown by LPE.

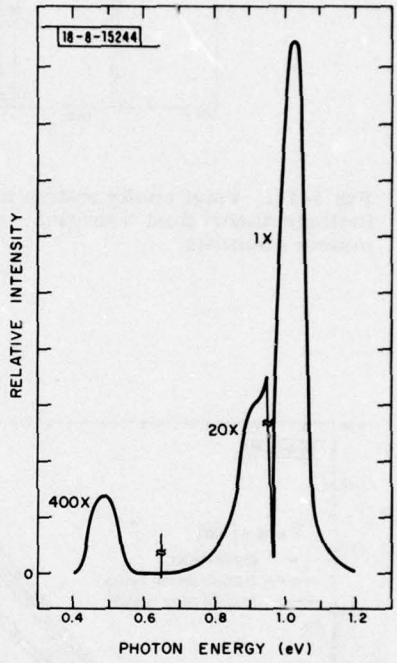


Fig. I-11. Photoluminescence spectrum for an undoped alloy of $In_{0.8}Ga_{0.2}As_{0.5}P_{0.5}$ grown by LPE.

Figure I-11 shows the luminescence spectrum for an $In_{0.8}Ga_{0.2}As_{0.5}P_{0.5}$ alloy with electrical characteristics $N_D - N_A = 5.8 \times 10^{15}$ cm^{-3} and $\mu_{77} = 1.2 \times 10^4$ cm^2/V-sec. The relative intensity scales in Figs. I-10 and I-11 are not necessarily the same, but probably are within a factor of 2 of each other. The main difference between the traces in Figs. I-10 and I-11, other than the energy shift due to the smaller bandgap of the alloy, is the reduced intensity in the second peak of Fig. I-11. Again, from the extrinsic activation analyses above, we attribute this line to a level located 0.12 eV below the conduction band. The reduced concentration of this level in the alloy compared with that in InP is in qualitative agreement with the results of Sec. D above.

S. H. Groves
J. G. Mavroides
D. F. Kolesar

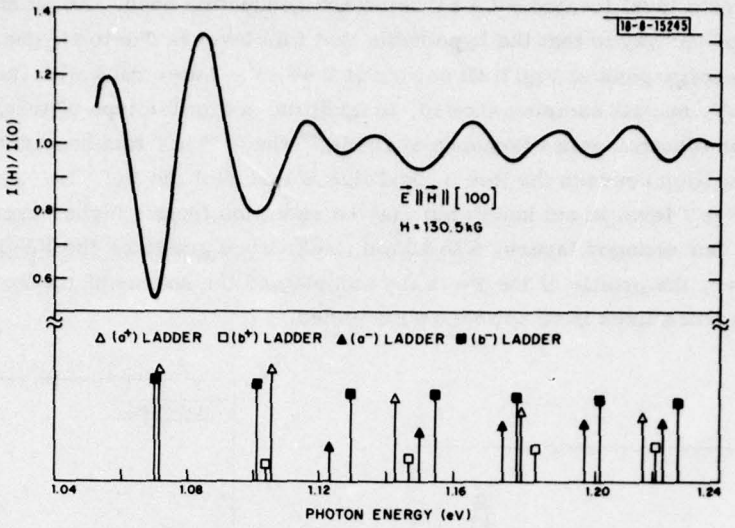


Fig. I-12. Voigt configuration magneto-transmission spectrum. Bars at bottom indicate theoretical energies, and their heights are proportional to square of matrix elements.

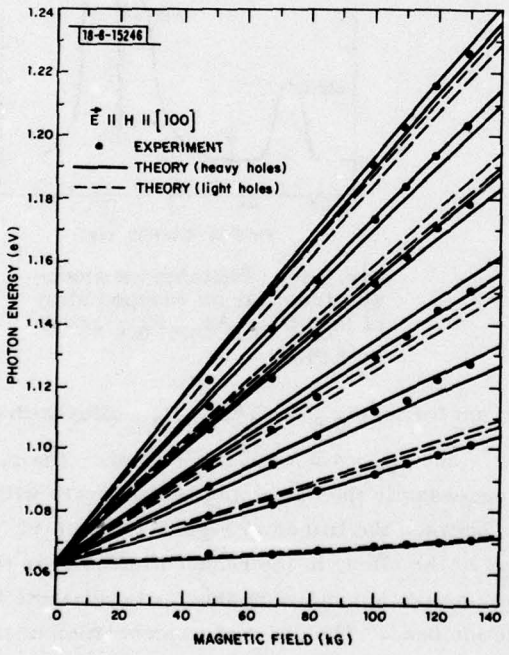


Fig. I-13. Transmission minima vs magnetic field. Theoretical curves include estimated excitation binding energy, which at H = 0 is 3 meV.

F. INTERBAND MAGNETOOPTICAL MEASUREMENTS ON $In_{1-x}Ga_xAs_yP_{1-y}$ ALLOYS

Oscillatory interband magneto-transmission in the 1.2-μm wavelength region has been measured on samples of $In_{0.77}Ga_{0.23}As_{0.52}P_{0.48}$ grown by liquid-phase epitaxy on InP substrates. Figure I-12 shows the oscillatory transmission made in the Voigt configuration, $\vec{E} \parallel \vec{H} \parallel [100]$, for H = 130.5 kG, where $\vec{E}$ is the optical electrical field vector. The arrows show the energies and strengths of transitions predicted by the theory with band parameters determined from this study. Figure I-13 shows the spectrum generated by plotting energies of absorption minima vs H. The band parameters determined by the fit of theory to the experimental data are $E_g = 1.07$ eV, $m_c^* = 0.061\ m_o$, and $E_p = 17.6$ eV, where these parameters are, respectively, the direct energy gap at $T \approx 20$ K, the conduction-band effective mass, and the $\vec{k} \cdot \vec{p}$ interaction energy, proportional to the square of the momentum matrix element. We are presently extending the magnetooptical measurements both to other InGaAsP alloys lattice-matched to InP and to such techniques as electric-field-modulated magnetoreflection. A more-detailed report of this work has been accepted for publication.[25]

K. Alavi†
R. L. Aggarwal†
S. H. Groves

† Francis Bitter National Magnet Laboratory, M.I.T.

REFERENCES

1. J. P. Donnelly and C. E. Hurwitz, Appl. Phys. Lett. 31, 418 (1977), DDC AD-A050856/4.
2. D. Eirug Davies, J. P. Lorenzo, and T. G. Ryan, Solid-State Electron. 21, 981 (1978).
3. D. Eirug Davies, W. D. Putter, and J. P. Lorenzo, to appear in the December 1978 issue of the Journal of the Electrochemical Society.
4. W. J. Devlin, K. T. Ip, D. P. Leta, L. F. Eastman, G. H. Morrison, and J. Comas, presented at the 7th Intl. Symp. on GaAs and Related Compounds, St. Louis, Missouri, 24-27 September 1978.
5. R. Becker, Solid-State Electron. 16, 124 (1973).
6. S. H. Groves and M. C. Plonko, presented at the 7th Intl. Symp. on GaAs and Related Compounds, St. Louis, Missouri, 24-27 September 1978.
7. J. P. Donnelly and C. A. Armiento, to be published in Applied Physics Letters.
8. J. P. Donnelly, F. J. Leonberger, and C. O. Bozler, Appl. Phys. Lett. 28, 706 (1976), DDC AD-A028457/0.
9. J. Comas and L. Plew, J. Electron. Mater. 5, 209 (1976).
10. J. Comas, L. Plew, P. K. Chatterjee, W. V. McLevige, K. V. Vaidyanathan, and B. G. Streetman, in Ion Implantation in Semiconductors and Other Materials, F. Chernow, J. Borders, and D. Brice, Eds. (Plenum, New York, 1977), p. 141.
11. W. V. McLevige, M. T. Helix, K. V. Vaidyanathan, and B. G. Streetman, J. Appl. Phys. 48, 3342 (1977).
12. J. Lindhard, M. Scharff, and H. Schiott, K. Dan. Vidensk. Selsk., Mat.-Fys. Medd. 33, 1 (1963).
13. W. J. Johnson and J. F. Gibbons, Projected Range Statistics in Semiconductors (Stanford University Bookstore, Stanford, California, 1970).
14. R. L. Davies and F. E. Gentry, IEEE Trans. Electron Devices ED-11, 313 (1964).
15. M. G. Astles, F. G. H. Smith, and E. W. Williams, J. Electrochem. Soc. 119, 496 (1972).
16. R. Sankaran, G. A. Antypas, R. L. Moon, J. S. Escher, and L. W. James, J. Vac. Sci. Technol. 13, 932 (1976).
17. S. H. Groves and M. C. Plonko, in Gallium Arsenide and Related Compounds 1978 (Institute of Physics Conference Series), to be published.
18. Solid State Research Report, Lincoln Laboratory, M.I.T. (1978:1), p. 13, DDC AD-A056715.
19. G. E. Stillman and C. M. Wolfe, Thin Solid Films 31, 69 (1976), DDC AD-A024175/2.
20. G. E. Stillman, C. M. Wolfe, and J. O. Dimmock, J. Phys. Chem. Solids 31, 1199 (1970), DDC AD-714321.
21. J. B. Mullin, A. Royle, B. W. Straughan, P. J. Tufton, and E. W. Williams, J. Cryst. Growth 13/14, 640 (1972).
22. A. R. Calawa, J. V. Gormley, and S. H. Groves, unpublished results.
23. K. Hess, N. Stath, and K. W. Benz, J. Electrochem. Soc. 121, 1208 (1974).
24. W. H. Koschel, U. Kaufmann, and S. G. Bishop, Solid State Commun. 21, 1069 (1977).
25. K. Alavi, R. L. Aggarwal, and S. H. Groves, to be published in the Journal of Magnetism and Magnetic Materials.

II. QUANTUM ELECTRONICS

A. EMISSION CROSS SECTION AND FLASHLAMP-EXCITED NdP_5O_{14} LASER AT 1.32 μm

Stoichiometric neodymium materials[1-3] have been the subject of considerable investigation based on their potential application in efficient miniature solid state lasers. Their high Nd concentration causes efficient pump absorption, yielding high gain per unit volume, and their freedom from significant concentration quenching results in long fluorescent lifetimes. We have measured the emission cross section and the room-temperature flashlamp-pumped laser action of NdP_5O_{14} at 1.32 μm. Previous laser experiments on similar materials are either at the conventional 1.05-μm line[4] or have used Ar^+ (Ref. 5) or Kr^+ (Ref. 6) lasers as excitation sources. We also compared the 1.32-μm laser performance with that of the conventional 1.05-μm line. The effective emission cross section determined from fluorescence measurements was in good agreement with the value found from laser-threshold data. The single-crystal 1-mm^2 × 7-mm NdP_5O_{14} laser rod delivers a few millijoules multimode output energy per pulse at 1.32 μm, and the threshold is as low as 180 mJ of electrical input energy with a 0.4-percent transmitting output mirror. The 1.32-μm wavelength is attractive for optical fiber communications since at this wavelength transmission loss of silica fibers is low and the material dispersion is favorable.[7] The lasing resonant losses at 1.32 μm are negligible compared with those at 1.05 μm, since the $^4I_{13/2}$ lower laser level of the 1.32-μm line is about 3900 cm^{-1} above ground level. Other advantages compared with 1.05-μm operation are larger mode volumes at 1.32 μm and lower Rayleigh scattering loss. Compared with quaternary semiconductor diode lasers[8] at this wavelength, stoichiometric Nd lasers might be a feasible alternative because of smaller beam divergence, narrower laser linewidth, and higher output-pulse energies. Relative to its Nd:YAG counterpart, the wider linewidth of NdP_5O_{14} would have shorter modelocked pulse capabilities.

Single crystals of NdP_5O_{14} were grown from hot phosphoric acids in which the rare-earth oxide had been dissolved. Details of the crystal growth were reported previously.[9]

Fluorescence measurements were performed on NdP_5O_{14} samples excited by a chopped argon-ion laser at 5145 Å. The excitation radiation was focused on a 1.5-mm "c" plate of NdP_5O_{14} of 1-mm^2 cross-section area placed close to the entrance slit of the 0.25-m Jarrell-Ash spectrometer with a 590 grooves/mm grating blazed at 1.2 μm. After transmission through a long-pass filter, infrared fluorescence was detected by a room-temperature Ge photodiode of 400-MHz bandwidth and a lock-in amplifier. An unpolarized fluorescence spectrum at 1.32 μm is shown in Fig. II-1.

Overall system calibration of detector and spectrometer was carried out with a tungsten lamp, using the appropriate emissivity and blackbody curves. The calibration was further checked against the known specifications of the detector spectral response and the unpolarized grating efficiency. The effective emission cross section at 1.32-μm transition was determined by comparing the peak emission intensity of the 1.32-μm line with that at 1.05 μm, whose cross section is already known. The relation between the cross sections of the two transitions is approximately[10]

$$\frac{\sigma_1}{\sigma_2} \cong \left(\frac{\lambda_1}{\lambda_2}\right)^5 \frac{I_1}{I_2} \quad .$$

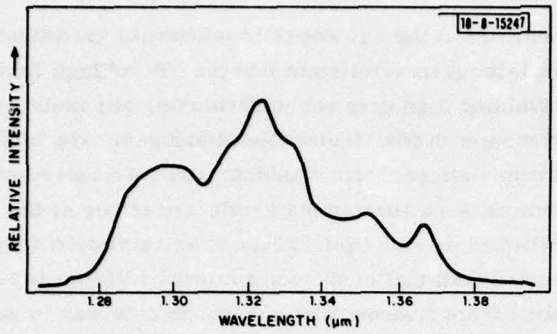


Fig. II-1. Unpolarized $^4F_{3/2} \rightarrow {}^4I_{13/2}$ fluorescence spectrum of NdP_5O_{14} at room temperature.

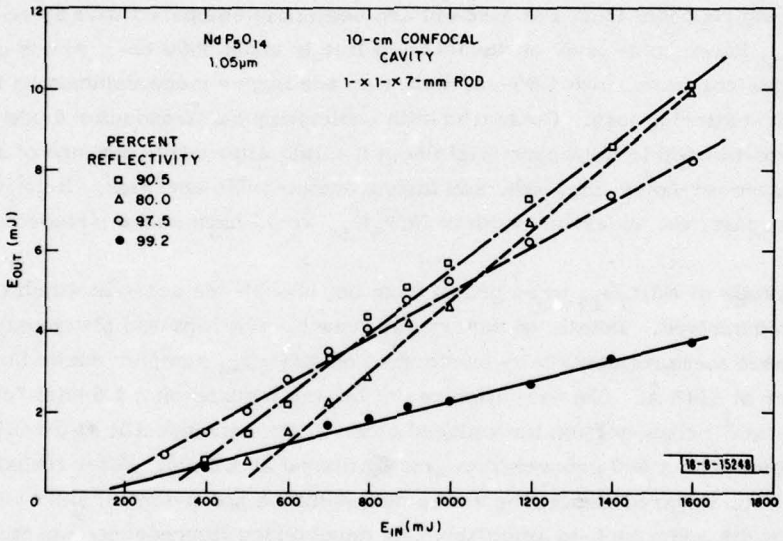


Fig. II-2. Laser output energy vs electrical input energy for NdP_5O_{14} as a function of output-mirror reflectivity at a wavelength of 1.05 μm.

As fluorescence data are compared under identical excitation conditions, reabsorption correction, which is of importance for thick samples,[11] was canceled out in the relative measurement. With the system calibration correction, a ratio of the 1.05- to 1.32-μm peak cross sections $\sigma_1/\sigma_2 = 5.6$ was obtained from the fluorescence data. By using a value of $\sigma_{1.05} = 2.5 \times 10^{-19}$ cm^2 at 1.05 μm (Ref. 12) the cross section at 1.32 μm was found to be $\sigma_{1.32} = 4.5 \times 10^{-20}$ cm^2.

Laser rods of NdP_5O_{14} were fabricated with "c" faces polished flat (λ/10) and parallel to 10 sec, and "a" and "b" faces fine ground. The fluorescence lifetime of the Nd^{3+} $^4F_{3/2}$ manifold was 135 μsec as measured by a N_2 laser pumped dye laser. The uncoated laser rod was placed inside an aluminum-coated reflector close to a Xe flashlamp which was driven by a single mesh circuit of 10-μF capacitance and 75-μH inductance described previously.[4] (The mode waists of the 10-cm confocal cavity are 129 and 183 μm at the crystal and mirrors, respectively.) The laser mirrors (Optasil) should have negligible absorption at 1.32 μm. Output mirrors of 99.6-, 99.0-, and 97.9-percent reflectivities at 1.32 μm were used in conjunction with a highly reflecting back mirror. All the dielectric coatings had >85-percent transmission at 1.05 μm. With the 99.0-percent reflecting mirror, an output energy of 1.5 mJ per pulse at a 1-Hz repetition rate was measured with a power meter. The laser linewidth at 1.32 μm was 14 cm^{-1} at 2-percent output coupling as measured by the Ge photodiode at the output slit of a 0.25-m Jarrell-Ash spectrometer. As in the case of 1.05-μm operation, the 1.32-μm laser polarization for the "c"-axis rod was along the "b" direction. With the 1-mm^2 × 7-mm laser rod, laser performance at 1.32 μm was compared with 1.05-μm operation under identical cavity configurations. With an output coupling of ~2 percent, the threshold energy at 1.32 μm was 340 mJ; with 2.5-percent coupling, that at 1.05 μm was 160 mJ. At this coupling level the multimode output energy per pulse was 2.7 and 8.2 mJ, respectively, with 1.6 J of electrical energy input. The slope efficiencies were 0.24 and 0.52 percent at 1.32 and 1.05 μm, as shown in Figs. II-2 and II-3. Total

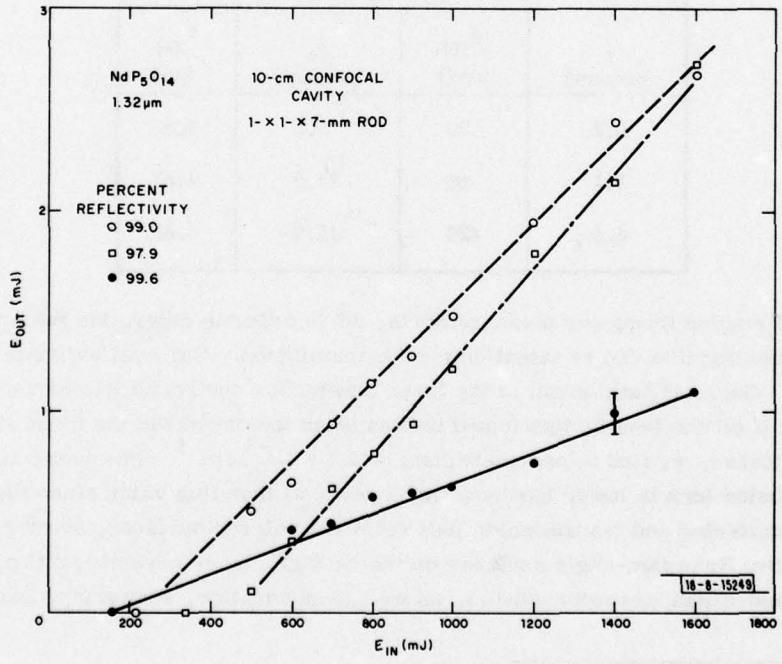


Fig. II-3. Laser output energy vs electrical input energy for NdP_5O_{14} as a function of output-mirror reflectivity at a wavelength of 1.32 μm.

internal cavity losses were estimated at 2 percent in both cases, with the 1.05-μm operation having an additional 3-percent resonant absorption loss, while that at 1.32 μm is negligible. From a comparison of the change in threshold energy with varying mirror transmission for both 1.05- and 1.32-μm operation, the ratio of $\sigma_1/\sigma_2 = 5.75$ was found. In this case, the ratio refers to the population-weighted "b" polarization cross sections rather than the presumably mixed polarization ratio given above. Using only the "b" polarized cross-section data,[12] $\sigma_{1.05}(b) = 1.6 \times 10^{-19}$ cm^2, giving $\sigma_{1.32}(b) = 2.8 \times 10^{-20}$ cm^2.

S. R. Chinn
M. M. Choy†
W. K. Zwicker†

B. Ni:MgF_2 LASER DEVELOPMENT

We have obtained 100 mW of CW output from a 3-mirror cavity Ni:MgF_2 laser described earlier,[13] and have observed extremely low crystal losses. Repetitive Q-switching of the laser has yielded power enhancements of $>10^3$, with peak power outputs of 20 W.

The laser crystal used in these experiments was doped with 1-wt% Ni and absorbed ~75 percent of the 1.33-μm pump radiation. With a 1.1-percent-transmission output mirror, we found a CW power output of 100 mW for an absorbed pump power of 1 W. Threshold absorbed powers P_{TH}, slope efficiencies Δ, and threshold wavelengths λ_{TH}, for three different output-mirror transmissions T, are given in Table II-1. We have compared the thresholds and slope efficiencies for the two lowest-transmission mirrors (for which the same λ_{TH} was observed) and we

TABLE II-1
Ni:MgF_2 LASER PERFORMANCE VS OUTPUT MIRROR TRANSMISSION

T (percent)	P_{TH} (mW)	Δ (percent)	λ_{TH} (μm)
0.2	20	5.5	1.67
1.1	68	11.5	1.67
6.6	420	15.0	1.62

have performed ringing frequency measurements, all in order to determine the total loss in the laser cavity excluding that due to output-mirror transmission. Our best estimate for this loss is 0.3 percent. The total path length in the laser crystal for one round trip of the cavity is 2.5 cm. Thus, if all the loss is distributed uniformly in the crystal in the form of absorption and scattering losses, we find a loss coefficient of 1.2×10^{-3} cm^{-1}. However, we feel that the Ni:MgF_2 distributed loss is lower (perhaps by 50 percent) than this value since the 0.3-percent loss includes scattering and transmission loss from two mirror surfaces, scattering and reflection loss from two Brewster-angle surfaces on the Ni:MgF_2 laser crystal and two Brewster surfaces on the fused-silica Brewster window, as well as absorption, scattering, and depolarization

† Philips Laboratories, Briarcliff Manor, New York.

losses in a 1-cm path of fused silica in the latter window. The ultimate limit for crystal loss, arising from phonon-assisted absorption processes, is roughly 4×10^{-5} cm^{-1} at 1.67 μm at 77 K.

Q-switching of the 3-mirror cavity Ni:MgF_2 laser was achieved using a 2.5-cm-long crystal of $LiNbO_3$ cut for Brewster-angle operation with optical propagation along the "z"-axis. The insertion loss of the Q-switch was unexpectedly high, about 3 percent, and was presumably due to strain-induced birefringence in the $LiNbO_3$. Thus, with a 1-percent-transmission output mirror, only 14 mW of CW output was observed at 1.62 μm for an absorbed pump power of 1 W. Roughly 200 V applied across the 5-mm-thick Q-switch was sufficient to turn the laser off. Q-switched output pulses observed by a high-speed HgCdTe photodiode, for a pulse repetition rate (PRR) of 100 Hz, are shown in Fig. II-4. Also shown in the figure is the voltage applied across the Q-switch. The peak and average power outputs at a 100-Hz PRR for 1 W of absorbed pump power were 20 W and 2.2 mW, respectively. At 1 kHz, peak and average power outputs changed to 4 W and 9.5 mW.

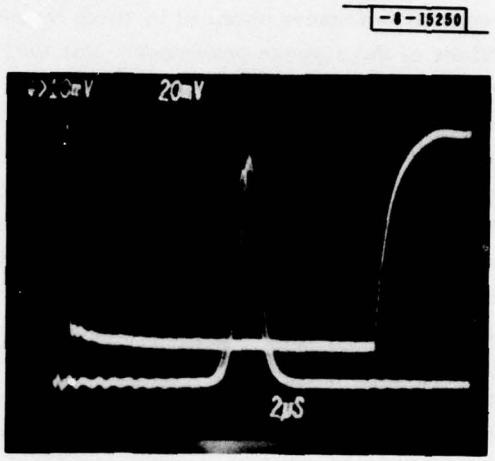


Fig. II-4. Q-switched pulses from Ni:MgF_2 laser along with voltage (~200 V) drive to $LiNbO_3$ Q-switch.

The power enhancement obtained by Q-switching, defined as the ratio of Q-switched peak power to CW power observed with no Q-switching, was 1.4×10^3 at a 100-Hz PRR. Computer calculations[14] of CW-pumped, repetitively Q-switched lasers predict for the system discussed here a power enhancement of 2.5×10^4. Some if not all of this discrepancy is related to the transient elastooptic effect, which is particularly noticeable in $LiNbO_3$ due to the large difference between static and dynamic electrooptic coefficients.[15,16] Essentially, the retardation of the Q-switch does not drop to zero as the voltage drops to zero, but oscillates at the mechanical resonance frequencies of the bulk crystal. Oscillations in crystals similar to the one we used have been observed with periods of about 1 μsec, lasting for >10 μsec (Ref. 16). Since our laser system performance was sensitive to small losses, the oscillations in the retardation of the Q-switch would noticeably affect the power enhancement. An acoustooptic Q-switch using fused silica as the interacting medium would likely provide better performance than we achieved with $LiNbO_3$, since the insertion loss could be much smaller, and there would be no problem with the transient elastooptic effect.

To summarize, we have observed $>10^3$ power enhancement in the Ni:MgF_2 laser by repetitive Q-switching, though even greater enhancements may be possible with a more-optimum Q-switch. The ability to achieve such large enhancements is an important property of the Ni:MgF_2 laser for applications involving nonlinear optical effects, such as frequency mixing and Raman shifting.

P. F. Moulton
A. Mooradian

C. HIGHER-ORDER NONLINEAR PROCESSES IN $CdGeAs_2$

We report observation of phasematched fourth-harmonic generation (FHG) in $CdGeAs_2$ using a CO_2 pump laser with a 140-nsec pulse duration. From the measurements, we determine an effective fourth-order susceptibility tensor which is much higher than previous theoretical estimates of the fourth-order tensor.[17,18]

Measurements of higher-order nonlinearities are complicated because of interference between the direct processes and cascade processes connected with lower-order nonlinearities. The susceptibility tensors obtained by these measurements are effective values that include the contributions of the cascade processes. For $CdGeAs_2$, the estimated contributions of these processes to the effective third- and fourth-order susceptibility tensors are comparable to the measured values.

Quantitative studies of higher-order nonlinear optical processes are important for the understanding of the nonlinear properties of dielectric media. Ninth-harmonic generation has recently been reported[19] in a gaseous sodium-argon mixture, and phasematched fourth- and fifth-harmonic generation in solids has been observed in lithium formate[20] and calcite,[21] respectively. These experiments were conducted in the visible and ultraviolet spectral regions with picosecond pump pulses from a modelocked Nd^{3+} glass laser. The present experiment is the first measurement of an effective fourth-order susceptibility tensor for an infrared material.

The interest in $CdGeAs_2$ during recent years derives from its large second-order nonlinear coefficient. The material is useful for frequency-doubling of CO_2-laser radiation, and energy conversion efficiencies as high as 27 percent have been reported.[22] Both its second-order[23,24] and effective third-order[25] nonlinear coefficients have been measured. Because it has the chalcopyrite structure (42-m symmetry), $CdGeAs_2$ has only two independent fourth-order nonlinear coefficients, $\chi^{(4)}_{xyzzz}$ and $\chi^{(4)}_{xyyyz} = \chi^{(4)}_{xxxyz}$ (Ref. 26).

$CdGeAs_2$ is one of the few infrared nonlinear materials with sufficient birefringence to allow phasematched FHG. Type I phasematching is satisfied at pump wavelengths longer than 9.7 μm, and type II phasematching is allowed at wavelengths between 12.4 and 15.2 μm (see Refs. 17 and 24). The type I phasematching condition can be stated as

$$n_4^o = n_1^e(\Theta) \qquad \text{(II-1)}$$

where o and e refer to ordinary and extraordinary waves, respectively, and Θ is the angle between the wavevector and the optic axis (z-axis). If ϕ is the azimuth angle between the x-axis and the projection of the wavevector in the x-y plane,[27] the fourth-order nonlinear coefficient for type I phasematching can be written as

$$\chi_I^{(4)}(\omega,\omega,\omega,\omega) = 2 \sin 2\Theta \cos 2\phi \left[\chi^{(4)}_{xyzzz} \sin^2\Theta + \chi^{(4)}_{xyyyz} \cos^2\Theta\right] . \qquad \text{(II-2)}$$

This expression is maximized for an input wave polarized either in the x-z or y-z plane ($\phi = 0$ or $\pi/2$, respectively).

A direct measurement of $\chi_I^{(4)}(\omega,\omega,\omega,\omega)$ is not possible because of interference between the direct FHG process and the two- and three-step cascade processes involving the lower-order nonlinearities $\chi^{(2)}$ and $\chi^{(3)}$. The cascade processes are automatically phasematched in the same direction [defined by Eq. (II-1)] as the direct process even though the individual cascade steps are generally not phasematched in the same direction.[28] The effective nonlinearity which is measured can therefore be written as[18]

$$\chi_{I,eff}^{(4)}(4\omega) = \chi_I^{(4)}(\omega,\omega,\omega,\omega) + b_1\chi^{(2)}(\omega,\omega)\,\chi^{(3)}(2\omega,\omega,\omega) + b_2\chi^{(3)}(\omega,\omega,\omega)\,\chi^{(2)}(3\omega,\omega) + b_3\chi^{(2)}(\omega,\omega)\,\chi^{(2)}(2\omega,\omega)\,\chi^{(2)}(3\omega,\omega) + b_4\,[\chi^{(2)}(\omega,\omega)]^2\,\chi^{(2)}(2\omega,2\omega) \quad . \tag{II-3}$$

The last term vanishes in the type I phasematching geometry that maximizes $\chi_I^{(4)}(\omega,\omega,\omega,\omega)$. In this case ($\phi = \pi/2$), Eq. (II-3) takes the specific form

$$\chi_{I,eff}^{(4)}(4\omega) = -2\sin 2\theta \left\{ \chi_{xyzzz}^{(4)}\sin^2\theta + \chi_{xyyyz}^{(4)}\cos^2\theta + \frac{3\chi_{xyz}^{(2)}}{4n_2^o\,[n_1^e(\theta) - n_2^o]\,\epsilon_o} \times [\chi_{xxzz}^{(3)}\sin^2\theta + \chi_{xxyy}^{(3)}\cos^2\theta] + \frac{\chi_{xyz}^{(2)}}{2n_3^e(\theta)\,[n_1^e(\theta) - n_3^e(\theta)]\,\epsilon_o} \times [\chi_{zzzz}^{(3)}\sin^4\theta + \chi_{xxxx}^{(3)}\cos^4\theta + 6\chi_{xxzz}^{(3)}\sin^2\theta\cos^2\theta] + \frac{[\chi_{xyz}^{(2)}]^3\sin^2 2\theta}{2n_3^e(\theta)\,n_2^o\,[n_1^e(\theta) - n_2^o]\,[n_1^e(\theta) - n_3^e(\theta)]\,\epsilon_o^2} \right\} \quad . \tag{II-4}$$

This equation is valid as long as the coherence lengths associated with the intermediate steps of the cascade processes are shorter than both the crystal length and the absorption length.

Two $CdGeAs_2$ crystals 2.7 and 3.8 mm long, referred to as A and B, were used in the experiments. Their measured absorption constants at liquid nitrogen temperature at 10.25 and 2.56 μm were, respectively, $a_1 = 0.1\ cm^{-1}$ and $a_4 = 4.4\ cm^{-1}$ for crystal A, and $a_1 = 1.9\ cm^{-1}$ and $a_4 = 9.5\ cm^{-1}$ for crystal B. Both crystals were cut for type I phasematching. The measured polarization of the fourth-harmonic output beam was perpendicular to the input-beam polarization, as expected for type I phasematching. Figure II-5 shows the measured wavelength dependence of the type I phasematching angle for FHG. The measured angles have an absolute uncertainty of ±1°. The figure also shows a phasematching curve calculated from refractive index data[24] taken at room temperature. Previously, we have shown that the phasematching angle for second-harmonic generation (SHG) of CO_2-laser radiation is only weakly temperature-dependent, varying by <1° between room temperature and liquid nitrogen temperature.[22] A stronger temperature dependence is expected for FHG since the fourth-harmonic wavelength is close to the wavelength corresponding to the $CdGeAs_2$ bandgap, which varies from 2.2 μm at room temperature to 1.9 μm at liquid nitrogen temperature.[29] The increased bandgap at liquid nitrogen temperature should reduce the indices of refraction at the fourth-harmonic wavelength,

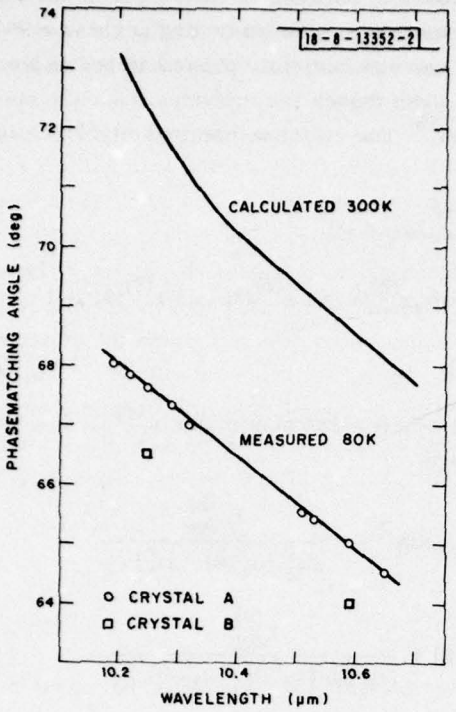


Fig. II-5. Type I phasematching angle for FHG in $CdGeAs_2$.

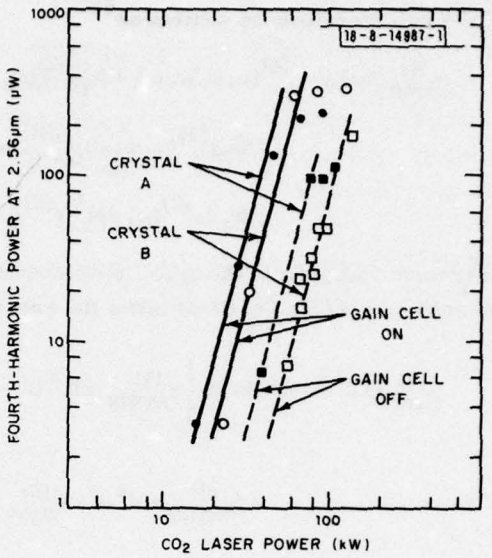


Fig. II-6. Input-output curve for FHG in $CdGeAs_2$ (spot size = 480 μm, lengths of 0.27 and 0.38 cm for crystals A and B, respectively).

TABLE II-2

MEASURED LINEAR AND NONLINEAR SUSCEPTIBILITIES OF $CdGeAs_2$

$\chi^{(1)}_{zz}/\epsilon_o = 12$	Refs. 23 and 24
$\chi^{(2)}_{xyz}/\epsilon_o = 6.1 \times 10^{-10}$ m/V	Refs. 23 and 31
$\chi^{(3)}_{II,eff}/\epsilon_o = 7.0 \times 10^{-18}$ m^2/V^2	Refs. 17 and 25
$\chi^{(4)}_{I,eff}/\epsilon_o = 7.9 \times 10^{-27}$ m^3/V^3	This work

and consequently lead to a smaller phasematching angle. In Fig. II-5, this effect is particularly evident at the shortest pump wavelengths where the measured phasematching angle is ~5° smaller than calculated. At 10.6 μm the difference is 3.5°, which is slightly larger than the difference of 2° for the phasematching angle of SHG with 10.6-μm radiation.

The measured fourth-harmonic output power at 2.56 μm vs input power at 10.24 μm for the two crystals with the gain cell on and off is shown in Fig. II-6. Turning the gain cell off resulted in partial modelocking of the laser pulse, increasing the conversion efficiency by 15 to 20 times. For the modelocked case, Fig. II-6 gives the average peak power. The conversion efficiency saturates at power levels approaching the laser-induced surface damage threshold. The saturation is less evident when the gain cell is on. This suggests an intensity-dependent effect. From the measured input-output curves in the case of no modelocking, we determine the effective fourth-order susceptibility tensor $\chi^{(4)}_{I,eff}$, in mks units, as 6.2×10^{-38} and 8.0×10^{-38} m^2As/V^4 for crystals A and B, respectively. In order to reduce the possibility of systematic errors, $\chi^{(4)}_{I,eff}$ for crystal A was also measured in another setup using a different laser and detector. The results of the two measurements agreed within 20 percent. From the experiments on both crystals, we obtain

$$\chi^{(4)}_{I,eff} = 7 \times 10^{-38} \frac{m^2As}{V^4} \pm 40 \text{ percent}$$

for $CdGeAs_2$.

The intrinsic breakdown thresholds in solids are determined by electron avalanche ionization,[30] which occurs at electric-field strengths of typically 10^8 V/m. To reach this intrinsic threshold in $CdGeAs_2$ probably requires CO_2-laser pulses shorter than 1 nsec. In Table II-2, the measured $\chi^{(4)}_{I,eff}/\epsilon_o$ is compared with the lower-order nonlinear susceptibilities. The higher-order terms in the expansion of the induced polarization do not exceed the lower-order terms even at the threshold for dielectric breakdown.

The interference terms for the fourth-order process can only be estimated, since the sign and magnitude of each $\chi^{(3)}_{iijj}$ component are not known. An upper bound can be determined using the reported $\chi^{(3)}_{eff}$ value for type II phasematching, keeping in mind that this value most likely is greater than the $\chi^{(3)}_{iijj}$ components because of the interference effects. The estimated contribution to $\chi^{(4)}_{I,eff}/\epsilon_o$ in Eq. (II-4) due to the cascade terms is 1.7×10^{-26} m^3/V^3, assuming $\chi^{(3)}_{iijj} \approx \chi^{(3)}_{iiii}/3 \approx \chi^{(3)}_{eff} > 0$. This is of the same order of magnitude as the measured value of $\chi^{(4)}_{I,eff}/\epsilon_o$.

The $\chi^{(4)}_I(\omega, \omega, \omega, \omega)/\epsilon_o$ for $CdGeAs_2$ has been theoretically estimated as 1.3×10^{-29} m^3/V^3 using a bond-orbital model,[17] and as 0.7×10^{-29} m^3/V^3 from a simple anharmonic-oscillator model.[18] These estimates are smaller than the measured $\chi^{(4)}_{I,eff}/\epsilon_o$ value by factors of almost 10^3. This suggests that the interference terms make the main contribution to $\chi^{(4)}_{I,eff}$. The theory may be in error, however, since theory and experiment differ by a factor of 50 for lithium formate[18] (even after accounting for the inference effects), the only other material for which fourth-order nonlinear processes have been studied.

H. Kildal
G. W. Iseler

D. HIGH-RESOLUTION TUNABLE SUBMILLIMETER SPECTROSCOPY

In a previous Solid State Research Report,[32] the generation and detection of tunable submillimeter radiation using corner-reflector diode mixers was reported. Two source systems were described: one which generated tunable sidebands by mixing a microwave signal with the output of a submillimeter laser, and one which generated a high-order harmonic directly from a microwave signal. The first system has been developed into a tunable sideband spectrometer for linear absorption spectroscopy which has higher sensitivity than the harmonic spectrometer.

Radiation from an optically pumped submillimeter laser is coupled into both the sideband generator and the heterodyne receiver. In the sideband generator, the laser radiation is mixed with a microwave signal of up to 45 GHz in a corner-reflector-mounted Schottky-barrier diode. The antenna structure which couples the laser radiation into the diode reciprocally reradiates the sidebands. A diplexer separates the reradiated sidebands from the fundamental laser radiation. The transmitted intensity of the sidebands is detected with high sensitivity in a heterodyne receiver in which a second diplexer combines the local oscillator and sideband beams with low loss in a corner-reflector-mounted diode mixer. The recovered IF is amplified, filtered, and synchronously detected. The new sideband system, shown in Fig. II-7, is significantly more efficient than the version previously discussed, since about one-half of the laser radiation is coupled into the source diode.

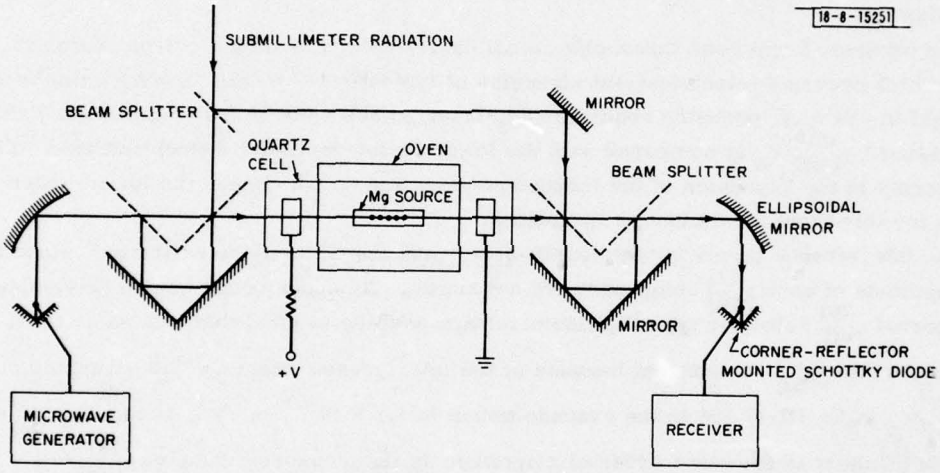


Fig. II-7. Tunable sideband submillimeter spectrometer with high-temperature Mg cell.

Preliminary measurements with the system have included the observation with high resolution of the $4_{13} \rightarrow 4_{22}$ rotational transition in D_2O at 692,245 ± 1 MHz (692,240.5 ± 2.8 MHz predicted[33] from measurements of lower-frequency transitions). Also observed was the $J = 5 \rightarrow 6$ rotational transition in CO at 691,473 ± 1 MHz (in agreement with the measurements of Helminger, De Lucia, and Gordy[34] and predictions of Kildal, Eng, and Ross[35] based upon CO-laser frequency measurements as well as prior data). The intensity of the absorption was two-orders-of-magnitude smaller than that of the D_2O absorption. The local oscillator was the 432.6-μm line of HCOOH, and the observations were made with a S/N of up to 60 dB. The CO measurements were made in support of an astronomical program to detect the $J = 5 \rightarrow 6$ transition in interstellar dust clouds.

The high S/N attainable makes the apparatus attractive for the study of still weaker transition in transient species. One material of particular interest is magnesium in its metastable ^3P state. This requires more sophisticated sample cells, as indicated in Fig. II-7, and a specialized high-temperature cell has been constructed to create and store the metastable Mg. Controlled small quantities of Mg effuse from an externally heated source chamber. The Mg is excited to the ^3P state by either an RF or DC discharge. The quartz windows of the cell are cold and protected from the Mg by a buffer gas. Using the 496-μm line of CH_3F, we have generated a sideband at 601.32 GHz (corresponding to the as yet unobserved $^3P_0 \rightarrow {}^3P_1$ fine-structure transition in Mg) which we have detected with a S/N of over 40 dB.

We are increasing the sensitivity of the spectrometer by amplitude stabilization of the submillimeter laser and by using Zeeman modulation of the Mg cell to make the first direct observation of this transition. This measurement will facilitate the locking of the CH_3F laser to a beam of metastable Mg for use as a possible submillimeter frequency standard.[36]

W. A. M. Blumberg D. D. Peck
H. R. Fetterman P. F. Goldsmith†

REFERENCES

1. S. R. Chinn, H. Y-P. Hong, and J. W. Pierce, Laser Focus 12, 64 (1976).
2. H. P. Weber, Opt. Quantum Electron. 7, 431 (1975).
3. H. G. Danielmeyer, Festkörperprobleme (Adv. in Solid State Physics) XV, 253 (1975).
4. S. R. Chinn and W. K. Zwicker, Appl. Phys. Lett. 31, 178 (1977).
5. M. Saruwatari, K. Otsuka, S. Miyazwa, T. Yamada, and T. Kimura, IEEE J. Quantum Electron. QE-13, 836 (1977).
6. G. Huber and H. G. Danielmeyer, Tenth International Quantum Electronics Conference, Atlanta, Georgia, 1978 (paper C.4).
7. C. A. Burrus, J. Stone, and A. G. Dentai, Electron. Lett. 12, 600 (1976).
8. J. J. Hsieh, J. A. Rossi, and J. P. Donnelly, Appl. Phys. Lett. 28, 709 (1976), DDC AD-A028550/2.
9. W. K. Zwicker, T. Kovats, and S. R. Chinn, Fourth American Conference on Crystal Growth, Gaithersburg, Maryland, 16-20 July 1978 (paper IIIB).
10. A. Lempicki, R. M. Klein, and S. R. Chinn, IEEE J. Quantum Electron. QE-14, 283 (1978).
11. S. Singh, R. G. Smith, and L. G. van Uitert, Phys. Rev. B 10, 2566 (1974).
12. The cross-section value we have used is the population-weighted sum over the overlapping contribution from several $R_i \rightarrow Z_j$ transitions. We have taken the sum of the "a" and "b" cross sections appropriate to emission in the "c" direction, and then used the average value of this sum computed from the differing data of G. Huber, W. W. Krühler, W. Bludau, and H. G. Danielmeyer, J. Appl. Phys. 46, 3580 (1975), and of S. Singh, D. C. Miller, J. R. Potopowicz, and L. K. Shick, J. Appl. Phys. 46, 1191 (1975).

† University of Massachusetts, Amherst.

13. Solid State Research Report, Lincoln Laboratory, M.I.T. (1978:3), p. 7.

14. R. B. Chesler, M. A. Karr, and J. E. Geusic, Proc. IEEE 58, 1899 (1970).

15. R. P. Hilberg and W. R. Hook, Appl. Opt. 9, 1939 (1970).

16. W. D. Fountain, Appl. Opt. 10, 972 (1971).

17. R. F. Begley, R. L. Byer, D. S. Chemla, M. M. Choy, R. L. Herbst, R. S. Feigelson, and S. Ciraci, Technical Report AFML-TR-74-240, Air Force Materials Laboratory, Air Force Systems Command, Wright-Patterson Air Force Base, Ohio (1974).

18. S. A. Akhmanov, in Nonlinear Optics, edited by N. Bloembergen, Proc. International School of Physics "Enrico Fermi," Course LXIV (North-Holland, New York, 1977).

19. M. G. Grozeva, D. I. Metchkov, V. M. Mitev, L. I. Pavlov, and K. V. Stamenov, Opt. Commun. 23, 77 (1977).

20. S. A. Akhmanov, A. N. Dubovik, S. M. Saltiel, I. V. Tomov, and V. G. Tunkin, JETP Lett. 20, 117 (1974).

21. S. A. Akhmanov, V. A. Martynov, S. M. Saltiel, and V. G. Tunkin, JETP Lett. 22, 65 (1975).

22. G. W. Iseler, H. Kildal, and N. Menyuk, in Ternary Compounds 1977, edited by G. D. Holah, Proc. 3rd Intl. Conf. on Ternary Compounds (The Institute of Physics, London, 1977), pp. 73-88, DDC AD-A054566/5.

23. R. L. Byer, H. Kildal, and R. S. Feigelson, Appl. Phys. Lett. 19, 237 (1971).

24. G. D. Boyd, E. Buehler, F. G. Storz, and J. H. Wernick, IEEE J. Quantum Electron. QE-8, 419 (1972).

25. D. S. Chemla, R. F. Begley, and R. L. Byer, IEEE J. Quantum Electron. QE-10, 71 (1974).

26. V. I. Zavelishko, V. A. Martynov, S. M. Saltiel, and V. G. Tunkin, Sov. J. Quantum Electron. 5, 1392 (1976).

27. J. E. Midwinter and J. Warner, Brit. J. Appl. Phys. 16, 1667 (1965).

28. E. Yablonovitch, C. Flytzanis, and N. Bloembergen, Phys. Rev. Lett. 29, 865 (1972).

29. G. W. Iseler, H. Kildal, and N. Menyuk, J. Electron. Mater. 7, 737 (1978).

30. N. Bloembergen, IEEE J. Quantum Electron. QE-10, 375 (1974).

31. B. F. Levine and C. G. Bethea, Appl. Phys. Lett. 20, 272 (1972).

32. Solid State Research Report, Lincoln Laboratory, M.I.T. (1978:2), p. 15, DDC AD-A061241.

33. W. S. Benedict, S. A. Clough, L. Frenkel, and T. E. Sullivan, J. Chem. Phys. 53, 2565 (1970).

34. P. Helminger, F. C. De Lucia, and W. Gordy, Phys. Rev. Lett. 25, 1397 (1970).

35. H. Kildal, R. S. Eng, and A. H. M. Ross, J. Mol. Spectrosc. 53, 479 (1974), DDC AD-A006706/6.

36. F. Strumia, Metrologia 8, 85 (1972).

III. MATERIALS RESEARCH

A. LASER ANNEALING OF Se-IMPLANTED GaAs

Experiments on the laser heating of Si and GaAs have shown that amorphous films of both materials can be crystallized by this technique if the power density is sufficient.[1,2] In addition, it has been found that laser heating of ion-implanted Si can anneal away damage and produce good electrical activation of implanted dopants, in some cases without causing appreciable dopant diffusion.[3] In experiments on laser annealing of ion-implanted GaAs layers, backscattering data have indicated that nearly all the ion-implantation damage could be annealed away and that the dopant species were in substitutional sites.[4] However, little information has been published on the electrical characteristics of such annealed layers.

We have now carried out a study of the effects of annealing with a CW Nd:YAG laser on the electrical properties of Se-implanted GaAs layers. Although good electrical activation has been achieved, we have observed the formation of (111) defect planes which degrade the electrical characteristics.

The samples used in the investigation were either polished slices cut from semi-insulating Cr-doped crystals, or 5- to 10-μm-thick epitaxial layers (S-doped to about 2×10^{15} cm^{-3}) on n^+ substrates. The semi-insulating samples were implanted with 1×10^{14} cm^{-2} 400-keV Se^+ ions. Control samples were implanted with 1×10^{14} cm^{-2} 400-keV Kr^+ ions. The epitaxial samples were implanted with 5×10^{12} cm^{-2} 400-keV Se^+ ions. Implant temperatures were 25°, 250°, and 300°C. Some of the samples were encapsulated either with 500 to 1000 Å of pyrolytic Si_3N_4 deposited prior to implantation, or with SiO_2 or phosphosilicate glass (PSG) deposited after implantation.

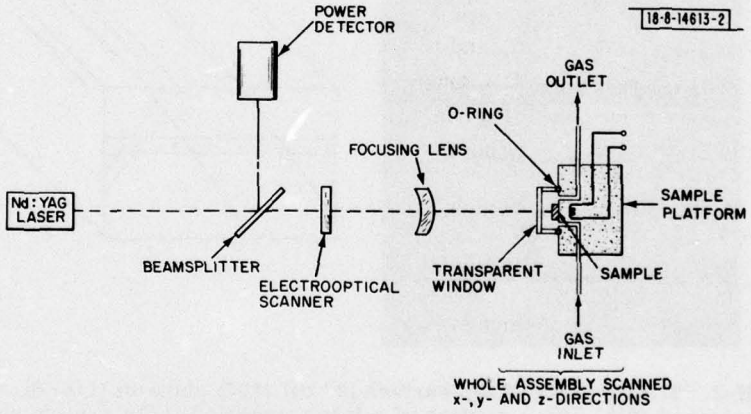


Fig. III-1. Schematic representation of CW Nd:YAG laser annealing system.

The laser annealing system is shown schematically in Fig. III-1. The multimode output of the CW Nd:YAG laser (operating at 1.06 μm) is focused by the cylindrical lens onto the sample. During annealing, the sample is held in a forming gas (Ar/H_2) ambient on a platform that can be resistively heated to over 700°C. The platform temperature generally used was 580°C. This temperature is high enough for sufficient bandgap narrowing to allow efficient absorption

of the Nd:YAG 1.06-μm radiation, but still low enough so that no thermal dissociation is observed. The platform is mounted on an x,y,z translational stage that permits the sample to be scanned under the laser beam in the focal plane and normal to the long axis of the slit image. By using synchronous motors, scan rates from 0.05 to 19 mm/sec have been obtained.

Over a hundred implanted GaAs samples have been laser-annealed under various conditions. The appearance of the sample surface after annealing was found to depend on the laser scan rate and power density P_D. For each scan rate, the surface appearance changed in the same general manner with increasing P_D. At sufficiently low values of P_D the entire surface remained as smooth as before annealing, while at sufficiently high values unencapsulated surfaces showed the characteristic features produced by thermal etching due to the loss of As by vaporization. The threshold P_D for thermal etching increased with increasing scan rate, from less than 4×10^3 W/cm^2 for 0.53 mm/sec to more than 7×10^3 W/cm^2 for 19 mm/sec. For each scan rate, over an intermediate range of P_D values, annealing resulted in the formation of characteristically oriented straight lines on the otherwise smooth surface. Such features have not been previously reported for laser-annealed samples of either GaAs or Si. The values of P_D at which these lines were first observed increased with increasing scan rate, and above this threshold the density of lines increased with increasing P_D. The highest densities of lines were observed for samples annealed at the highest scan rates. Encapsulated samples generally exhibited higher densities of lines than unencapsulated samples annealed under the same conditions, especially at high scan rates.

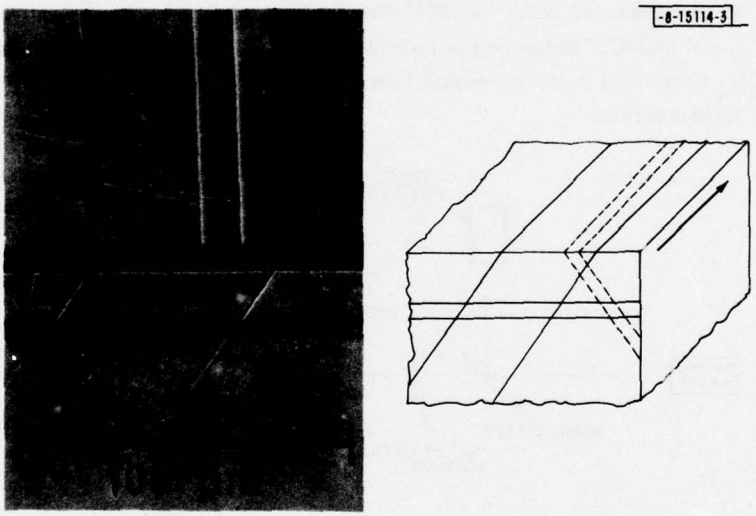


Fig. III-2. Micrographs of top surface [2° off (100) plane in (110) direction] and a cleaved (011) cross section of a laser-annealed GaAs sample showing lines due to defects produced by annealing. Schematic diagram locates lines three-dimensionally on sample. Dark arrow in diagram indicates laser scan direction. Defects have tentatively been identified as (111) slip planes.

The characteristics of the surface lines are illustrated by Fig. III-2, which shows two optical micrographs of an epitaxial sample annealed at the highest scan rate (19 mm/sec) using $P_D = 7.3 \times 10^3$ W/cm^2. The upper micrograph shows the top surface of the sample, which was oriented 2° off the (100) plane, while the lower one shows an (011) plane cleaved perpendicular to

the top surface and stained with a potassium ferricyanide solution. The two micrographs have been positioned to align the corresponding features on the top surface and cleaved cross section. Figure III-2 also includes a schematic diagram locating these features three-dimensionally with respect to the sample, which was formed by the epitaxial growth of an n^+ buffer layer and an upper n-layer on an n^+ GaAs substrate.

The upper micrograph of Fig. III-2 shows two pairs of parallel straight lines ("tracks") on the top surface of the sample – one pair at an angle of 1° to the cleaved edge at the intersection between the (100) and (011) planes, the other pair also at a 1° angle to this edge but in the opposite sense. The angle of 2° between the two pairs of tracks results from the 2° deviation of the top surface from (100) toward (110). As can be seen in the micrograph of the (011) cleaved face, the tracks propagate from the surface through both epitaxial layers into the substrate. On the basis of their orientation, we have tentatively identified the surface tracks as intersections between the (100) surface and two sets of (111) slip planes, which intersect with each other at 70° in the plane of the cleaved (011) face. Since the slip planes propagate from the surface at an angle of 55°, their density is always highest at the surface. Except for the tracks, the top surface is as smooth as it was before annealing, and the interface between the upper epitaxial layer and the buffer layer is also unchanged, indicating that no melting occurred.

Formation of the slip planes is presumably caused by thermal stress that occurs during laser annealing. This mechanism is consistent with the observation that the threshold P_D for producing the surface lines increased with increasing laser scan rate, since the P_D required to achieve a given surface temperature also increases with scan rate.

The presence of slip planes has a strong adverse effect on the electrical properties of laser-annealed GaAs. This effect can be seen from the data listed in Table III-1, which gives the effective sheet carrier concentration N_S and effective mobility μ_s for representative samples prepared by implantation of 1×10^{14} cm^{-2} Se^+ ions directly into semi-insulating substrates and then annealed under various conditions. Significant trends are illustrated by Fig. III-3, in which N_s is plotted against P_D for a number of unencapsulated samples that were Se-implanted at 300°C, then subjected to single laser scans at four different scan rates. The values of N_s and μ_s for control samples that were Se-implanted at 300°C and then heated to 580°C but not laser annealed were 9×10^{11} cm^{-2} and 980 cm^2/V-sec, respectively. For such control samples implanted at room temperature, the resistivity was too high to permit Hall measurements. All the Kr^+-implanted control samples remained semi-insulating following laser annealing.

The data of Fig. III-3, which are restricted to samples that did not have significant thermal etching, show an overall decrease in N_s with increasing scan rate. At the highest scan rate, over the range of P_D values we examined, N_s actually decreases with increasing P_D. On the other hand, at the lower scan rates N_s increases with increasing P_D. These results may be explained by assuming that laser annealing can have two opposing effects: removing ion-implantation damage and producing slip planes. Therefore, it can increase N_s by removing the compensating defects due to implantation damage, but it can also decrease N_s by introducing compensating defects due to slip planes. For the two lower scan rates shown in Fig. III-3, N_s increases with increasing P_D because the increased removal of implantation damage outweighs the rather limited formation of slip planes in these samples. The sample annealed at 0.53 mm/sec with $P_D = 3.0 \times 10^3$ W/cm^2 has the highest N_S that we have obtained for a singly scanned sample, $N_s = 2.7 \times 10^{13}$ cm^{-2} with $\mu_s = 2100$ cm^2/V-sec. By comparison, similarly

TABLE III-1

LASER ANNEALING RESULTS IN GaAs SAMPLES IMPLANTED WITH 1×10^{14} cm^{-2} Se^{+} IONS

Implant Temperature (°C)	Power Density P_D (W/cm^2)	Scan Rate (mm/sec)	No. of Scans	Effective Sheet Electron Concentration N_s (cm^{-2})	Effective Mobility μ_s (cm^2/V-sec)	Surface Features
300	2.1×10^3	0.053	1	1.9×10^{13}	2400	Slight marks
300	2.4×10^3	0.053	1	1.9×10^{13}	2500	Slight marks
300	2.6×10^3	0.53	1	1.7×10^{13}	2100	Slight marks
300	3.0×10^3	0.53	1	2.7×10^{13}	2100	Slight marks
300 (Si_3N_4)	3.0×10^3	0.53	1	2.2×10^{13}	1600	Slight marks
300	3.7×10^3	4.8	1	7.7×10^{12}	1100	Marks
300	3.9×10^3	4.8	1	2.0×10^{13}	1900	Marks
300	4.3×10^3	4.8	1	2.2×10^{13}	1900	Marks
300	3.9×10^3	9.5	1	1.7×10^{13}	1700	Marks
300	4.3×10^3	9.5	1	1.6×10^{13}	1900	Marks
300	4.7×10^3	9.5	1	1.8×10^{13}	1800	Marks
300 (Si_3N_4)	4.3×10^3	9.5	1	1.5×10^{13}	160	Marks
300	5.0×10^3	19.0	1	5.2×10^{12}	1500	Smooth
300	5.6×10^3	19.0	1	5.2×10^{12}	1400	Smooth
300	6.0×10^3	19.0	1	4.3×10^{12}	1000	Slight marks
250	3.0×10^3	0.53	10	5.9×10^{13}	1400	Marks
20	3.0×10^3	0.53	10	3.8×10^{12}	1500	Marks
20	$3.5 \times 10^{3\dagger}$	0.53	10	2.2×10^{13}	2200	Marks

† The uncertainty of the power density incident on this sample is higher.

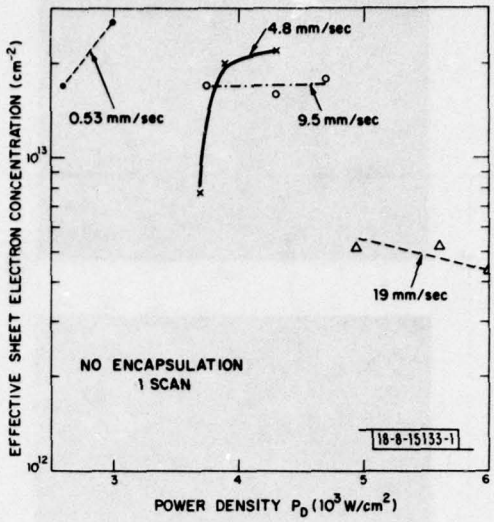


Fig. III-3. Effective sheet carrier concentration vs laser power density at scan rates from 0.53 to 19 mm/sec for GaAs samples implanted with 1×10^{14} cm^{-2} 400-keV Se^{+} ions (implant temperature 300°C).

implanted samples that are thermally annealed at 900°C for 15 min. with a pyrolytic Si_3N_4 encapsulant typically have $N_s = 5.0 \times 10^{13}$ cm^{-2} and $\mu_s = 2300$ cm^2/V-sec. Further improvement can be expected at 0.53 mm/sec by increasing P_D, provided that the threshold for thermal etching is not significantly exceeded.

For the samples of Fig. III-3 that were annealed at a scan rate of 9.5 mm/sec, all of which exhibited significant densities of surface lines, N_s was essentially independent of P_D over the range used, indicating that the two opposing effects of laser heating canceled each other. Of the samples annealed at 19 mm/sec, the two annealed at the lower values of P_D did not exhibit surface lines but both had the same low value of N_s. Probably the surface temperatures achieved at those power levels were not sufficient to remove very much of the implantation damage. For the third sample, which was annealed at 6×10^3 W/cm^2, not many surface lines were observed, but these apparently outweighed any increased removal of implantation damage. The use of still higher power levels resulted in a rapid increase in the density of the surface lines, and the results of van der Pauw measurements became too anisotropic to be meaningful.

The anisotropy in the van der Pauw results is another consequence of the formation of slip planes. This is demonstrated by the results shown in Fig. III-4, which includes two I-V curves obtained for different electrode pairs in measurements on a cloverleaf mesa etched on the surface of a sample that had been laser-annealed under conditions that produced a high density of slip planes. The schematic diagram of the cloverleaf in Fig. III-4 shows the configuration of the surface lines in relation to the electrodes (only three of the lines are indicated). The I-V curve designated as (a), which was obtained for electrodes 1 and 2 or 3 and 4, is linear and indicates low resistivity. Curve (b), for electrodes 1 and 4 or 2 and 3, is characteristic of back-to-back diodes. In the first case, the current paths between the electrodes do not intersect the slip planes, while in the second case they do. The characteristics of curve (a) thus show that the laser annealing removed the ion implantation damage in the regions between the planes, while those of curve (b) show that the planes act as barriers in n-type GaAs.

The effects of the slip planes on the electrical properties of laser-annealed samples are further shown by C-V carrier-concentration profiles on several ion-implanted GaAs epitaxial

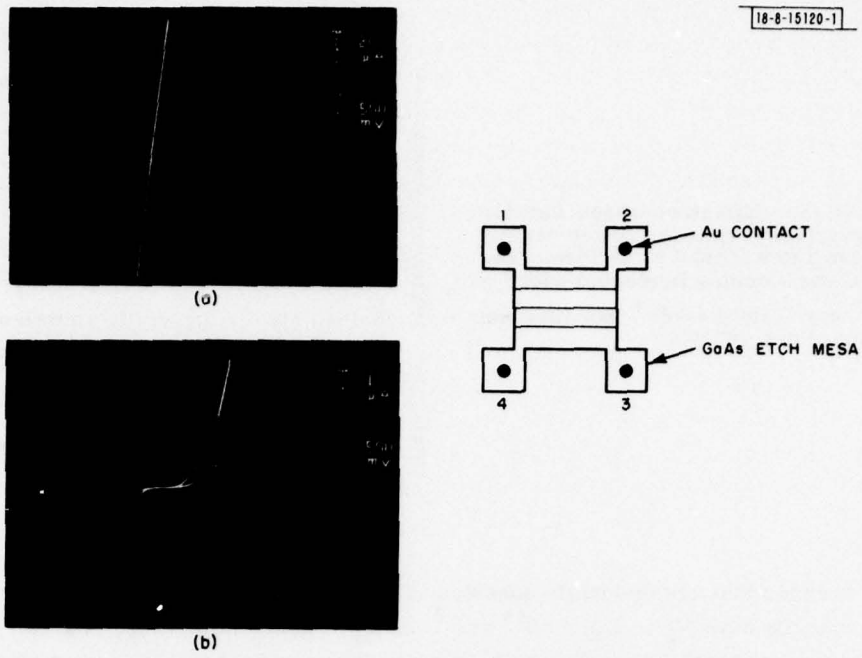


Fig. III-4. Current-voltage characteristics between different contacts to an etched mesa cloverleaf on laser-annealed GaAs with a high density of defect lines. Insert schematically shows etched cloverleaf with three such lines. (a) I-V characteristics parallel to these lines, i.e., between contacts 1 and 2 or 3 and 4; (b) across the lines, i.e., between contacts 1 and 4 or 2 and 3.

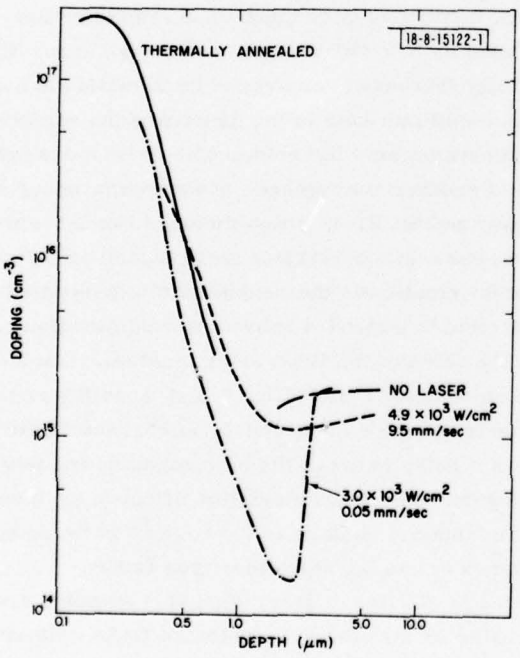


Fig. III-5. Effective carrier concentration vs depth obtained from C-V measurements on GaAs samples implanted with 5×10^{12} cm^{-2} 400-keV Se^+ ions (implant temperature 300°C). Solid line represents data for an encapsulated sample that was thermally annealed at 900°C for 15 min. Other three samples were mounted on substrate platform which was heated to 580°C.

layers. These layers had an initial carrier concentration of 2×10^{15} cm^{-3} and were implanted with 5×10^{12} cm^{-2} Se^+ ions at 300°C. Figure III-5 shows the effective carrier-concentration (n_{eff}) profiles for four such samples. The solid line represents data obtained for a sample that was encapsulated with Si_3N_4 and thermally annealed at 900°C for 15 min. The other three samples were not encapsulated. In separate experiments using the laser-annealing system, each was mounted on the sample platform which was heated to 580°C. The sample not subjected to laser heating exhibited no activation. For the sample subjected to a single laser scan at 9.5 mm/sec with $P_D = 4.9 \times 10^3$ W/cm^2, slip planes were observed but activation occurred. However, the peak n_{eff} was much lower than that obtained for the thermally annealed sample. In addition, n_{eff} in the unimplanted region of the epitaxial layer decreased from its original level of about 2×10^{15} cm^{-3} to about 10^{15} cm^{-3}, presumably because the slip planes propagated into this region. For the sample annealed at 0.05 mm/sec with $P_D = 3 \times 10^3$ W/cm^2, the peak n_{eff} was higher than in the other laser-annealed sample, but still lower than the value obtained by thermal annealing. In this sample, the slip planes probably account for the deep minimum in n_{eff}, but they apparently propagated to a depth of only about 4 μm, since n_{eff} returned to its initial value at about this depth.

Reflection high-energy-electron diffraction (RHEED) indicates that the surfaces of samples implanted at 250° or 300°C are single crystal both before and after laser annealing. Samples implanted at room temperature were found to be amorphous prior to annealing, and single crystal afterwards. It was further noted that these RHEED observations show good single crystallinity even when a large number of slip planes are present. This result indicates that in order to characterize laser-annealed samples, crystallographic-type observations should be supplemented by electrical measurements.

In summary, one laser scan is sufficient to obtain fairly good activation of GaAs samples implanted at 250° or 300°C. The best results obtained were for low scan rates. At 0.53 mm/sec, the best results for a single scan were $N_s = 2.7 \times 10^{13}$ cm^{-2} and $\mu_s = 2100$ $cm^2/V\text{-sec}$. On samples scanned ten times at 0.53 mm/sec, the best measured N_s was 5.9×10^{13} cm^{-2}. The corresponding sheet mobility was only 1300 $cm^2/V\text{-sec}$, however, and is most likely limited by slip-plane formation. For fast scan rates, multiple scans usually caused more defect planes, and Hall measurements became quite anisotropic.

On samples implanted at room temperature, one scan did not generally result in appreciable activation, but ten scans did. The best results obtained for a sample implanted at room temperature and scanned ten times at 0.53 mm/sec were $N_s = 2.2 \times 10^{13}$ cm^{-2} and $\mu_s = 2200$ $cm^2/V\text{-sec}$.

Overall, the results suggest that very good electrical characteristics may be possible if the formation of slip planes can be prevented or minimized. Since these planes are probably caused by thermal stress encountered in laser heating, annealing procedures such as lower scan rates and/or higher substrate platform temperatures, which reduce thermal stress, should lead to some improvement. It may also be possible that slip-plane formation can be reduced if surface orientations other than (100) are used. There is probably no obvious advantage to using pulsed-laser heating, since large thermal stresses are incurred in this mode of operation.

J. C. C. Fan C. O. Bozler
J. P. Donnelly R. L. Chapman

B. ACTIVATION ENERGY OF Cr ACCEPTORS IN InP

Infrared diode lasers and avalanche photodiodes utilizing GaInAsP epitaxial layers grown on InP substrate are promising sources and detectors for fiber optics communications at 1.1 to

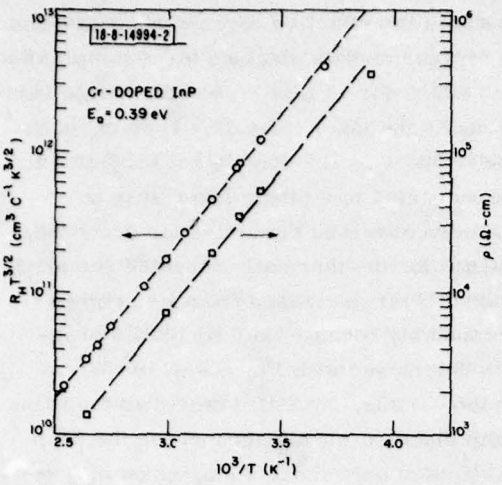


Fig. III-6. Dependence of $R_H T^{3/2}$ (left ordinate) and resistivity ρ (right ordinate) on reciprocal absolute temperature 1/T for an InP sample from a Cr-doped LEC boule.

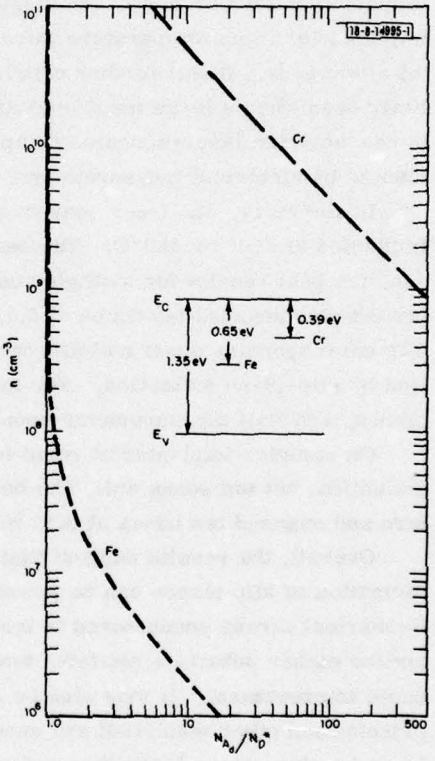


Fig. III-7. Calculated dependence of carrier concentration in InP at 295 K, n_{295}, on N_{A_d}/N_D^*, the ratio of deep acceptor (Fe or Cr) concentration to difference between total donor concentration and concentration of acceptors other than Fe or Cr.

1.3 μm. As previously reported,[5] we have been growing InP single crystals by the liquid-encapsulated Czochralski (LEC) method to provide substrate material for use in the development of these devices. Semi-insulating crystals with resistivities of $\sim 10^8$ Ω-cm have been obtained by doping with Fe, a deep acceptor. By measuring the Hall coefficient (R_H) as a function of temperature for a sample from one of these crystals, the activation energy for thermally exciting electrons from the Fe acceptor level to the conduction band was found to be 0.65 eV (see Ref. 5).

Like Fe, Cr is known to be a deep acceptor in InP, since resistivities of 10^3 to 10^5 Ω-cm have been obtained by Cr doping of material that would otherwise be n-type with low resistivity.[6] However, these values are much lower than those achieved by Fe doping. In order to establish the reason for this difference, we have determined the activation energy for electron excitation from the Cr acceptor level. As in the case of Fe, this determination was made by measuring R_H as a function of temperature. The measurements were made on a Cr-doped sample, cut from a crystal grown by the LEC method, with room-temperature resistivity (ρ) of 5.3×10^4 Ω-cm, carrier concentration ($n = 1/R_H e$) of 2.6×10^{10} cm^{-3}, and Hall mobility ($\mu = R_H/\rho$) of 4600 cm^2/V-sec. The results are shown in Fig. III-6, where $R_H T^{3/2}$ and ρ are plotted on logarithmic scales vs 1/T. The activation energy obtained from the $R_H T^{3/2}$ plot is 0.39 ± 0.01 eV, in good agreement with the value of 0.37 eV obtained by Pande and Roberts[7] as the thermal activation energy for the flow of current through a Cr-doped sample in the ohmic current range. For the space-charge-limited range, these authors found an activation energy of 0.20 eV. They explained their observations in terms of a deep donor, deep acceptor model with a total deep acceptor concentration of $<10^{12}$ cm^{-3}. This model is inconsistent with our results, since it implies a residual net donor concentration that is also $<10^{12}$ cm^{-3}, while we have never observed values of n_{300} below about 5×10^{14} cm^{-3} for nominally undoped samples of InP.

The molar Cr concentration in the charge used for our Cr-doped boule was 4500 ppm. Assuming that Cr is a simple deep acceptor with an activation energy of 0.39 eV and that the residual donor concentration is 3×10^{15} cm^{-3}, from the measured value of n_{300} for a first-to-freeze sample we have calculated the concentration of Cr incorporated in the sample to be 2.7 ppm, corresponding to a distribution coefficient of 6×10^{-4}. This value falls within the range of 1 to 6×10^{-4} found by means of mass spectrographic analysis.[8]

For wide-bandgap semiconductors containing excess residual donors (i.e., $N_D^* > 0$, where N_D^* is the difference between the total donor concentration and the concentration of shallow acceptors), very high resistivities can be obtained by incorporating acceptor impurities with levels located near the center of the bandgap because the Fermi level is shifted from the vicinity of the conduction band to the vicinity of the deep levels, greatly reducing the carrier concentration. The shift of the Fermi level increases with increasing separation between the deep levels and the conduction band E_c, and also as the ratio of the deep acceptor concentration N_{A_d} to N_D^* increases. For InP doped with Fe or Cr, these trends are shown in Fig. III-7 where calculated values of n at 295 K are plotted against N_{A_d}/N_D^*. For doping with Fe (acceptor level 0.65 eV below E_c), n decreases precipitously as soon as the Fe concentration exceeds N_D^*, reaching values of 10^8 and 10^7 cm^{-3} for N_{A_d}/N_D^* ratios of 1.2 and 2.6, respectively. In contrast, for doping with Cr (acceptor level 0.39 eV below E_c), n does not reach 10^{10} cm^{-3} until $N_{A_d}/N_D^* = 50$, and is still 9×10^8 cm^{-3} even for $N_{A_d}/N_D^* = 500$. Thus, the highest resistivities obtained for Cr-doped InP are much lower than those achieved by Fe doping because the Cr acceptor level

is considerably closer to the conduction band than is the Fe level, not because Cr is less soluble in InP than Fe. Even if the solubility of Cr were the same as that of Fe, which is reported to be 2.5×10^{17} cm^{-3} (Ref. 9), and N_D^* were only 1×10^{15} cm^{-3}, n would still be $\sim 2 \times 10^9$ cm^{-3} at the Cr solubility limit, compared with the values of $\sim 10^7$ cm^{-3} we have obtained for Fe-doped samples.

G. W. Iseler

REFERENCES

1. J. C. C. Fan and H. J. Zeiger, Appl. Phys. Lett. 27, 224 (1975), DDC AD-A016696/7.
2. J. C. C. Fan, H. J. Zeiger, and P. M. Zavracky, Proc. National Workshop on Low Cost Polycrystalline Silicon Solar Cells, Dallas, Texas, 18-19 May 1976, pp. 89-104.
3. A. Gat, J. F. Gibbons, T. J. Magee, J. Peng, V. R. Deline, P. Williams, and C. A. Evans, Jr., Appl. Phys. Lett. 32, 276 (1978).
4. J. A. Golovchenko and T. N. C. Venkatesan, Appl. Phys. Lett. 32, 147 (1978).
5. Solid State Research Report, Lincoln Laboratory, M.I.T. (1978:2), p. 21, DDC AD-A061241.
6. G. A. Antypas, in Gallium Arsenide and Related Compounds (St. Louis) 1976, edited by L. F. Eastman (The Institute of Physics, London, 1977), p. 55.
7. K. P. Pande and G. G. Roberts, J. Phys. C 9, 2899 (1976).
8. B. W. Straughan, D. J. Hurle, K. Loyd, and J. B. Mullin, J. Cryst. Growth 21, 117 (1974).
9. R. N. Lee, M. K. Norr, R. L. Henry, and E. M. Swiggard, Mater. Res. Bull. 12, 651 (1977).

IV. MICROELECTRONICS

A. INTEGRATED MIXER MODULE FOR SUBMILLIMETER-WAVELENGTH OPERATION

A GaAs monolithic integrated circuit capable of receiving radiatively coupled submillimeter-wavelength radiation has been fabricated. Figure IV-1 is a schematic of the circuit elements which have been integrated on this module. The radiation is received by a slot antenna and coupled to a surface-oriented mixer diode[1] by an appropriate section of coplanar transmission line. An integrated bypass capacitor completes the mixer circuit by providing a low impedance to radio frequencies and a high impedance to intermediate frequencies. The realization of the circuit of Fig. IV-1 is shown in Fig. IV-2(a). The design of the planar slot antenna is complicated by the presence of the high-resistivity GaAs. Free-space radiation patterns, even from a simple metal antenna fabricated on the high-resistivity GaAs, show complex lobe structure unacceptable for most applications. Therefore, the module of Fig. IV-2(a) has been designed so that the radiation is coupled through the high-resistivity GaAs substrate. The radiation pattern obtained at 350 GHz is shown in Fig. IV-2(b). It is nearly identical to that obtained from a frequency-scaled model at 5 GHz. The pattern was obtained in both cases by measuring the video response of the surface-oriented diode as the direction of the incident radiation was changed. The theoretically expected radiation pattern from a half-wavelength dipole is also shown in Fig. IV-2(b) for comparison.

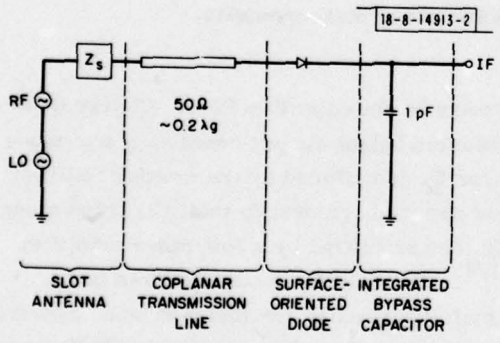


Fig. IV-1. Circuit diagram of integrated mixer module designed for quasi-optical operation at 350 GHz.

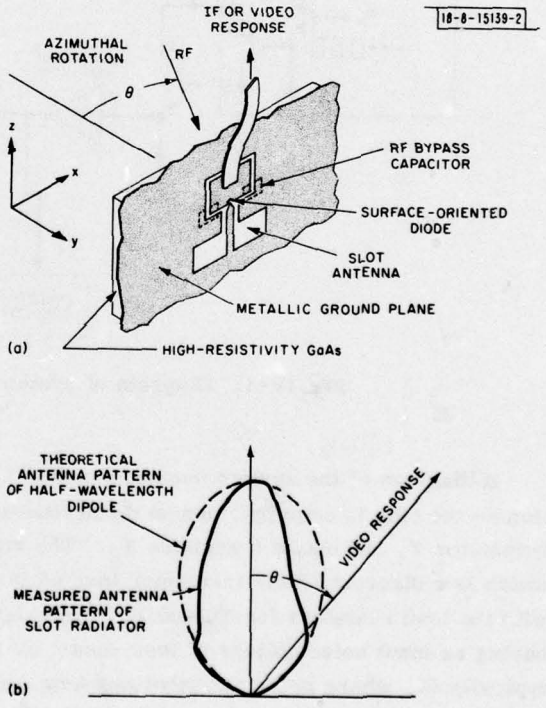


Fig. IV-2. Millimeter-wave mixer module. (a) Configuration of device and circuit elements on module. Radiation is coupled through GaAs as shown. (b) Radiation patterns at 350 GHz.

Though the measured radiation pattern does contain some interference from the coplanar transmission-line feed, it allows the near-millimeter-wavelength radiation to be radiatively coupled to the device. The conversion loss measured at 350 GHz with this mixer was approximately 20 dB, as compared with a 7.5-dB loss obtained with the frequency-scaled model. Network-analyzer measurements have indicated that the comparatively poor performance of the mixer module at 350 GHz is due to loss in the RF bypass capacitors. A mixer module which incorporates improved bypass capacitors is currently being fabricated.

R.A. Murphy
G.D. Alley
B.J. Clifton

B. CHARGE-COUPLED DEVICES: IMAGERS

The 100- × 400-element CCD imagers fabricated for the GEODSS (Ground Electro-Optical Deep Space Surveillance) program are required to have as high a sensitivity as possible. This implies both high quantum efficiency and low-noise charge transfer and charge detection. In this report, we describe some experimental results on noise measurements related to charge detection and signal processing. Using correlated double sampling (CDS), we have achieved noise-equivalent signals from the detection circuitry of 10 electrons at a 400-kHz data rate.

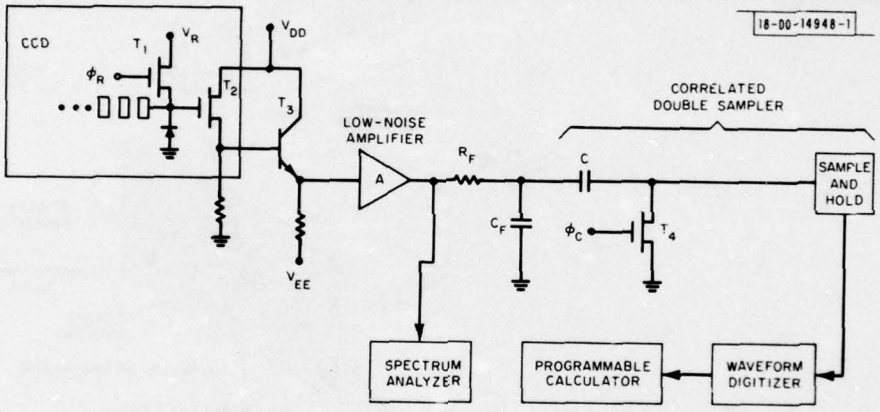


Fig. IV-3. Diagram of system used in noise measurements.

A diagram of the system used to evaluate CCD noise is shown in Fig. IV-3. Charge detection on the chip is done by a conventional floating-diffusion output circuit consisting of a reset transistor T_1 and output transistor T_2. The signal for T_2 is buffered by the emitter follower T_3, which is a discrete 2N930 transistor located in the device package next to the CCD chip[2] along with the load resistors for T_2 and T_3. The signal is then amplified by a low-noise amplifier having an input noise voltage of less than 2 nV $Hz^{-1/2}$. The gain A is adjusted to a level, typically 50, where noise contributions from the remaining circuits are insignificant. Spectral measurements of the noise from T_2 and T_3 are made at this point. The signal-processing chain continues with a low-pass filter formed by R_F and C_F to band-limit the noise, followed by a

circuit which performs correlated double sampling.[3-5] The mean and variance of the sampled voltage signal are measured by first digitizing a sequence of signal samples (typically 1024) to 10-bit resolution in a waveform digitizer† and transmitting the data to a programmable calculator‡ for computation. The calculator can plot on a display scope the distribution function of the voltage samples together with a comparison plot of a Gaussian curve of the same mean and standard deviation to verify the Gaussian nature of the noise.

The noise-equivalent signal in electrons is then determined by the rms noise voltage after signal processing divided by the voltage/electron conversion ratio. The term usually applied to this ratio is responsivity R expressed in volts/electron, and is given by

$$R = G \frac{g}{C_o} \qquad \text{(IV-1)}$$

where G is the voltage gain between the gate of T_2 and the point in the circuit where the signal is measured, and C_o is the capacitance at the output-diode node. Low-noise operation then dictates low C_o and low noise from T_2. By careful design of the output circuit, the capacitance C_o has averaged 0.050 pF or a factor-of-4 lower than values typical of CCDs described in the literature. Corresponding responsivities measured at the emitter of T_3, where G = 0.75, have been in the range of 2.3 to 2.5 μV/electron.

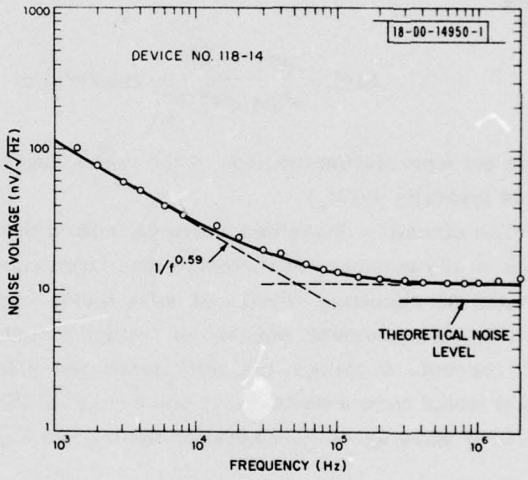


Fig. IV-4. Measurement of noise spectral voltage of output MOSFET and emitter follower. MOSFET is operating in buried-channel mode.

Under ideal circumstances, the off-chip signal processing should result in noise levels determined solely by the thermal noise of T_2. It has been shown by Brodersen and Emmons[4,5] that the noise of T_2 can be significantly reduced if this transistor is subjected to the same buried-channel implant as the remainder of the device, and if it is operated in a buried-channel mode (i.e., the channel current flow is kept away from the oxide-silicon interface). The normally high 1/f noise is significantly reduced in this case. In our process, T_2 receives the buried-channel implant, and we have observed greatly reduced noise output when operating T_2 buried channel. A typical measurement of noise spectral voltage for the T_2-T_3 combination is shown in Fig. IV-4,

† Biomation Model 1010.

‡ Hewlett-Packard Model 9825A.

and it is seen that significant 1/f noise still occurs at frequencies below 50 kHz. The measured slope of the low-frequency noise voltage exhibits a $1/f^{0.59}$ dependence for this device, in contrast to the usual $1/f^{1/2}$ relationship. The high-frequency noise level of 12 $nV/\sqrt{Hz}$ is somewhat higher than the theoretical value of 8.6 $nV/\sqrt{Hz}$.

The signal processing performed by the low-pass filter and correlated double sampling is needed to fully realize the low-noise capability of this system. The low-pass filter removes high-frequency noise which would be aliased into the sampled data passband below $f_c/2$, where f_c is the clock frequency. The optimum corner frequency f_L of this filter has been shown to be[4,5]

$$f_L = 4f_c/3 \quad . \tag{IV-2}$$

The video clamping performed by coupling capacitor C and switch T_4 in Fig. IV-3 removes reset noise from the signal when the reset gate of the CCD is being clocked, and, in addition, helps suppress low-frequency noise such as 1/f noise. Reset noise is given by $(kTC_o)^{1/2}/q$, and would be 90 electrons in our case. The mean-square output-noise voltage $\overline{V}_o^2$ from the low-pass filter/CDS processor in terms of the input-noise spectral voltage $\overline{V}_i^2$ is[5]

$$\overline{V}_o^2 = 2\,[R(\tau) - R(o)]$$

where

$$R(\tau) = \int_o^\infty \frac{\overline{V}_i^2}{1 + f^2/f_L^2} (\cos 2\pi f\tau)\, df \tag{IV-3}$$

is the autocorrelation function of the noise, and τ is the time between clamp and sample pulses and is typically $1/(2f_c)$.

The circuitry described above permitted the observation of very low noise levels. As a check on the accuracy of the noise measurements, the CCD was illuminated with an incandescent bulb and the resulting signal and noise levels were measured at the output of the CDS circuit. For this measurement, only the 405-stage output register of the imager was clocked to minimize dark current. In theory, optically generated charge packets having an average of $\bar{n}$ electrons/packet would have a photon shot noise level of $(\bar{n})^{1/2}$ electrons. The experimental results in Fig. IV-5 show agreement between theory and experiment to within 5 percent.

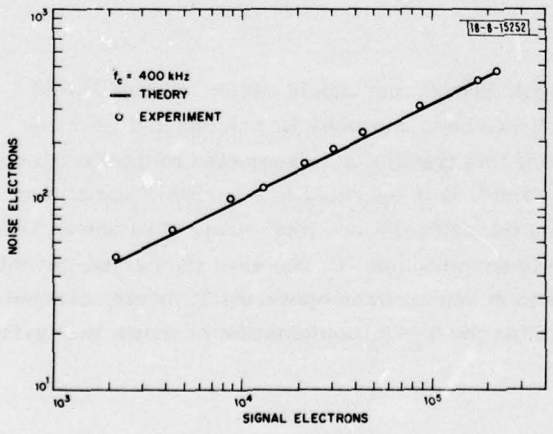


Fig. IV-5. Measured noise level on optically generated signal. Theoretical photon shot noise level in electrons is equal to square root of average signal level and is shown as solid line.

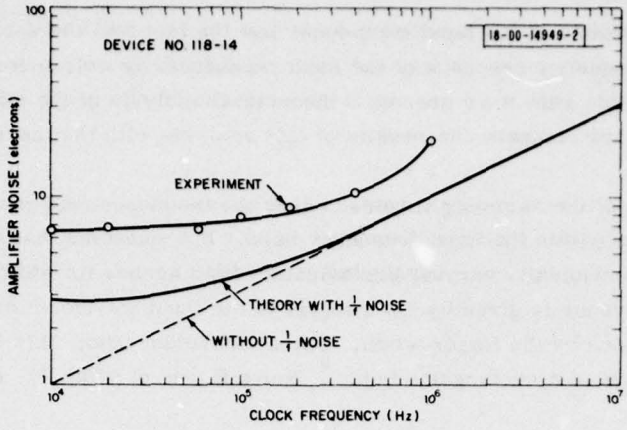


Fig.IV-6. Measured amplifier noise from CCD with no signal charge. Theoretical curve is based on measured spectral noise in Fig.IV-4 and includes a calculation assuming the data in Fig.IV-4 had no 1/f component.

Measurements were made of the system noise with the CCD clocked in the normal fashion, but with the output gate biased off. In this case, dark-current charge is prevented from being delivered to the CCD output circuit, and the system noise should be only that of the output circuit. Measurements made at clock frequencies from 10 kHz to 1 MHz are shown in Fig.IV-6. At each frequency, the low-pass filter was adjusted according to Eq.(IV-2). The values range from about 7 electrons at 10 kHz to 20 electrons at 1 MHz, and represent the lowest reported noise-equivalent signals from a floating diffusion output structure. Plotted in the same figure is a theoretical curve using Eq.(IV-3) and the measured noise data from Fig.IV-4. In addition, the calculation was also performed (dashed curve) assuming the measured noise data had only the high-frequency white noise and no 1/f component. This curve suggests that noise levels below one electron may be possible at low clock frequencies with carefully made low-noise output MOSFETs. The measured data are about a factor-of-2 higher than theory. The major difference in the measurement conditions of Figs.IV-4 and IV-6 is that in the former the CCD output is DC-biased to its operating point with all clocks off, while in the latter the CCD is clocked. Earlier measurements of noise were much higher, and the problem was traced to a commercial pulse generator used for the reset gate which had fairly high levels of noise (several thousand $nV/\sqrt{Hz}$). Generators having much lower noise levels were then used, and much lower CCD noise levels were achieved. The remaining discrepancy between theory and experiment may still be due to pulse-generator noise.

B.E. Burke
W.H. McGonagle

C. CHARGE-COUPLED DEVICES: SAW/CCD BUFFER MEMORY

The SAW/CCD buffer memory is described in detail in earlier reports.[6,7] The device is comprised of a set of sampling fingers on a CCD die which is in close proximity (typically 300 nm) to a SAW delay line. The piezoelectric RF fields associated with a traveling surface wave are sampled and held by the fingers, and the resulting charge pattern is parallel-transferred to a CCD shift register. The overall frequency response of the SAW/CCD buffer memory is affected

by the frequency response of the input transducer and the fact that the sampling fingers have finite width. The frequency response of the input transducer is well understood[8] and will not be discussed here. In this report we present a theoretical analysis of the effect of finger width on frequency response and compare the results of this analysis with the measured response of the prototype device.

The finite width of the sampling fingers causes the frequency response to roll off gradually at higher frequencies within the input frequency band. If we assume that each finger samples the average of the sinusoidally varying piezoelectric field across its width, then this component of the frequency response is given by the integral of the input waveform over the width of the sampling finger divided by the finger width. For a sinusoidal input, this integral is identical to the Fourier transform of a rectangular pulse.[9] For a finger of width W, the transfer function is given by

$$\text{T.F.} = \frac{\sin(\pi W/\lambda)}{\pi W/\lambda} \qquad \text{(IV-4)}$$

Here, λ is the wavelength (or the inverse of the spatial frequency) of the piezoelectric field and is equal to V_a/f, where V_a is the velocity of the surface acoustic wave and f is the input radio frequency. This transfer function is more useful if it is expressed in terms of f, f_s, and S_c:

$$\text{T.F.} = \frac{\sin \pi(W/S_c)\,(f/f_s)}{\pi(W/S_c)\,(f/f_s)} \qquad \text{(IV-5)}$$

where S_c is the spatial period of the sampling fingers, and $f_s = V_a/S_c$ is an effective sampling frequency discussed in an earlier report.[6] A computer program has been written which calculates the theoretical frequency response of the SAW/CCD buffer memory by combining the above equation with the theoretical response of the input transducer and its matching network.

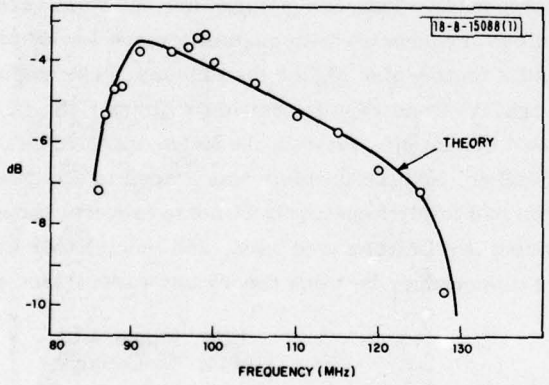


Fig. IV-7. Frequency response of buffer memory.

The frequency response of the first prototype device is shown in Fig. IV-7. The measured response falls off inside the pass band of the input transducer as predicted by theory. (The artifact in the experimental data around 98 MHz is the result of measurement errors, which can be as high as 1 dB.) The theoretical curve in the figure is calculated for W = 18 μm, which is equal to the measured finger width of 16 μm plus the 2 μm which the wave travels in the 0.6 nsec it takes to close the sampling gate. In a system application, this rolloff can be eliminated by

tailoring the response of the input transducer and its matching network to flatten the overall response.

D. L. Smythe
B. E. Burke

D. PARALLEL-PLATE PLASMA ETCHING FOR SILICON CCDs

Plasma etching of deposited thin films of Si_3N_4 and polycrystalline silicon has been incorporated into the fabrication sequence for CCD devices (see p.40 in Ref.2). To improve process control, various strategies have been investigated to maintain surface temperature on the silicon substrates at an equilibrated value throughout a particular etching cycle. These strategies involve preheating using radiant or resistance heaters, preheating using an inert-gas plasma cycle, or constraining the process to temperatures near room temperature by use of water or refrigeration cooling. Optimum process control appears to correspond to constraining process temperatures to 25°C using a water-cooling coil on the sample-holding (ground) plate.

The plasma-etching system is similar to an RF-diode sputtering system (Fig.IV-8). The wafers to be processed are placed on top of a stainless-steel ground plate which comprises one side of a capacitor across which 13.56 MHz RF power is applied. The base plate is shown in Fig.IV-9. The gas, typically a mixture of CF_4 with a low percentage of O_2, flows from an inlet below the ground plate and sweeps radially across this plate to a vacuum port in the center. The flow is controlled by a needle valve, while a mechanical vacuum pump is at a constant throttle. The ground plate may be water-cooled and has provisions for the installation of electrical heaters. Meters for measuring forward and reflected power are provided to assist with manual

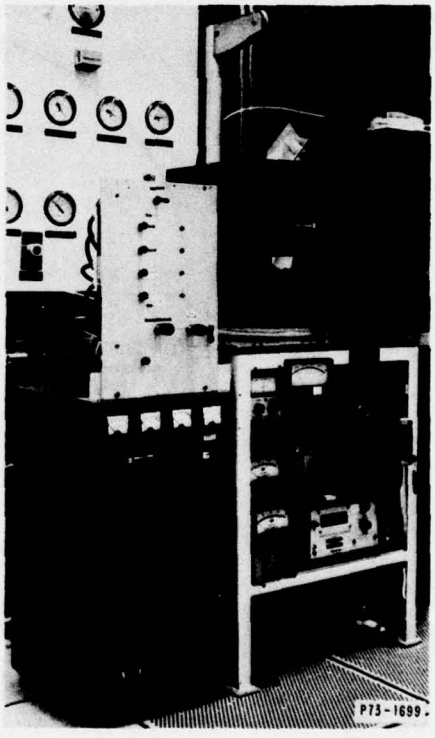


Fig.IV-8. Parallel-plate plasma reactor. At left is manifold mounted on top of a Henry RF exciter. Vacuum chamber is on right under a tuning network. Below cylindrical vacuum chamber 28 cm diam × 14 cm high are a variety of instruments including a thermocouple vacuum gauge, a capacitance manometer, mass flow meters, heater variac, gas rotometer, valves, and regulators.

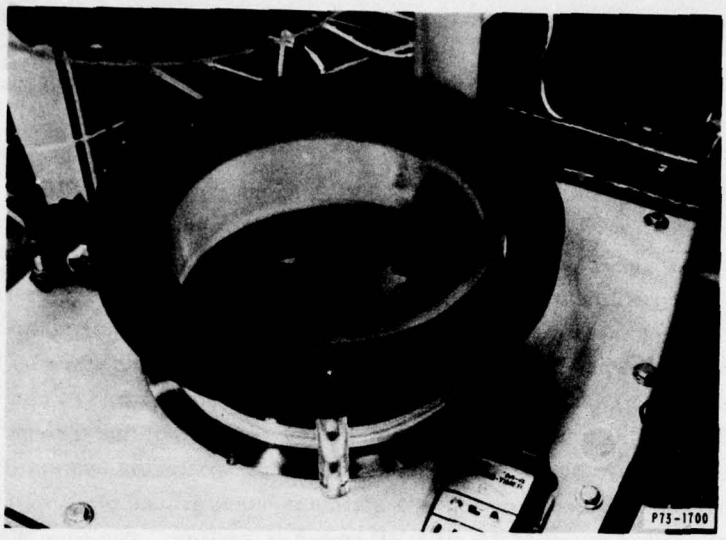


Fig. IV-9. View of open vacuum chamber with 5-cm-diam wafer placed on 23-cm-diam base plate. Gas is exhausted through port in center of stainless-steel plate. Gas inlet is located under base plate. When closed, distance between plates is 8.25 cm.

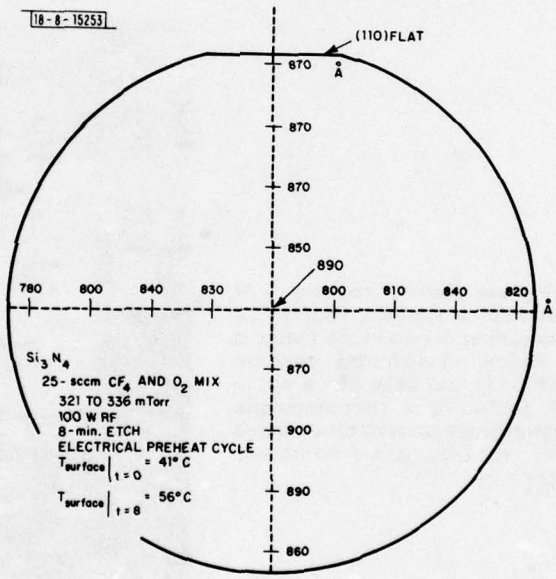


Fig. IV-10. Pictorial representation of surface profiler thickness measurements as a function of position on a typical plasma-etch test run. Thin film in this case is Si_3N_4, and negative resist was utilized earlier to form a cross-grid etch mask. For this experiment, ground plate was heated to 41°C using electrical cartridge units before 8-min. etch cycle commenced.

impedance matching, and continual adjustments are found to be necessary during the first minutes of etching. Typical operating parameters are a pressure of 180 to 280 mTorr, an RF power of 100 W forward, a gas flow of 22 sccm, and an anode-to-cathode spacing of 8.25 cm. The system volume is 8600 cm^3 and the ground plate is 23 cm in diameter.

Data were collected on oxidized, 5-cm-diam (100) silicon wafers which were patterned with negative photoresist on top of nominal 1000-Å Si_3N_4 or polysilicon films deposited using low-pressure chemical-vapor-deposition (LPCVD) reactors. The photoresist pattern consisted of lines crossing the wafers both in a direction parallel to the (110) flat and in a direction perpendicular to the flat. Measurements were performed on the two perpendicular axes that cross the center of a wafer using a step profiler. Up to 18 steps were measured on each sample, permitting determination of an average etch rate. Results of a typical measurement are given in Fig. IV-10. In addition to indicating etch rate, these measurements are useful in current work on determining etch uniformity as a function of electrical, temperature, gas-flow, vacuum, and geometrical considerations.

Plasma etching at elevated temperatures is attractive because etch rates increase as an exponential function of temperature.[10] However, this work indicates that the higher temperature process introduces process control difficulties and is a factor in the etch-uniformity difficulty. With no attempt to control wafer temperature during etching, a plasma-etch run at 100 W results in a rise in surface temperature from room temperature to an equilibrium of 40° to 45°C in a time on the order of 5 min. Because of the exponential dependence of etch rate on temperature,[10] there is no etch-rate control during this heatup period. Use of electrical resistance or radiant heating on the base plate to maintain a constant temperature is complex, as this heat input will have to be decreased as the plasma reaction proceeds.

An alternative is to try to preheat the wafers and ground-plate surface in an inert-gas plasma, typically nitrogen. The nitrogen-plasma preheating cycle, however, is not effective as a means of achieving an equilibrated etch temperature. It is also more time consuming than a cooling process because the heating rate is low and involves the use of nitrogen gas which must be pumped away before the etching gas is introduced, and thus any time gained in etch rate at higher temperatures is lost by the length of the preheating process. The problem is graphically illustrated in Fig. IV-11, which indicates the temperature of the surface of the ground plate with time during

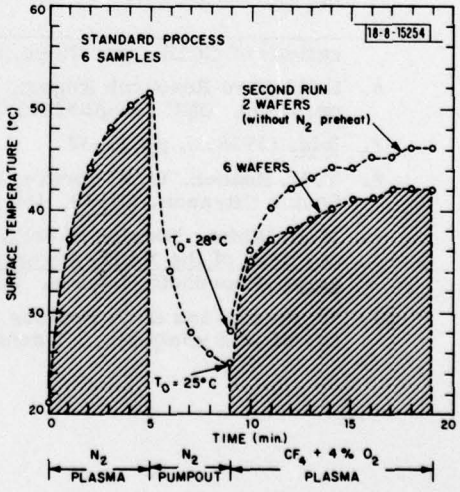


Fig. IV-11. Standard process with N_2 preheat step. N_2 plasma is on for 5 min., during which time base-plate surface reaches 51°C. It takes about 4 min. more to exhaust N_2 from system, during which time base-plate temperature returns to room-temperature range. As a result, no benefit is achieved by N_2-plasma preheat step.

a typical process initiated with a N_2-plasma heatup step. The effect of the thermal mass of the ground plate is such that the net increase in bulk temperature of the plate after 5 min. of a N_2 plasma is only 4°C, resulting in rapid cooling of the plate surface during N_2 pumpout.

By igniting the plasma with the base plate at 22°C and running water at 25 gph through the ground-plate cooling coil, we found that the plate surface temperature did not increase by more than 3°C on a typical run. The operator needed only to verify the starting temperature (20° to 25°C) and the final temperature after the plasma was turned off. The water was left running for some minutes after the etch run so that the temperature would return to its original level, thereby avoiding different initial temperatures for successive runs. The average etch rate of LPCVD Si_3N_4 at 22 cc/min. and 100 W is reduced by nearly 30 percent when the plate temperature is controlled by water cooling to 25°C, as compared with the etch rate near the equilibrated plasma-surface temperature of 40° to 45°C which is achieved after 5 min. of noncontrolled operation. We also observed that the uniformity of the etching is better at lower temperatures, though temperature is not the only contributing factor in the uniformity problem.

In conclusion, operation of a parallel-plate plasma system with controllable etch rates appears to be optimized by constraining the temperature of the base plate to near room temperature using a water-cooling coil. Run-to-run reproducibility has been achieved in the etching of various thicknesses of LPCVD Si_3N_4 and polysilicon, even when making the runs in quick succession.

D.J. Silversmith
R.W. Mountain
O. Sotomayor-Diaz

REFERENCES

1. R.A. Murphy, C.O. Bozler, C.D. Parker, H.R. Fetterman, P.E. Tannenwald, B.J. Clifton, J.P. Donnelly, and W.T. Lindley, IEEE Trans. Microwave Theory Tech. MTT-25, 494 (1977).
2. Solid State Research Report, Lincoln Laboratory, M.I.T. (1978:2), pp.36-37, DDC AD-A061241.
3. M.H. White, D.R. Lampe, F.C. Flaha, and I.A. Mack, IEEE J. Solid-State Circuits SC-9, 1 (1974).
4. R.W. Brodersen and S.P. Emmons, IEEE J. Solid-State Circuits SC-11, 147 (1976).
5. _____, Proc. Intl. Conf. on Applications of CCDs, San Diego, California, October 1975, pp.331-349.
6. Solid State Research Report, Lincoln Laboratory, M.I.T. (1977:4), pp.37-39, DDC AD-A052463/7.
7. Ibid. (1978:3), pp.31-32.
8. T.M. Reader, W.R. Shreve, and P.L. Adams, IEEE Trans. Sonics Ultrason. SU-19, 466 (1972).
9. M.H. White, "Design of Solid-State Imaging Arrays," in Proceedings of the NATO Advanced Study Institute of Solid-State Imaging (Noordhoff, Leyden, 1976), pp.494-497.
10. M. Brochu and R.G. Poulson, Extended Abstract 51, Electrochemical Society Mtg., Washington, D.C., May 1976.

V. SURFACE-WAVE TECHNOLOGY

A. PARAMETRIC INTERACTIONS IN ACOUSTOELECTRIC SURFACE ACOUSTIC WAVE (SAW) DEVICES

Several types of devices which employ nonlinear acoustoelectric interactions have been developed. The earliest device was the acoustoelectric convolver,[1] which has since reached an advanced stage of development.[2,3] More-recent devices – memory correlators,[4,5] coherent integrators,[6] and integrating correlators[7] – have incorporated charge storage in a convolver-like structure to effect a variety of signal-processing functions. In extending this work on charge-storage acoustoelectric devices, it has been recognized that the overall device performance results from a two-step parametric interaction. The first parametric interaction results in a stored charge pattern, and the second interaction utilizes this stored pattern to produce an output. The specific interactions used in each step combine to determine the overall signal-processing function performed with the device.

Examination of the various two-signal processes for charge storage and readout shows that the alternative parametric interactions can be straightforwardly interrelated. It has also been possible to extend these results to high-order interactions and to enumerate all possible signal-processing functions which can be performed with this structure. This report describes this functional summary of parametric interactions in acoustoelectric signal processing.

The structure analyzed here consists of a piezoelectric substrate and a strip of silicon held in close proximity to the piezoelectric surface. The electric fields generated by surface waves on the piezoelectric interact with carriers in the silicon. Diodes on the silicon provide a means for integrating and storing a charge pattern generated by nonlinear interactions in the silicon. The back side of the silicon is covered by a uniform conductor or plate. There exist other structures with analogous physical interactions which can also be described within the framework of this report. For simplicity, the diode structure is considered here as a prototype for these other devices.

The parametric interaction of two signals which results in a stored charge pattern is often quite complex. For the rest of this report it will be useful to consider a simple model for the charge-storage mechanism,[8] which will allow straightforward examination of the signal-processing possibilities. In this model it is assumed that the rate of change of stored charge at any point on the silicon is proportional to the local product of the interacting signal amplitudes.

Figure V-1(a-b) shows the two distinct configurations which may be used to create a charge pattern as the result of the application of two signals; both have the form of a cross-correlation of the two signals.

The two possible readout configurations, both of which are convolutions with the stored pattern, are shown in Fig. V-2(a-b). Two alternate configurations obtained by spatially reversing Figs. V-2(a) and (b) cannot be considered as distinct since they are simply convolutions with a spatially reversed charge pattern, and this spatial reversal could be achieved by interchanging the original charging signals. For emphasis, however, the convolution with the reversed pattern is indicated because of its importance as a matched-filtering or correlation process.

Possibilities resulting from the charging and readout processes are indicated in Table V-1. The two steps are a correlation of two signals followed by a convolution with a third. The

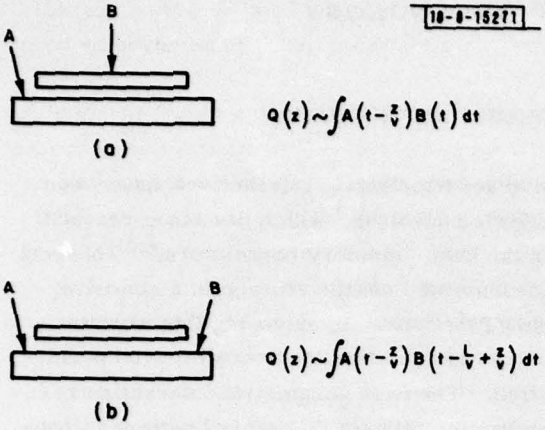


Fig. V-1(a-b). Charge storage.

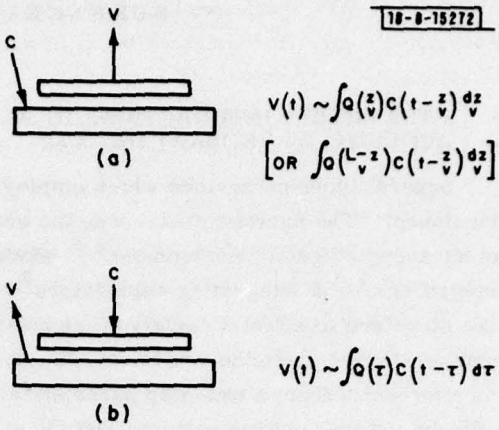


Fig. V-2(a-b). Charge readout.

TABLE V-1

SIGNAL-PROCESSING FUNCTIONS OBTAINABLE WITH CORRELATION OF TWO SIGNALS FOLLOWED BY CONVOLUTION WITH A THIRD SIGNAL

A	B	C	Result
H(t)	Impulse	Input	Programmable filter (memory convolver)
Impulse	H(t)	Input	Programmable matched filter (memory correlator)
Pulse train	Impulse train	Impulse	Coherent pulse overlay (coherent integrator)
Impulse train	Pulse train	Pulse	Burst-waveform processor
Input	Reference	Impulse	Correlation receiver with window (integrating correlator)
Reference	Input + H(t)	H(t)	Integrating correlator with improved readout

situation of making the readout convolution look like a correlation can be achieved by several possible changes in geometry, but it is assumed for this discussion that it is achieved by interchanging the charging signals.

By making one input approximately an impulse, it is possible to store a signal H(t) applied to the other input. The device then can appear to be a filter, with H(t) as its impulse response for a subsequent signal C(t). If C(t) also approximates an impulse, then the device acts as an analog memory for the waveform H(t). By interchanging the original signals, it is possible to make a matched filter for H(t) or a memory which can read out the time reverse of H(t). In the matched-filter mode, the device is referred to as a memory correlator.[4,5]

If a pulse train is one input and a synchronous impulse train is the other, then the resulting charge pattern will have all the pulses overlayed in the same location within the device. A device called a coherent integrator[6] has been developed for implementing this process for improving the signal-to-noise ratio of a repeated signal. An impulse is used to read out the resulting pattern. If the pattern is not a simple pulse but has significant structure, then correlation readout can be used to compress the waveform on readout. The resulting use of a coherent integrator is ideally suited to processing radar burst waveforms.

If the inputs are a long-duration signal and a suitable reference, then the resulting charge pattern is a finite portion of the cross-correlation function, and this can be read out to look for a correlation spike which would appear if the timing of the signal and reference was correct to within the propagation time through the structure. A device called an integrating correlator[9] has been developed to act as a correlation receiver which searches a large timing window on each integration interval, thus significantly reducing search time for acquisition of a spread-spectrum signal.

All the examples given so far have used an impulse for at least one of the three applied signals. A more-general capability is available if an impulse is not used. The last example of Table V-1 shows this concept applied to the integrating correlator. Ralston[9] has shown that the integrating correlator can be improved by spatially spreading the stored correlation function, by passing the input through a dispersing filter, and then recompressing on readout. But this corresponds to replacing the impulse readout with a cross-correlation readout using the impulse response of the dispersing filter.

It is instructive to consider the ω-k diagram representation of parametric interactions. Proper interpretation of the ω-k plane as the domain of Fourier-transform space for the various signals will lead to correct conclusions concerning these interactions.

Figure V-3(a) shows the ω-k plane, with heavy lines indicating the allowed dispersion lines for signals which occur in the acoustoelectric charge-storage devices. Signals on the semiconductor strip must be spatially uniform and therefore must fall on the ω-axis. A stored charge pattern is at $\omega = 0$ and thus appears on the k-axis. The line $\omega = kv$ (where v is the SAW velocity) represents forward-traveling acoustic-wave signals, while $\omega = -kv$ represents waves in the reverse direction. The filled and empty dots represent the "normal" and "conjugate" components of a real wave traveling in the forward direction. The ω-k diagram can be used as a map of the two-dimensional Fourier-transform space of a general space-time signal. A line segment on the appropriate dispersion line is used to represent a wideband signal.

These ideas are now applied to the interaction of two acoustic-wave signals, as shown in Fig. V-3(b). A parametric interaction is represented as vector addition in the ω-k plane: the vector sum indicates the ω and k of the signal generated as a result of the interaction. The

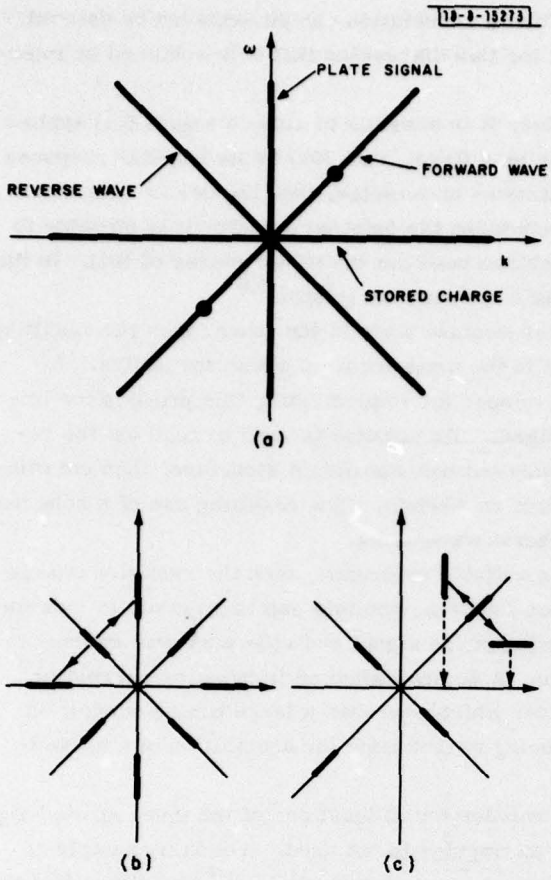


Fig. V-3. ω-k diagrams: (a) allowed dispersion lines; (b) convolution and correlation; and (c) three-signal interactions.

arrows in Fig. V-3(b) show the two possible center-frequency interactions: a signal is produced which has twice the center frequency and zero k. This is recognized as the convolver interaction. Another signal has twice the spatial frequency but does not oscillate in time. This is the signal which stores charge in a correlation operation. The vector sum is satisfied over a finite bandwidth, thus indicating that these operations are really convolution and correlation. Note that the convolution interaction used the normal field of both waves, while the correlation interaction used the normal field of one and the conjugate of the other. This is exactly in keeping with the Fourier-transform interpretation of the ω-k diagram: convolution and correlation are point-by-point multiplications in the frequency domain, but correlation uses the conjugate of one of the transforms.

In a more-general case, suppose two acoustic waves interact as in Fig. V-3(b), but we let the center frequencies be different. The resulting center-frequency ω-k diagram is indicated by the arrows of Fig. V-3(c), and the two possible vector sums fall on neither the ω- nor k-axis. If an interaction of three signals is considered rather than two, then a CW pump signal could be applied to the silicon to translate either of the two-signal products down to the k-axis at center frequency, as indicated by the dashed arrows. However, only one of the two parametric interactions yields products along the k-axis for a finite bandwidth. This interaction is just a

"k-shifted" version of the degenerate case when the acoustic-wave signals have the same center frequency; it still stores the correlation of the two signals as a charge pattern.

A three-signal interaction has been introduced in the ω-k discussion to show compatibility with the Fourier-transform interpretation of ω-k diagrams. The ω-k diagram of Fig. V-3(a) shows four possible dispersion lines. In an interaction of order n, an output signal is produced by n input signals, and n + 1 dispersion lines must be used. The number of distinct interactions which use only one dispersion line at a time is quite restricted. There are no fourth- or higher-order interactions which are distinct from second- or third-order possibilities in structures of this type for lack of more dispersion lines.

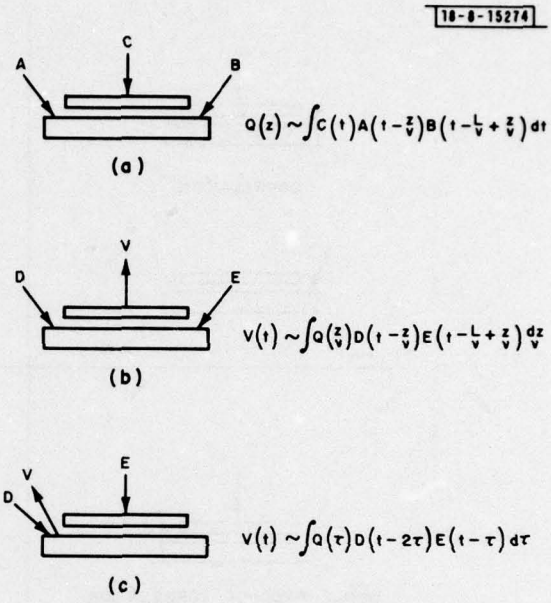


Fig. V-4(a-c). Three-signal interactions.

Figure V-4(a-c) summarizes the distinct three-signal interactions. There is only one three-signal charge-storage interaction, shown in Fig. V-4(a). Since all three signals appear forward in time inside the integral, this is analogous to correlation and one might call this "triple-product correlation." Figure V-4(b) shows one of the possible readout interactions. It has the form of a convolution of the two acoustic signals, but the stored charge pattern acts as a stationary weighting function. Others have referred to this operation as "triple-product convolution." Figure V-4(c) shows the other distinct readout which has the form of a correlation of the time signals with the stored charge, again as a weighting function. By analogy with Fig. V-4(b), this process is called "triple-product correlation."

These three-signal interactions are interesting for two reasons. First, if the third signal is a CW pump, then the interaction can be a convolution or correlation of two signals as in a two-signal interaction, but with a shift of the k of the stored pattern or the ω of the output signal. These degrees of freedom might be of use in the design of practical devices – for example, in the suppression of spurious signals. Second, if used in their full generality, these three-signal interactions offer new signal-processing capabilities such as beam forming with arrays of arbitrary geometry.[10]

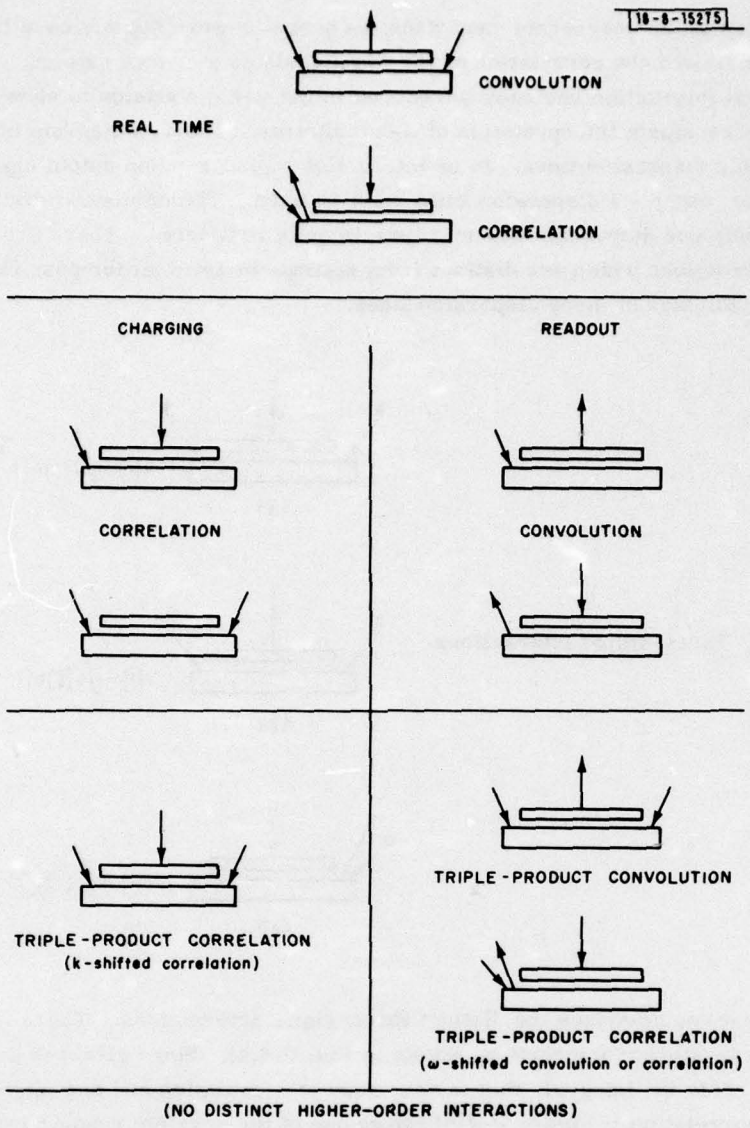


Fig. V-5. Acoustoelectric signal-processing operations.

Figure V-5 shows a summary of the real-time interactions, two-signal storage and readout, and three-signal storage and readout. The familiar acoustoelectric convolver and a correlation device[11] constitute the possible real-time interactions. Two-signal charge storage is always a correlation, and two-signal readout is always a convolution process, although the ability to access the spatially reversed charge pattern can make this readout appear as a correlation. Three-signal charge storage has the form of a triple-product correlation or a k-shifted correlation of two signals. Three-signal readout is either triple-product convolution or triple-product correlation, but can also be used to perform ω-shifted convolution or correlation of two signals.

J. H. Cafarella

B. RESONANT INTERACTIONS OF SURFACE AND BULK ACOUSTIC WAVES IN GRATINGS

In transmitting a surface wave through normal-incidence gratings with a period approximately equal to the acoustic wavelength, one observes a series of sharp stop bands, as shown on Fig. V-6 for gratings of two different depths, 1920 and 3640 Å. For a 4800-Å-deep grating, the stop bands are deeper and sharper. Expanded plots of the transmission at one such stop band are shown in Fig. V-7.

The stop band occurs when the surface wave couples to a plate mode of the substrate. The modes to which the surface wave couples consist essentially of bulk waves which are multiply reflected at near-vertical incidence between the top and bottom surfaces. The condition for coupling can be expressed as

$$K_p = K_g - K_s \qquad \text{(V-1)}$$

where K_p is the projection along the surface of the wave vector of the plate mode, $K_g = 2\pi/d$

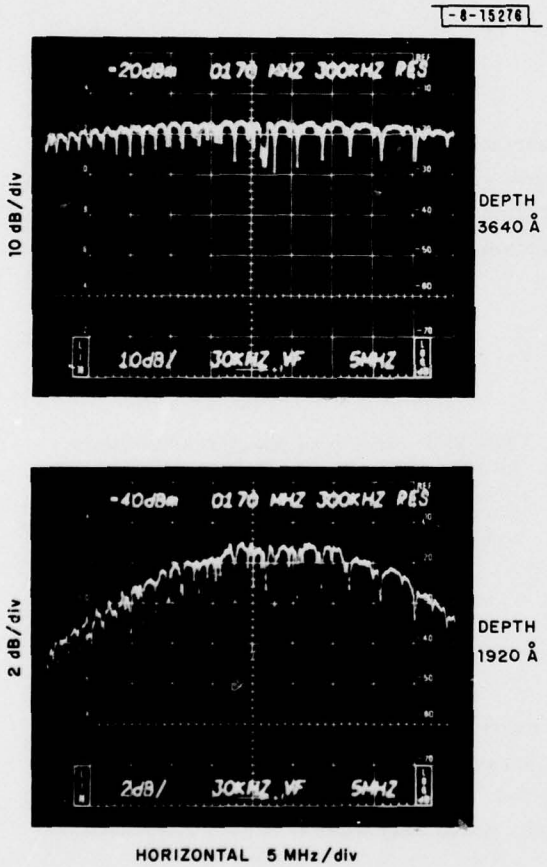


Fig. V-6. Transmission through a 200-groove grating at normal incidence. Center frequency is 170 MHz. Period of grooves is 20.32 μm.

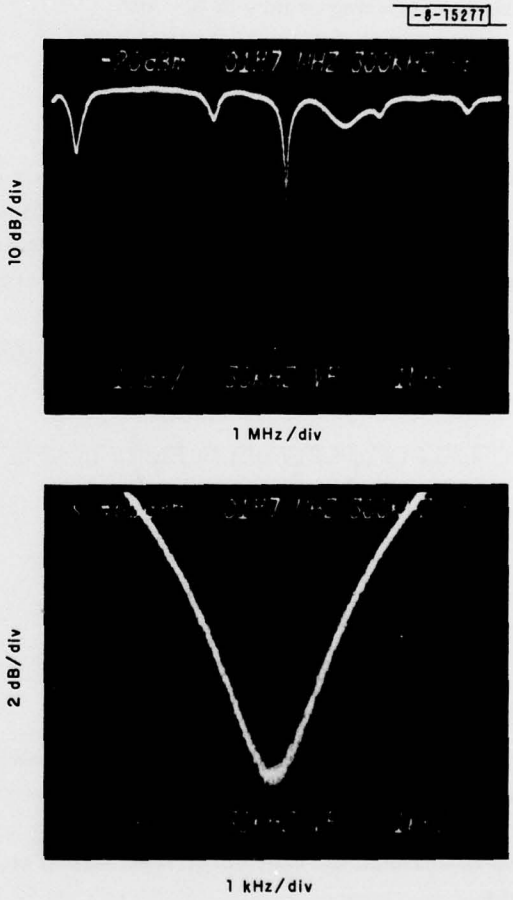


Fig. V-7. Same as Fig. V-6 except expanded and for a 4800-Å-deep grating. Center frequency is 194.2 MHz.

where d is the grating period, and K_s is the magnitude of the wave vector of the surface wave in the grating. This is similar to the problem of coupling of interdigital transducers to plate modes.[12]

A simplified model of the coupling can be derived by first examining the angle of propagation of a scattered bulk wave, and then specifying the conditions for efficient coupling into plate modes characterized by a bulk wave propagating at this angle. The exact solution for a plate mode involves both shear and longitudinal bulk waves. In order to derive a simplified model of the resonance phenomenon, the approximation is made that only a single bulk wave is scattered and that there is no longitudinal-to-shear-wave coupling upon reflection. With these approximations Eq. (V-1) can be rewritten as

$$|K_B| \cos\Theta = K_g - K_s \tag{V-2}$$

where K_B is the wave vector of the only bulk wave in the model, and Θ is the angle relative to the surface at which the bulk wave is scattered and reflected (see Fig. V-8). When $K_g = K_s$ or, equivalently, when the wavelength of the surface wave is approximately equal to the grating period, scattering occurs at $\Theta = 90°$.

Equation (V-2) may be rewritten as

$$\cos\Theta = \frac{v_B}{v_s}\left(1 - \frac{f_o}{f}\right) \tag{V-3}$$

where v_B and v_s are the velocities of the bulk and surface waves, and $f_o = v_s/d$. Note that f_o is twice the frequency of the stop band in which coupling of a surface wave into a reflected surface wave occurs. For $f > f_o$ the bulk waves are scattered in the reverse direction ($\Theta < 90°$), while for $f < f_o$ the scattering is in the forward direction.

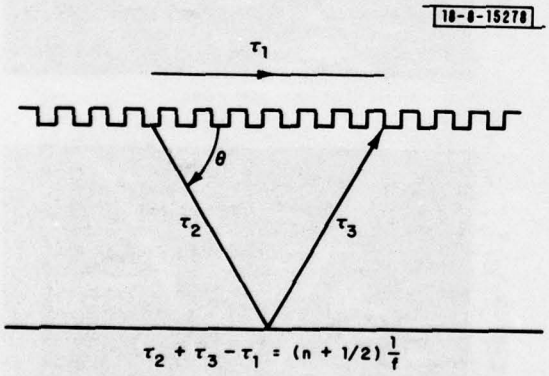


Fig. V-8. Model of sharp transmission stop bands. τ_2 and τ_3 are bulk-wave transit times, and τ_1 is surface-wave transit time from conversion points. n is an integer.

A stop band is produced when the bulk wave bounces off the bottom, travels back up to the grating, and reconverts to a surface wave which is out of phase with the original surface wave traveling in the grating. This is illustrated in Fig. V-8. When many reflections occur, a sharp stop band results. Therefore, these sharp stop bands occur only when $\Theta \sim 90°$, i.e., when $f \sim f_o$.

Several experimental observations indicate the existence and nature of the surface-wave-to-plate-mode coupling in normal-incidence gratings. When a surface wave is launched on the top (grating) surface of a substrate, the spatial period of a plate mode may be measured by

surface-probing the field pattern on the bottom surface. This was done for a series of frequencies corresponding to the centers of several stop bands. In each case, the measured periodicity was accurately predicted by Eq. (V-1).

In a second series of experiments, a CW tone was applied to the input transducer and the result of multiple bounces of the scattered waves was observed vs time in the output transducer, as shown in Fig. V-9. The top left photo shows the received RF signal. The next three photos show the phase-detected response for frequencies at the middle of a stop band, between two stop bands, and at the middle of the next stop band, respectively. Note that the multiple echoes are out of phase with the direct transmission at the centers of the stop bands, whereas the echoes alternate in phase at a frequency between stop bands.

As a third check on the existence of plate-mode coupling, the back of a substrate was scored with a diamond saw; the multiple stop bands disappeared, as anticipated.

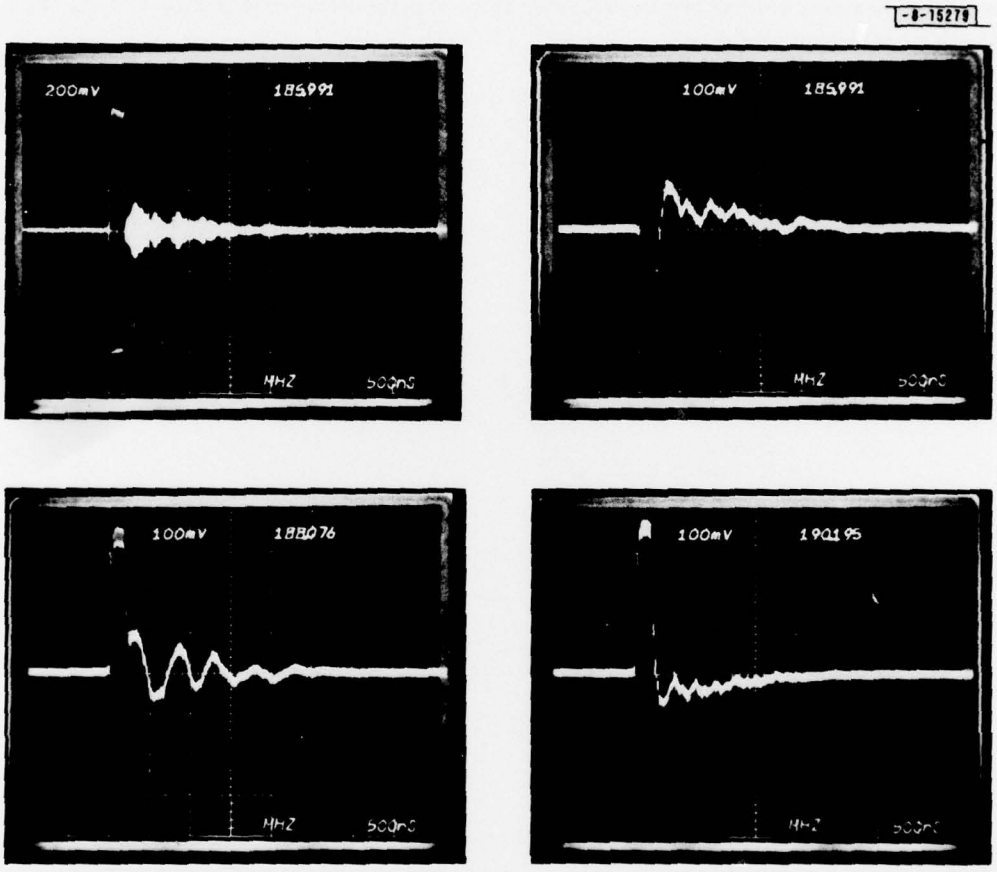


Fig. V-9. Transmission of a 200-nsec tone burst through grating. Upper left is direct RF output. At top right, it is shown mixed with CW to yield phase information at a 185.99-MHz stop-band frequency. Left bottom trace is between two stop-band frequencies at 188.08 MHz showing that alternate bounces of bulk wave yield out-of-phase signals. Bottom right trace is at next stop-band frequency (190.02 MHz).

Using the condition for resonance shown in Fig. V-8, one can make an approximate calculation of the stop-band frequencies. The timing condition of Fig. V-8 combined with Eq. (V-3) yields the relation

$$\frac{1-\left(\frac{v_B}{v_s}\right)^2\left(1-\frac{f_o}{f}\right)}{\sqrt{1-\left(\frac{v_B}{v_s}\right)^2\left(1-\frac{f_o}{f}\right)^2}} = \frac{(n+\frac{1}{2})\frac{f_o}{f}}{2bf_o/v_B} \qquad \text{(V-4)}$$

where b is the thickness of the substrate. The quantity $2bf_o/v_B$ is the number of bulk-wave periods in the round trip from the top to the bottom of the crystal at normal incidence at frequency f_o. Equation (V-4) may be solved for the stop-band frequencies f corresponding to successive values of n. The parameters inserted into Eq. (V-4) to calculate the values of f for the experiments on Y-Z $LiNbO_3$ were v_s = 3485 m/sec, b = 1.27 mm, and f_o = 171.51 MHz. In addition, the dominant bulk wave was assumed to be a shear wave propagating at a constant velocity of 4444 m/sec (Ref. 13).

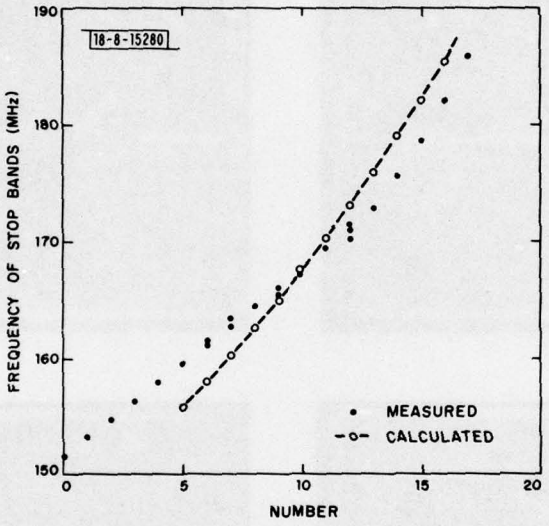


Fig. V-10. Calculated and measured stop-band frequencies plotted in order vs "number." Measured stop bands are those obtained from a display such as shown in Fig. V-6. Stop bands plotted are those which are most prominent and appear to belong to a series. When a stop band appears split, several frequencies are plotted at one number.

The theoretical stop-band frequencies and the frequencies of the most-prominent experimental stop bands are plotted in Fig. V-10. The correspondence is seen to be good for $f > f_o$. (The curves can be displaced laterally since the "number" assignment is arbitrary.) The disagreement for $f < f_o$ may be due to the approximations used. The deviation of the simple model is in the right direction, since the inclusion of longitudinal waves in the exact plate-mode calculation would yield higher coupled-wave velocities and a lower slope for the theoretical curve. However, the approximate quantitative agreement indicates that the general interpretation of the phenomenon is correct.

J. Melngailis

REFERENCES

1. J. M. Smith, E. Stern, A. Bers, and J. H. Cafarella, "Surface Acoustoelectric Convolvers," in 1973 Ultrasonics Symposium Proceedings (IEEE, New York, 1973), pp. 142-144, DDC AD-A000497/8.
2. J. H. Cafarella, J. A. Alusow, W. M. Brown, and E. Stern, "Programmable Matched Filtering with Acoustoelectric Convolvers in Spread-Spectrum Systems," in 1975 Ultrasonics Symposium Proceedings (IEEE, New York, 1975), pp. 205-208, DDC AD-A031716/4.
3. S. A. Reible, J. H. Cafarella, R. W. Ralston, and E. Stern, "Convolvers for DPSK Demodulation of Spread Spectrum Signals," in 1976 Ultrasonics Symposium Proceedings (IEEE, New York, 1976), pp. 451-455, DDC AD-A040519/1.
4. A. Bers and J. H. Cafarella, "Surface Wave Correlator-Convolver with Memory," in 1974 Ultrasonics Symposium Proceedings (IEEE, New York, 1974), pp. 778-787, DDC AD-A011326/6.
5. K. A. Ingebrigtsen, R. A. Cohen, and R. W. Mountain, Appl. Phys. Lett. 26, 596 (1975), DDC AD-A016703/1.
6. K. A. Ingebrigtsen and E. Stern, Appl. Phys. Lett. 27, 170 (1975), DDC AD-A016688/4.
7. R. W. Ralston, D. H. Hurlburt, F. J. Leonberger, J. H. Cafarella, and E. Stern, "Gap-Coupled Schottky-Diode/$LiNbO_3$ Acoustoelectric Integrating Correlator," paper presented at IEEE Device Research Conf., Cornell University, 27-29 June 1977, abstract published in IEEE Trans. Electron Devices ED-24, 1190 (1977).
8. J. H. Cafarella, "Surface State Acoustoelectric Memory-Correlator," Sc. D. Thesis, Department of Electrical Engineering, Massachusetts Institute of Technology, Cambridge, Mass., February 1975.
9. R. W. Ralston, D. H. Hurlburt, F. J. Leonberger, J. H. Cafarella, and E. Stern, "A New Signal-Processing Device, The Integrating Correlator," in 1977 Ultrasonics Symposium Proceedings (IEEE, New York, 1977), pp. 623-628, DDC AD-A057512.
10. J. M. Speiser and N. J. Berg, "Signal Processing Architectures Using Convolutional Technology," to be published in Real-Time Signal Processing, Society of Photo-Optical Instrumentation Engineers Symposium Proceedings, Vol. 154.
11. I. Drukier, W. C. Wang, and P. Das, Appl. Phys. Lett. 23, 4 (1973).
12. R. S. Wagers, IEEE Trans. Sonics Ultrason. SU-23, 113 (1976).
13. R. F. Milsom, N. H. C. Reilly, and M. Redwood, IEEE Trans. Sonics Ultrason. SU-24, 158 (1977).

UNCLASSIFIED

SECURITY CLASSIFICATION OF THIS PAGE *(When Data Entered)*

REPORT DOCUMENTATION PAGE

READ INSTRUCTIONS BEFORE COMPLETING FORM

1. REPORT NUMBER: ESD-TR-78-287	2. GOVT ACCESSION NO.
3. RECIPIENT'S CATALOG NUMBER	
4. TITLE *(and Subtitle)*: Solid State Research, 1978:4.	5. TYPE OF REPORT & PERIOD COVERED: Quarterly Technical Summary rept. 1 August – 31 October 1978
	6. PERFORMING ORG. REPORT NUMBER: 1978:4
7. AUTHOR(s): Alan L. McWhorter	8. CONTRACT OR GRANT NUMBER(s): F19628-78-C-0002
9. PERFORMING ORGANIZATION NAME AND ADDRESS: Lincoln Laboratory, M.I.T. P.O. Box 73 Lexington, MA 02173	10. PROGRAM ELEMENT, PROJECT, TASK AREA & WORK UNIT NUMBERS: Program Element No. 65705F Project No. 649L
11. CONTROLLING OFFICE NAME AND ADDRESS: Air Force Systems Command, USAF Andrews AFB Washington, DC 20331	12. REPORT DATE: 15 November 1978
	13. NUMBER OF PAGES: 76
14. MONITORING AGENCY NAME & ADDRESS *(if different from Controlling Office)*: Electronic Systems Division Hanscom AFB Bedford, MA 01731	15. SECURITY CLASS. *(of this report)*: Unclassified
	15a. DECLASSIFICATION DOWNGRADING SCHEDULE

16. DISTRIBUTION STATEMENT *(of this Report)*

Approved for public release; distribution unlimited.

17. DISTRIBUTION STATEMENT *(of the abstract entered in Block 20, if different from Report)*

18. SUPPLEMENTARY NOTES

None

19. KEY WORDS *(Continue on reverse side if necessary and identify by block number)*

solid state devices
quantum electronics
materials research
microelectronics
surface-wave technology
photodiode devices
lasers
laser spectroscopy
imaging arrays
infrared imaging
surface-wave transducers
charge-coupled devices
acoustoelectric devices

20. ABSTRACT *(Continue on reverse side if necessary and identify by block number)*

This report covers in detail the solid state research work of the Solid State Division at Lincoln Laboratory for the period 1 August through 31 October 1978. The topics covered are Solid State Device Research, Quantum Electronics, Materials Research, Microelectronics, and Surface-Wave Technology. Funding is primarily provided by the Air Force, with additional support provided by the Army, ARPA, NSF, and DOE.

DD FORM 1 JAN 73 1473 EDITION OF 1 NOV 65 IS OBSOLETE

207 650

UNCLASSIFIED

SECURITY CLASSIFICATION OF THIS PAGE *(When Data Entered)*

☆U.S. GOVERNMENT PRINTING OFFICE: 1979 – A-1173/30